PROBING THE CAUSES AND EFFECTS OF PARASITIC REACTIONS IN LITHIUM-ION CELLS

by

Leah Ellis

Submitted in partial fulfilment of the requirements
for the degree of Doctor of Philosophy

at

Dalhousie University
Halifax, Nova Scotia
April, 2018

TABLE OF CONTENTS

LIST OF TABLES

LIST OF FIGURES

ABSTRACT

Parasitic reactions in lithium-ion cells consume solvent, salt and active lithium ions, resulting in a loss of capacity and eventual cell failure. The projects described in this thesis have the common goal of exposing the chemical mechanisms of these parasitic reactions and probing their effects on cell performance. Three types of projects are described in this thesis. The first part of this thesis is focused on exposing and probing the effects of parasitic reactions that cause the evolution and consumption of gases in lithium-ion cells. The second project is focused on probing how the conditions of the first cycle of a lithium-ion cell impact the amount of parasitic reactions in subsequent cycles. The third project describes the development and use of a new analytical tool for quantifying the solvent/salt ratio in the electrolyte of aged cells. This work improves the understanding of certain parasitic reactions that may contribute to capacity fade and eventual failure of lithium-ion cells.

LIST OF ABBREVIATIONS AND SYMBOLS USED

ATR: attenuated total reflectance

B: buoyant force

BE: binding energy

C/#: the "C-rate", or current at which a cell is cycled, were C is the cell capacity in mAh, and # is the number of hours desired to charge or discharge the cell.

$\mathbf{C_{dl}}$: double layer capacitance

CE: coulombic efficiency

CIE: coulombic inefficiency

CPS: counts per second

DMC: dimethyl carbonate

DTD: ethylene sulfate

EC: ethylene carbonate

EMC: ethyl methyl carbonate

Fade: discharge capacity lost in one cycle

FEC: fluoroethylene carbonate

FTIR: Fourier transform infrared (spectroscopy)

FWHM: full width at half maximum

GC: gas chromatography

GED: gas extraction device

HPLC: high performance liquid chromatography

hv: energy of a photon

ICP-OES: inductively coupled plasma optical emission spectrometry

IMFP: inelastic mean free path

k: SEI passivation growth constant

mg: force of gravity

MMDS: 5,2,4-dioxadithiane-2,2,4,4-tetraoxide

MS: mass spectrometry

m/z: mass-to-charge ratio

NMC: $Li[Ni_xMn_yCo_z]O_2$ (where x+y+z=1), a positive electrode material. The ratio of Ni:Mn:Co is sometimes appended as a suffix; for example, $LiNi_{0.4}Mn_{0.4}Co_{0.2}O_2$ is referred to in short as NMC442.

NMR: nuclear magnetic resonance (spectroscopy)

OCV: open circuit voltage

PES: prop-1-ene-1,3-sultone

PES###: a ternary blend of PES, DTD and TTSPi, where # are the weight percents of the three additives.

PVDF: polyvinylidene fluoride

Q: cell capacity, sometimes with subscript c or d to indicate charge or discharge capacity

R: some unknown species

$\mathbf{R_s}$: solution resistance

RSF: relative sensitivity factors

SEI: solid electrolyte interphase

SlipC: charge endpoint capacity slippage

SOC: state of charge

T: force of tension

t: time

TCD: thermal conductivity detector

TTSPi: Tristrimethylsilyl phosphite

UHPC: ultra high precision coulometry

V: volume

VC: vinylene carbonate

VC###: a ternary blend of VC, MMDS and TTSPi, where # are the weight percents of the three additives.

x: degree of SEI passivation

Φsp : work function of an XPS spectrometer

CHAPTER 1 INTRODUCTION

Lithium-ion cells are the energy storage devices of choice for portable electronic devices due to their superior volumetric energy density and cycle life. Lithium-ion cells are also drawing the attention of the sustainable energy sector, as efforts continue to replace fossil fuels with electricity. Many green technologies, such as solar panels, wind turbines, and electric vehicles either generate or use electricity. These technologies must be paired with energy storage devices, such as lithium-ion batteries, capable of storing electrical energy for later use.

To be practically and economically competitive with fossil fuel-powered counterparts, green technologies require energy storage systems capable of operating for many years. The cycle life and energy density of most lithium-ion cells are limited by the stability of their electrolyte solutions.[1] Solvent and salt molecules in the electrolyte react at charged electrode surfaces.[2] Reaction rates increase with temperature and vary with electrode potential. Not only do the reactions consume active lithium and electrolyte; they can also result in the formation of films on both electrodes.[3] These films are often referred to as Solid-Electrolyte Interphases (SEIs). An SEI can be beneficial to cell performance if it passivates against further unwanted reactions, and detrimental if it impedes the passage of active lithium ions.[4] In these ways, parasitic reactions involving the electrolyte cause capacity loss and limit the lifetime of lithium-ion cells.

This thesis is devoted to exposing the parasitic reactions in lithium-ion cells and probing their effects on cell performance. This introduction will begin with a description of lithium-ion cell parts and the types of parasitic reactions. The research projects described in this work will be introduced in more detail.

1.1 Lithium-Ion Cell Components

A lithium-ion cell, like any other electrochemical cell, contains two electrodes separated by an ion-conducting electrolyte. One electrode is called the "positive" electrode and the other is called the "negative" electrode, since one electrode has a higher voltage vs. lithium than the other. Electrons flow spontaneously when the charged electrodes are connected by an electron-conducting path, a process called "discharge". Lithium is oxidized in the negative electrode, and the resulting electron travels through the electron-conducting path (where it is used to do work) towards the positive electrode, where it reduces a transition metal ion in the positive electrode. Simultaneously, a lithium ion leaves the negative electrode, diffuses through the electrolyte, and enters the positive electrode, where it is needed to maintain charge-balance after the reduction of a transition metal ion. Equation (1) shows the oxidation of lithium intercalated in graphite (C_6), which occurs at the negative electrode during discharge. Equation (2) shows the reduction of a lithium transition metal oxide ($LiMO_2$), which occurs at the positive electrode during discharge.

$$LiC_6 \rightarrow Li_{1-y}C_6 + yLi^+ + ye^- \qquad (1)$$

$$xLi^+ + xe^- + Li_{1-x}MO_2 \rightarrow LiMO_2 \qquad (2)$$

When an external bias is applied to the cell, the reverse reactions occur. Lithium ions and electrons are removed from the positive electrode upon the oxidation of a transition metal ion. The electron moves through the external circuit towards the negative electrode and the lithium ion moves through the electrolyte towards the negative electrode, where they recombine in a reduction reaction. A cartoon of a lithium-ion cell, illustrating the flow of lithium ions and electrons during charge and discharge, is shown in Figure 1.1.1. In the following subsections, the components of a lithium-ion cell will be described in more detail, with an emphasis on their reactions that contribute to cell aging.

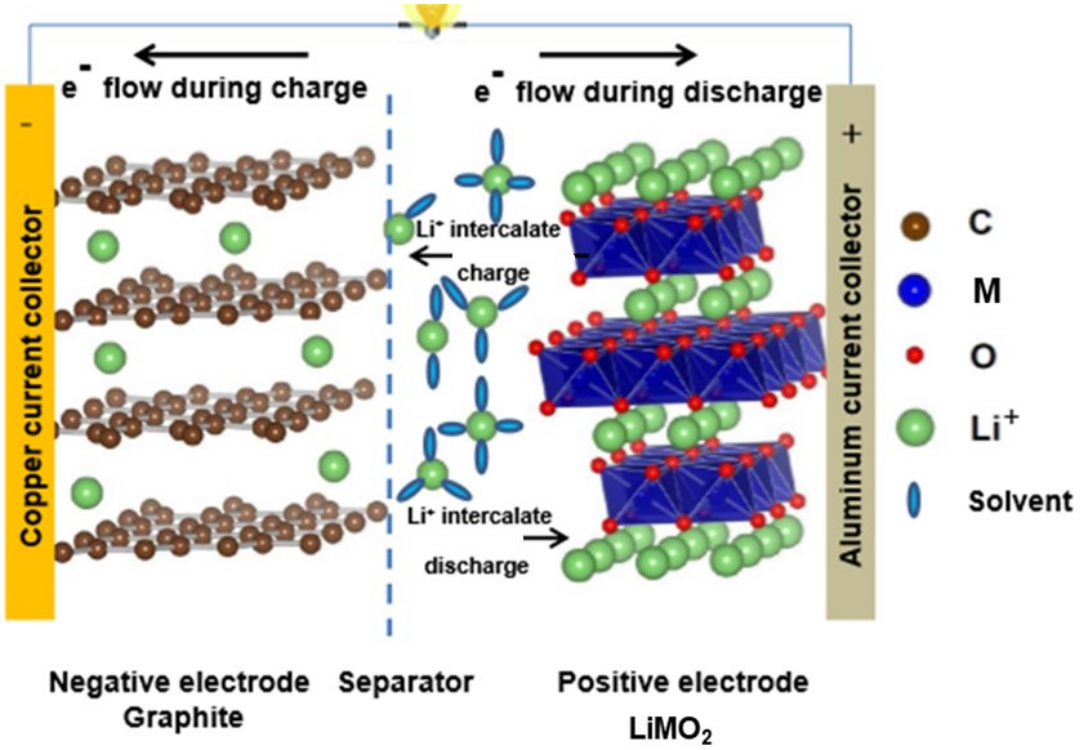

Figure 1.1.1: anillustration of a lithium-ion cell. "M" in $LiMO_2$ stands for a combination of Co, Ni, and/or Mn. This figure is adapted with permission from D.J. Xiong, Surprising Chemistry in Li-ion Cells, PhD thesis, Dalhousie University, Halifax, NS, Copyright (2017).

1.1.1 The Negative Electrode

The negative electrode in lithium-ion cells is typically made of graphite. Lithium reacts with graphite by a process called intercalation, whereby lithium atoms insert between graphite sheets, inducing minimal structural change to the graphite upon insertion, removal and reinsertion (12% volume expansion).[5] Recently, electrode materials made from lithium-metal alloys have drawn considerable attention due to their high energy densities.[6] Presently, no cell manufacturers can boast the successful adaptation of graphite-free alloy negative electrodes. For this reason, only graphite negative electrodes will be discussed in this thesis.

An important part of the negative electrode that is not shown in Figure 1.1.1 is the negative electrode SEI. This is a film formed by the reaction of lithium with electrolyte components. The first electrolyte components to react are typically electrolyte additives, which are added to the electrolyte to form passivating films. The best-known electrolyte additives (described in greater detail in Section 1.1.3) are thought to form passivating SEI films that hinder further reaction of the electrolyte. Thus, the negative electrode SEI is crucial for lithium-ion cell operation.

The graphite electrode is typically made by mixing graphite powder in an aqueous slurry with carbon black and a binder. The binder is typically a combination of sodium carboxymethyl cellulose and styrene-butadiene rubber. The slurry is cast onto a copper

foil current collector, dried and compressed before being assembled into a lithium-ion cell.

1.1.2 The Positive Electrode

Positive electrodes in lithium-ion cells are typically layered lithium transition metal oxides with crystalline structures capable of supporting lithium intercalation. The most common positive electrode material is lithium cobalt oxide ($LiCoO_2$, called LCO). LCO has high capacity and high average voltage relative to some positive electrode materials but is costly[7] Substitution of the cobalt in LCO with nickel and manganese results in an increasingly popular positive electrode material, called NMC.[8,9] The ratio of nickel, cobalt and manganese can be varied to optimize cost, capacity, thermal stability and cycle life.[10] The ratio of Ni, Mn and Co in a material is commonly appended as a suffix to NMC. For example, $LiNi_{0.4}Mn_{0.4}Co_{0.2}O_2$ is referred to in short as NMC442. Only NMC positive electrode materials will be discussed in this work, as they are of greater interest for green energy applications.

The positive electrode also has an SEI, formed on the first cycle from the oxidation of electrolyte, or other species in solution. It is much thinner than the negative electrode SEI, although it has a somewhat similar composition.[11–15] It is made from LiF, fluorophosphates, organic species, and decomposed additives (if used). Changes to the surface and bulk material of a commercial positive electrode are small when cycled in cells up to 4.2 V, and are minor contributors to capacity loss in cells.[16–19] However, when

cells are cycled above 4.2 V, cell failure is often attributable to impedance growth at the positive electrode.[20–23] The cause of this impedance growth is not well understood. This effect may have something to do with the collapse of lithium-conducting pathways in the crystal lattice as a result of oxygen loss from the surface of charged positive electrodes.[24,25] However, this explanation is not sufficient, since in many cases dramatic impedance changes are reversible. [26,27]

The positive electrode is typically made by mixing lithium transition metal oxides in a slurry with a conductive diluent and a binder. The solvent for the slurry is typically *N*-methylpyrrolidone. The conductive diluent and binder are typically carbon black and polyvinylidene difluoride (PVDF). The slurry is cast onto an aluminum foil current collector, dried and compressed before being assembled into a lithium-ion cell.

1.1.3 The Electrolyte

The electrolyte in a typical lithium-ion cell is ~1M $LiPF_6$ dissolved in a blend of organic carbonate solvents, with some electrolyte additive(s). $LiPF_6$, in a concentration near 1M, is widely acknowledged to deliver the best performance.[2,28] Common solvents include ethylene carbonate (EC), dimethyl carbonate (DMC), and ethyl methyl carbonate (EMC), shown in Figure 1.1.2. Commercial electrolytes normally contain some amount of EC, which is sacrificially reduced to form a passivating SEI on the negative electrode.[5,29] Electrolyte additives, used to form passivating SEI films or improve other aspects of performance, are typically added in amounts less than 5 wt. %. The types and amounts of

electrolyte additives used by manufacturers are closely guarded trade secrets. Some well-known electrolyte additives used in this thesis are shown in Figure 1.1.2.

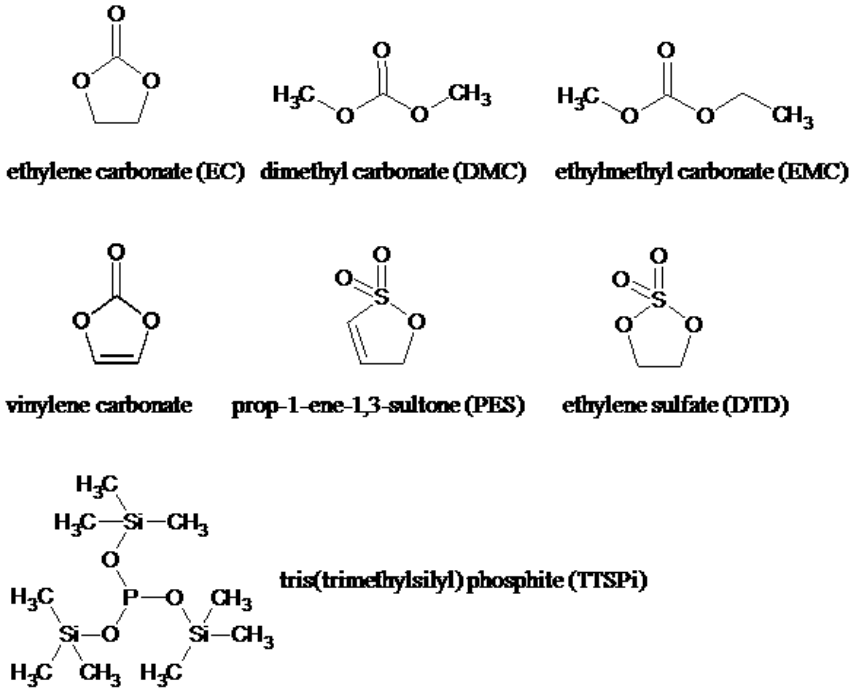

Figure 1.1.2: structures and abbreviated names of commonly used carbonate solvents and electrolyte additives.

The electrolyte is susceptible to reaction at the surface of charged electrodes, causing gas evolution and the formation of SEI components. Heating the electrolyte can also cause electrolyte decomposition. Reactions between the salt and the solvent occur with increasing temperature, especially in the presence of protic impurities.[30–34] $LiPF_6$ is thought to decompose to form LiF and PF_5. PF_5 catalyzes the decomposition of organic carbonates. This is commonly observed by the colour change of electrolytes stored at high temperature (60°C).[33,35]

1.2 PARASITIC REACTIONS BETWEEN ELECTRODES AND THE ELECTROLYTE

The lifetime of a rechargeable cell depends on the degree of reversibility of a discharge-charge cycle. Parasitic reactions are reactions other than the desired charging and discharging of a cell. The effects of these reactions include lithium inventory loss (capacity loss), gas evolution (swelling), depletion of electrolyte (conductivity loss) and impedance growth (power loss). The parasitic reactions between electrodes and the electrolyte under normal conditions fall into three categories: reaction of the electrolyte at one electrode, one-way "cross-talk", and two-way "cross-talk". These three reactions are described in more detail below.

1.2.1 Parasitic Reactions at One Electrode

Parasitic reactions of the electrolyte at one electrode could be either the reduction of electrolyte at the negative electrode, or the oxidation of electrolyte at the positive electrode. The initial reduction of electrolyte species to form a passivating SEI is a desirable parasitic reaction, because this hinders further reactions with the electrolyte. However, formation of the SEI consumes active lithium from the negative electrode, resulting in irreversible capacity loss. Typically, 5-10% of the cell capacity is lost during the first cycle, in part due to SEI formation.[36] If the SEI is not fully passivating, then reduction of electrolyte and capacity loss continue. This lack of passivation may cause thickening of the negative electrode SEI, as shown in Figure 1.2.1a. The best-known example for this type of reaction is the two-electron reduction of EC to form lithium ethylene dicarbonate, a prominent SEI component, by Equation (3).[29]

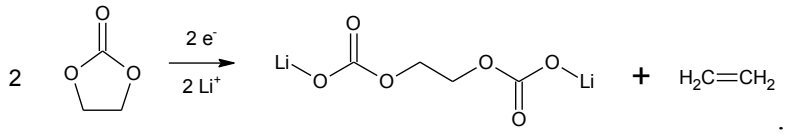

(3)

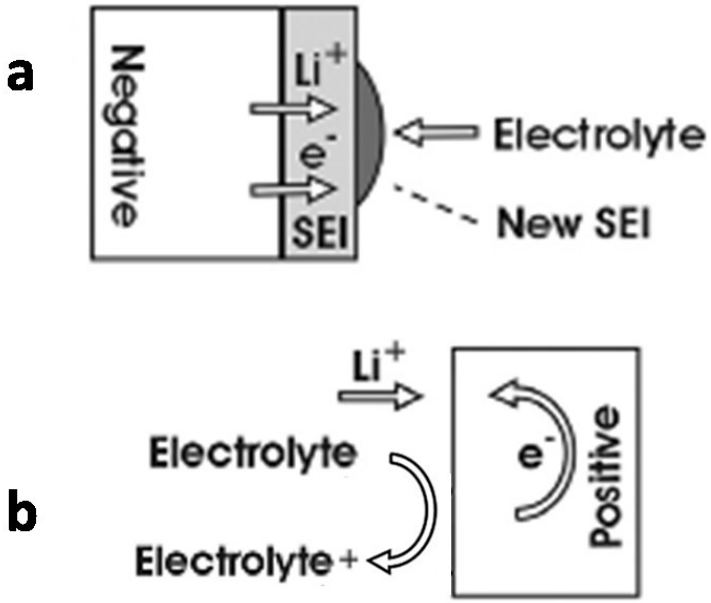

Figure 1.2.1: an illustration of parasitic reactions involving one electrode: a) reduction of electrolyte at the negative electrode, b) oxidation of electrolyte at the positive electrode. This figure is reproduced, with permission, from A. J. Smith, J. C. Burns, D. Xiong, and J. R. Dahn, J. Electrochem. Soc., 158, A1136–A1142 (2011). Copyright 2011, the Electrochemical Society

Similar reactions occur at the positive electrode, shown in Figure 1.2.1b. Oxidation of electrolyte at the positive electrode results in the reduction of a transition metal ion in the positive electrode and the insertion of a lithium ion from the electrolyte into the positive electrode, to maintain charge balance. Addition of a lithium ion into positive electrodes increases its chemical potential and causes a decrease in cell voltage. On the first cycle, electrolyte is oxidized to form an initial SEI. Continued high voltage cycling can cause

thickening of the positive electrode SEI;[15] however some of the products of electrochemical electrolyte oxidation are thought to be soluble in electrolyte.[37]

1.2.2 One-Way Chemical Dialogue

The reaction of electrolyte at one electrode can result in soluble species that react at the opposite electrode. This is sometimes called "chemical dialogue" or "cross-talk".[3,38–40] Evidence for these reactions is a major subject of this work and will be discussed at length in Chapter 3. Figure 1.2.2a shows cross-talk from the positive electrode: electrolyte is oxidized (as in Figure 1.2.1b); the oxidized species migrates to the negative electrode, where it is reduced to form a species *R*. Figure 1.2.2a shows *R* as an insoluble solid (an SEI species), but *R* could be either soluble, a liquid or a gas. Figure 1.2.2b shows cross talk from the negative electrode: the electrolyte is reduced, and the reduced species migrates to the positive electrode, where it is oxidized to form some species *R*. Chemical dialogue reactions of the type described by Figure 1.2.2 result in reversible capacity loss, a decrease in cell voltage, and depletion of electrolyte species. The capacity lost is reversible because the lithium that is removed from the negative electrode is re-inserted into the positive electrode, so there is no loss of active lithium.

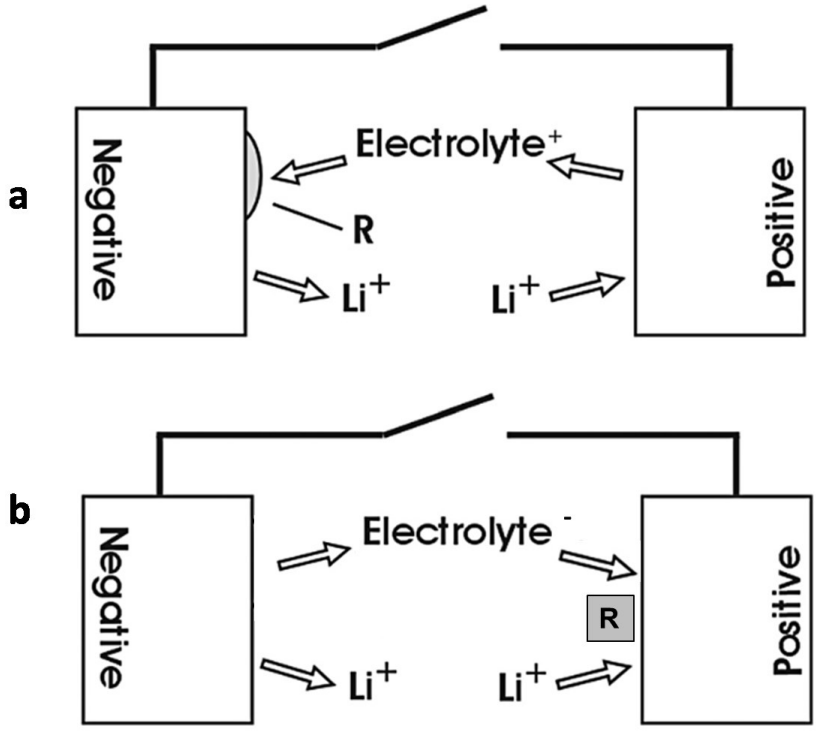

Figure 1.2.2: an illustration of parasitic reactions involving both electrodes in one-way chemial dialogue, a) chemical dialogue from the positive electrode, b) chemical dialogue from the negative electrode. *R* indicates a unknown species, from the decomposition of an electrolyte decomposition product. This figure is adapted, with permission, from A. J. Smith, J. C. Burns, D. Xiong, and J. R. Dahn, J. Electrochem. Soc., 158, A1136–A1142 (2011). Copyright 2011, the Electrochemical Society.

1.2.3 Two-Way Chemical Dialogue

Two-way chemical dialogue occurs when the decomposition of electrolyte (or some other species) at one electrode is reversible upon reaction at the opposite electrode. Two-way chemical dialogue is sometimes called a "shuttle" reaction, because it causes species to travel in a cycle between the two electrodes.[3,41] Figure 1.2.3 shows a shuttle reaction that startes at the positive electrode, where an electrolyte species is oxidized; the oxidized species diffuses to the negative electrode, where it reduces to re-form the original species, which again is oxidized at the positive electrode. The shuttle reaction may also begin at

the negative electrode, with the reduction of an electrolyte species. Shuttle reactions cause reversible capacity loss and voltage drop.

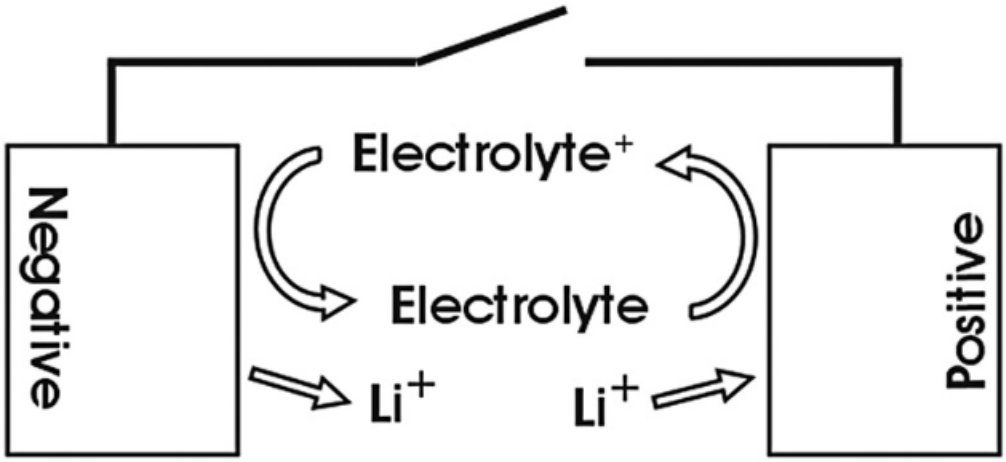

Figure 1.2.3: an illustration of reversible chemical dialogue between negative and positive electrodes. This figure is adapted, with permission, from A. J. Smith, J. C. Burns, D. Xiong, and J. R. Dahn, J. Electrochem. Soc., 158, A1136–A1142 (2011). Copyright 2011, the Electrochemical Society.

1.3 Concluding Remarks

The purpose of this thesis is to better understand the parasitic reactions occurring in lithium-ion cells. Chapter 2 summarizes the experimental techniques used in this thesis. In Chapter 3, evidence of one-way chemical dialogue is presented. In the previous section, the species that carried out chemical dialogue were called "some unknown species, *R*". In Chapter 3 it is shown that CO_2, from the positive electrode is one such species, *R*, as it is subsequently consumed at the negative electrode.[42,43] The effects of CO_2 reduction on the chemistry of the negative electrode SEI is determined using x-ray photoelectron spectroscopy (XPS), a technique used to determine the chemical composition of surfaces. XPS is also used to observe the effect of cross-talk on the

positive electrode SEI.[44] Chapter 4 investigates the evolution and consumption of gases other than CO_2 in lithium-ion cells (H_2, C_2H_4, and CO).[43] The possible chemical mechanisms for the consumption of these gases are discussed, as well as the effects that these might have on cell performance. Chapter 5 investigates the effects of gas consumption on cell performance, to see whether gas consumption is a parasitic reaction that harms cell performance, or whether it improves performance by contributing to a passivating SEI.[43] Chapter 6 explores how the conditions during the first charge of a lithium-ion cell (time, temperature, and voltage) affect the passivating qualities of the initial SEI. Chapter 7 introduces a new technique for quantifying electrolyte composition using Fourier transform infrared spectrometry (FTIR) and machine learning (ML).[45] This tool is expected to be very useful for analyzing the changes in electrolyte composition in aged lithium-ion cells. It is hoped that the tools, techniques and chemical insights developed in this thesis will help others understand more about the aging mechanisms of lithium-ion cells. It is hoped that understanding the chemical mechanisms for cell aging will allow for targeted ways of preventing these reactions, so that the lifetimes of lithium-ion cells can be extended.

CHAPTER 2 EXPERIMENTAL TECHNIQUES

2.1 LITHIUM-ION POUCH CELL FABRICATION

Many different cell types were used in this thesis. Each chapter includes adescription of the cell chemistry used. What follows here is a general description of the cells used in this thesis. All cells were machine-made (402035-size) pouch cells (the cell casing was a flexible aluminum laminate material). The cells were ~2 mL in volume. They were obtained sealed, without electrolyte, from LiFun Technologies (Xinma Industry Zone, Golden Dragon Road, Tianyuan District, Zhuzhou City, Hunan Province, PRC, 412000). The negative electrodes of these cells contained 96% artificial graphite, 2% carbon black conductive diluent, and 2% binder (sodium carboxymethylcellulose and styrene butadiene rubber). The positive electrodes contained 96% NMC, 2% carbon black and 2% PVDF binder in all cases except one. The positive electrodes containing single-crystalline NMC532, discussed in Chapter 6, were comprised of a 94:2:2:2 wt. % blend of NMC, carbon black, graphite and PVDF. The capacities of these cells ranged between 200 and 290 mAh (depending on the cell type). Prior to filling with electrolyte, the cells were opened and dried under vacuum (<100 mtorr) for 14 hours at 100°C, to remove residual moisture. The cells were then transferred to an Ar-filled glovebox without exposure to air.

2.1.1 Electrolyte Filling and Wetting

To each cell 0.85 mL of electrolyte was added. This amount was in slight excess of the volume required for adequate electrode wetting. The electrolyte salt was $LiPF_6$ in every case (1 M in Chapters 3-5, 1.2 M in Chapters 6 and 7). The solvent was EC:EMC 3:7 wt.unless otherwise specified. No electrolyte additives were used, unless specified. The purities and suppliers of the electrolyte components are listed in Table 2.1.1. After filling the cells with electrolyte, the cells were put under vacuum (~ -90 kPa for 60 seconds) to help electrolyte fill the electrode pores. The aluminum-laminate cell casings were vacuum sealed at 165°C, under a gauge pressure of -90 kPa, using a vacuum heat sealer (Model MSK-115V from MTI Corp.).

Table 2.1.1: abbreviations, suppliers and purities for the electrolyte components and additive blends.

Electrolyte component	***Abbreviation***	***Supplier***	***Purity, water content***
	solvents		
ethylene carbonate	EC	BASF	99.95%
ethyl methyl carbonate	EMC	BASF	99.9%, < 20 ppm H_2O
dimethyl carbonate	DMC	BASF	99.99% < 10 ppm
	salt		
$LiPF_6$		BASF	99.94%, 14 ppm H_2O
	Electrolyte additives		
vinylene carbonate	VC	BASF	99.97%, < 100 ppm H_2O
fluoroethylene carbonate	FEC	BASF	99.94%
1,3 propane sultone	PES	Lianchuang	98.20%
ethylene sulfate	DTD	Yacoo	> 98%
5,2,4-dioxadithiane-2,2,4,4-tetraoxide	MMDS	Tinci	98.7%
tristrimethylsilyl phosphite	TTSPi	TCI America	> 98%
	Ternary electrolyte blends		
	PES211: 2% PES, 1% DTD, 1% TTSPi		
	PES222: 2% PES, 2% DTD, 2% TTSPi		
	VC211: 2% VC, 1% MMDS, 1% TTSPi		

2.1.2 Formation and Degassing of Lithium-ion Pouch Cells

After filling with electrolyte, the cells were held at 1.5 V for 24 hours. This allowed time for the electrolyte to permeate the electrodes. The voltage of 1.5 V was applied to prevent oxidation of the copper current collector, which occurs above 3.2 V vs. Li/Li^+. Cells were clamped tightly inside polyethylene holders, using metal shims to sandwich the cells tightly between rubber blocks (approximately the same size as the pouch cell). The rubber blocks were made from 5/8" medium-hard rubber (McMaster Carr, part number 5508T45). The pressure exerted on the cell by this type of clamping method is approximately 5-10 psi. If pouch cells are not clamped, gas evolution, if it occurs, can decrease the stack pressure between the electrodes. This can cause inhomogeneous lithiation of the negative electrode, which can lead to lithium plating. After wetting the cells were transferred to a 40.0 ± 0.1°C temperature-controlled box, and charged using a Maccor 4000 series test system. The first cycle of a lithium-ion cell is often called "formation". Unless otherwise specified, the formation procedure was as follows. Cells were charged to their upper voltage using a current that would fully charge the cell in 20 hours—this current is referred to henceforth as "C/20", where C stands for the cell capacity and 20 is the number of hours for the cell to be fully charged (for example, a C/20 current for a 200 mAh cell is 10 mA). The cells were held at the upper voltage limit for one hour, followed by a C/20 discharge to 3.8 V, where they were held for another hour. During the first charge EC and other electrolyte components reduce, forming the negative electrode SEI and causing gaseous by-products. To degas the cells, they were

transferred to an Ar-filled glove box, where the cell casings were cut open to release the gas. The cells were then resealed under -90 kPa gauge pressure.

2.2 POUCH BAG ASSEMBLY

To probe the reactivity of individual electrodes, charged electrodes were removed from cells and sealed in separate "pouch bags". These "pouch bags" were made from the same aluminum laminate material as the pouch cells used in this work (Contemporary Amperex Technologies Limited, Ningde, Fujian, 352100, China). Figure 2.2.1 illustrates the pouch bag assembly process. Pouch bag experiments were pioneered in the Dahn lab by Deijun Xiong and are described in several publications.[42,44,46,47]

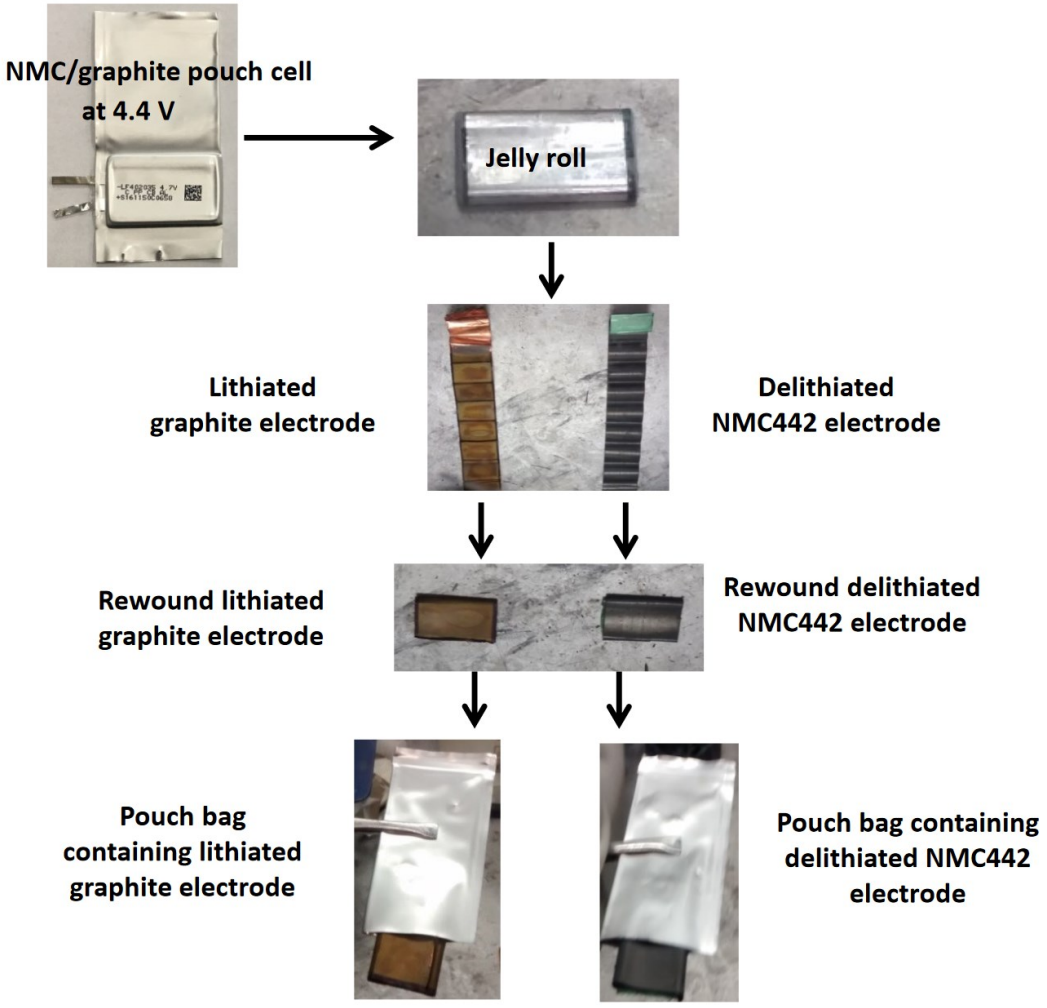

Figure 2.2.1: assembly of pouch bags containing individual charged electrodes. This figure is adapted with permission from D.J. Xiong, Surprising Chemistry in Li-ion Cells, PhD thesis, Dalhousie University, Halifax, NS, Copyright (2017).

To probe the reactivity of individual electrodes with gases, Deijun Xiong's pouch bags were modified so that they could be inflated with gas. One of these inflatable pouch bags is shown in Figure 2.2.2a. Rubber septa (Thermo Scientific, C4000-30) were adhered to the outside of the pouch bags using a generous amount of adhesive. At first, super glue (Gorilla Glue Inc.) was used. Later silicone sealant ('Silicone 1', General Electric) was

found to be more reliable. In addition to a charged electrode, one ¼ inch stainless-steel ball was placed in each pouch bag approximately underneath the rubber septum. The pouch bags were sealed under vacuum in the same manner as the pouch cells described above. The purpose of the stainless steel ball was to create space in the pouch bag for a syringe needle to pass through the rubber septum, puncturing only the single layer of aluminium-laminate directly under the rubber septum without puncturing the other side of the bag, thus avoiding a leak in the bag. The pouch bags were inflated with ~8 mL of CO_2, H_2, C_2H_4 or CO (>99.99%, Praxair Technology Inc.) using a syringe. After inflation with gas, the casings of the pouch bags were heat-sealed a second time, below the rubber septum, creating a gas-tight seal equivalent to that of a pouch cell once the rubber septum was cut away.

To determine if the CO_2-inflated and the H_2-inflated pouch bags were gas-tight, their volume changes were measured after 3 hours of storage at an external gauge pressure of -0.01 kPa. The H_2-inflated pouch bags were afterwards stored for an additional week at 60°C. Figure 2.2.2b shows that volume change of inflated aluminum laminate pouch bags is positive after storage, suggesting that the aluminum laminate cell casing does not leak, and that it deforms inelastically to accommodate the expansion of gasses. The expansion in volume (0.1-0.4 mL) is small compared to the volume of the inflated pouch bag (~6 mL). All inflated pouch bags in this work were submerged under water before and after testing for visual inspection for leaks.

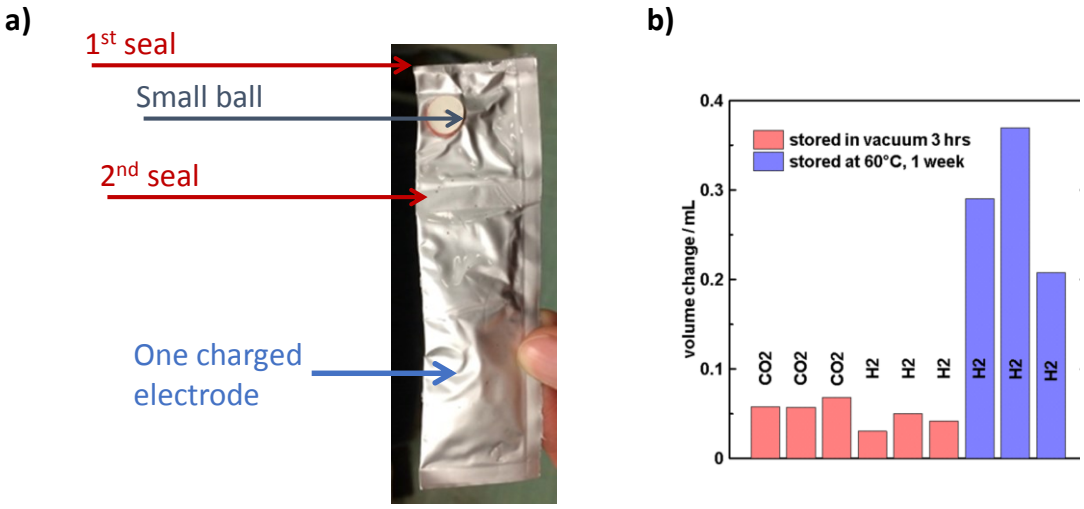

Figure 2.2.2: a) an inflatable pouch bag, b) results of the inflated pouch bag leak tests. Reproduced with permission from *J. Electrochem Soc.*, **164**, A3518 (2017). Copyright 2017, The Electrochemical Society.

To better simulate the environment of a pouch cell, c harged negative electrodes were stored in inflated pouch bags with 0.5 mL of electrolyte (1M $LiPF_6$ in EC:EMC). Positive electrodes were rinsed with three 2 mL aliquots of DMC and dried (first under argon, then under vacuum) to remove all electrolyte before being stored in CO_2-inflated pouch bags, so that gas evolution and impedance growth from electrolyte oxidation would not occur.

2.3 Quantification of Gas using Archimedes' Method

The volume change of cells or pouch bags was measured using Archimedes' method. According to Archimedes' principle, the upward buoyant force exerted on an object immersed in a fluid is equal to the weight of the fluid displaced by the object. If the

submerged object is hanging from a hook, the force of gravity, mg, on the object is equal to the buoyant force, B plus the force of tension from the hook, T, as in Equation (4)

$$mg = T + B. \quad (4)$$

If the volume of the object changes, B and T must also change (from B_1 to B_2 and T_1 to T_2). If the object does not change in mass, remains submerged and suspended from the hook, then Equation (5) applies:

$$mg = T_1 + B_1 = T_2 + B_2. \quad (5)$$

Figure 2.3.1a illustrates Equation (5), showing a pouch cell before and after gas evolution, submerged under a fluid, while hanging from a hook. Pouch cells are encased in a flexible aluminum laminate material that can expand to accommodate gas evolution. The change in volume in mL, V, of a cell is the same as the change in B if the fluid used to submerge the object has a density of 1.00 g/mL (such as water at room temperature), as shown by Equation (6)

$$T_1 - T_2 = \Delta B = \Delta V_{displaced\ water}(1\ \text{g/mL}) = \Delta V_{object}(1\ \text{g/mL}). \quad (6)$$

T, and therefore ΔV of a cell, can be measured using a strain gauge or the underhook of a balance. Atmospheric pressure fluctuations (99-102 kPa) may cause a 3% uncertainty in these measurements.

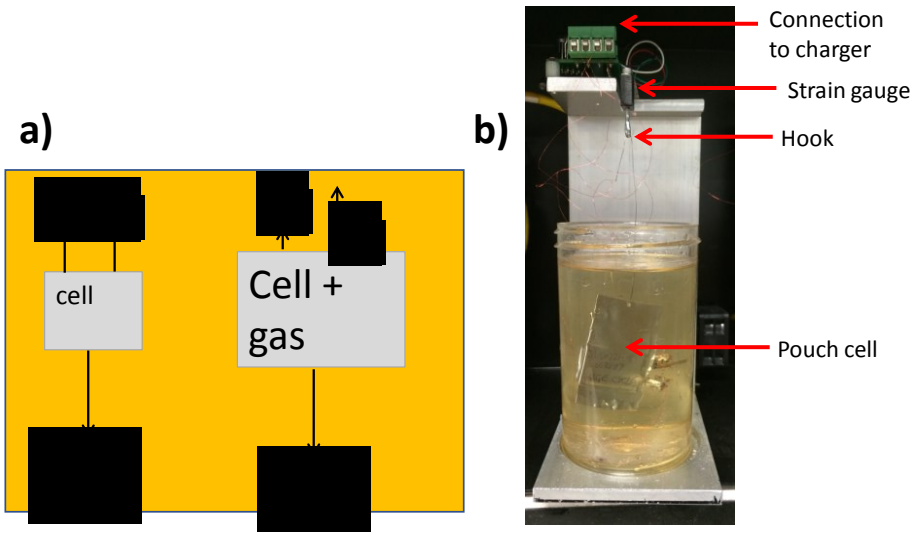

Figure 2.3.1: a) free body diagram of a cell hung from a hook while submerged under fluid, before and after gas-evolution causes a volume change, b) a photograph of the apparatus to measure gas evolution *in-situ*.

Figure 2.3.1b shows the apparatus used to measure changes in cell volume *in-situ,* as a function of time during cycling. This apparatus was designed and built at Dalhousie University, and is described in several publications.[48–50] Data from the strain gauge is collected by a computer and combined with the cycling data. The fluid in Figure 2.3.1b is silicone pump oil, which was chosen so that the cell can be cycled at 40 or 60°C without fluid evaporation, and so that the submerged cells could be charged beyond 4 V without decomposing the fluid. To determine the difference in volume before and after a test, *ex-situ* volume change measurementswere done at room temperature, by weighing cells suspended from a fine wire attached to the underhook of an analytical balance (Shimadzu, AUW200D). The cells were submerged under de-ionized water (18.2 MΩ/cm, Thermo Scientific Barnstead NANOpure Water Purification System).

2.4 ELECTROCHEMICAL TESTING

2.4.1 Cycling

Cell cycle life was tested by repeatedly charging and discharging and observing the decrease in cell capacity. The capacity, *Q*, of a cell is the amount of charge that it can store, often expressed in mAh (the product of the current in mA and the cycle duration in hours). The capacity of a cell, Q, is sometimes appended with the subscript *d* or *c* to indicate the capacity on the discharge or the charge cycle. A cell was considered to have failed once Q_d was depleted to 80%. Neware-brand cyclers were used for long-term cycling.

2.4.2 Ultra High Precision Cycling

A decent lithium-ion cell will cycle for many years before its capacity is depleted to 80%. Ultra High Precision Cyclers (UHPC) were invented in the Dahn lab for quickly ranking the expected lifetimes of lithium-ion cells. UHPCs measure the current coming in and out of a cell with much higher accuracy and precision than other cyclers, allowing for the coulombic efficiency (CE, the ratio of Q_d to Q_c) to be determined to many decimal places.[51] Many studies have confirmed that UHPC is often able to predict the order in which cells will fail in long-term cycling experiments, based on their relative CEs.[52–55]

A low CE indicates the increased presence of parasitic reactions. Since CE is the ratio of Q_d to Q_c, it is lowered when Q_d decreases and when Q_c increases. Q_d decreases when

parasitic reactions cause irreversible capacity loss (consumption of active lithium). Capacity loss can be caused by reduction of electrolyte at the negative electrode, as discussed in Section 1.2.[3] Q_c increases when parasitic reactions (such as chemical dialogue or shuttle reactions) cause self-discharge, re-insertion of lithium into the positive electrode. More electrons are needed in the charge cycle to compensate for this, resulting in an apparent increase in Q_c.[3] This causes the charge endpoint capacity to increase on every cycle. For example, a hypothetical cell with on-going chemical dialogue may have a charge endpoint capacity of 200 mAh on the first cycle, and a charge endpoint of 202 mAh on the second cycle. The additional 2 mAh is called "charge endpoint capacity slippage", or sometimes "slipC" for short. By quantifying the capacity loss and slipC, the contributions of different parasitic reactions to the overall CE can be determined.

Cells for UHPC cycling were clamped, as described before, and kept in temperature-controlled boxes at 40.0 ± 0.1°C. They were cycled using a constant current of C/20 \. The cells were cycled between 2.8 V and the desired upper voltage. After 20 cycles, the cells were equilibrated at 3.8 V.

2.4.3 Storage

Parasitic reactions at the positive electrode cause re-insertion of lithium into the positive electrode, resulting in a decrease in positive electrode potential and a decrease in cell voltage. Measuring the open-circuit voltage of a fully charged cell as a function of time allows these reactions to be quantified. Storage is often done as a preliminary test before

UHPC cycling, since self-discharge in storage and charge slippage in UHPC are correlated. The storage systems in the Dahn lab were built in-house.[56] These instruments measure cell voltage at regular intervals, while the cells are stored open-circuit in temperature-controlled boxes.

2.4.4 Electrochemical Impedance Spectroscopy

Electrochemical impedance spectroscopy (EIS) was used in this work to measure the charge-transfer impedance (R_{ct}) of cells and electrodes. In EIS, small sinusoidal voltages are applied to a cell at different frequencies. The voltages must be small enough to elicit a linear current response from the cell. A cell's electrodes have capacitive properties (due to charging of the double layer at the electrode interface) that delay the current elicited from the cell when the frequency of the voltage change is low. Electrodes also have resistive properties (due in part to diffusion of lithium-ions through an SEI) that reduce the amplitude of the current. EIS data is commonly plotted as a Nyquist plot, where the real part of the impedance is plotted on the x-axis and the negative imaginary part of the impedance (from the capacitor) is plotted on the y-axis. The simplest circuit model of a cell, shown in Figure 2.4.1a, has the solution resistance, R_s, in series with R_{ct} and a double layer capacitor, C_{dl} in parallel.[57] A Nyquist plot for such a cell is shown in Figure 2.4.1b. The high-frequency x-intercept gives the magnitude of R_s. The diameter of the semi-circle in the Nyquist plot is the magnitude of R_{ct}.

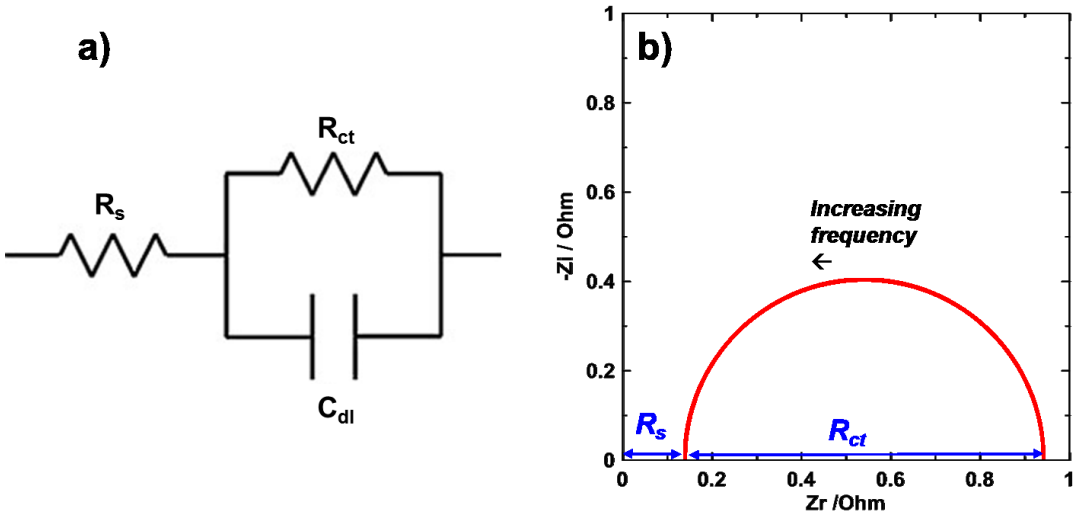

Figure 2.4.1: a) a simple circuit for modeling an electrode in a lithium-ion cell; b) a representative Nyquist plot for such a cuircuit.

The simple circuit model of a cell in Figure 2.4.1a does not accurately represent a lithium-ion cell, which contains two electrodes with dissimilar C_{dl} and R_{ct} values. The Nyquist plot of a lithium-ion cell is not a perfect semi-circle, but rather an oblong shape in which two overlapping semicircles (from the two electrodes) are sometimes distinguishable. In this work, R_{ct} of a full cell is taken to be the diameter of this mid-frequency feature. The R_{ct} of a single electrode (either positive or negative) is determined by EIS analysis of a symmetric cell, which contains identical electrodes of one type.[20] Construction of a symmetric cell is described in the following section.

EIS measurements were performed using a BioLogic VMP3 potentiostat, inducing a 10 mV bias, at frequencies ranging from 100 kHz to 10 mHz. All cells were equilibrated at 10.0 ± 0.1° C before measurement. Full cells were equilibrated at 3.8 V.

2.4.5 Symmetric Cell Construction

Electrodes (disks 1.14 cm^2 in diameter) were punched from the same pouch cell electrode and assembled into symmetric cells, using 2325-type coin cell hardware, shown in Figure 2.4.2. Blown-microfiber (3M Co) was used as a separator and the electrolyte was 1 M $LiPF_6$ in EC:EMC 2:7 wt. ratio (no additives). Electrodes for positive/positive symmetric cells were cut from the part of the pouch cell electrode that was coated only on one side of the current collector, since the positive electrode materials are poorly conductive and would yield large contact impedances.

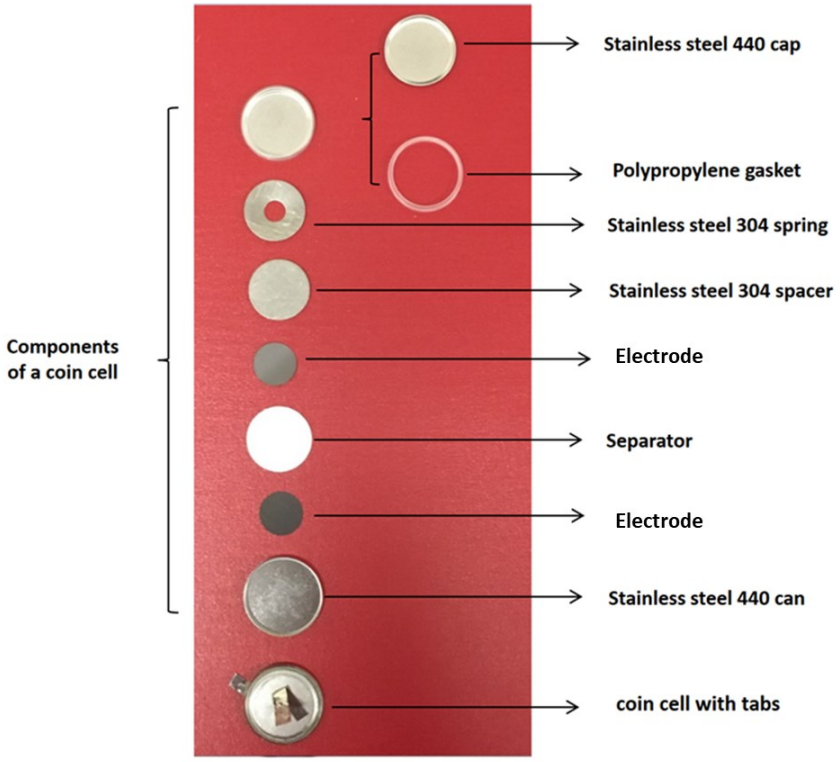

Figure 2.4.2: components of a coin cell. This figure is adapted with permission from D.J. Xiong, Surprising Chemistry in Li-ion Cells, PhD thesis, Dalhousie University, Halifax, NS, Copyright (2017).

2.5 GAS CHROMATOGRAPHY

Gas chromatography (GC) is a method of separating a mixture of gases by passing them through a long, thin column, where they are retained to varying degrees. Columns can be filled or coated with materials that retain compounds based on polarity (using a polar stationary phase, such as silica) or based on size (using stationary phases like zeolites or molecular sieves). Samples are introduced to the column through an injection port. The injection port and the column are heated to keep liquid analytes in the gas phase, and to reduce their retention times. After the samples are eluted from the column they pass to a detector.

2.5.1 GC Analysis of Liquid Electrolyte

A mass spectrometer (MS) was used in this work to detect the components in liquid samples. After separation by GC, molecules are ionized by bombarding them with high-energy electrons. Molecules sometimes fragment when ionized and do so in characteristic ways. The ionized molecules and ionized fragments are separated according to their mass-to-charge, *m/z,* ratio using a quadrupole mass spectrometer. This consists of four cylindrical electrodes spaced equidistant from each other. Ionized particles are passed through the centre of the four electrodes. Oscillating voltages are applied to the two pairs of opposing electrodes such that only particles of a desired *m/z* ratio travel straight through the quadrupole without being deflected. The voltages can be varied such that all *m/z* ratios are scanned sequentially as a compound elutes. This is called “total ion

monitoring". The eluted compound is identified by matching its unique fragmentation pattern to a database.

A Bruker 436 GC coupled to a Bruker Scion single quadrupole MS was used for the analysis of liquid electrolytes. The GC used a split injection with helium as the carrier gas, flowing at a rate of 1.3 mL/min. The column (BR-5MS) was 30 m long, with an internal diameter of 0.35 mm, and a 1 μm thick dimethyl arylene siloxane-based coating. The oven temperature ramped from 40°C to 240°C, at a rate of 30 °C/min to 240°C, to maximize peak quality. The MS transfer line was held at 270°C. The ion source was set to 270°C, and the electron energy was 70 eV. A minimum five-point calibration curve was used to determine the relative amounts of known compounds present in each sample. Analytes included DMC, EMC, VC, DEC, FEC, EC, dimethyl-2,5-dioxahexane carboxylate (DMOHC) and diethyl-2,5-dioxahexane carboxylate (DEOHC). Although absolute amounts are not known for the cell, the method allows for semi-quantitative analysis.

To obtain samples for MS, liquid electrolyte was extracted from discharged cells using a centrifuge. In this process, the cell casings were cut along the top and bottom of the cell just before they were sealed in 15-mL polypropylene centrifuge vials. The vials were centrifuged at 2200 rotations per minute for 20 minutes at 30°C. The cells were immediately removed from the vials after centrifuging, and the electrolyte was taken from the vial using a syringe. One drop of this electrolyte was added to a perfluoroalkoxy polymer vial containing 10 mL of dichloromethane (to extract the organics) and ~0.1 mL

of pure water (18.2 MΩcm, Barnstead Nanopure Diamond) to extract the $LiPF_6$. The vials were shaken twice in 15-minute intervals, then centrifuged at 2200 RPM, for 20 minutes, at 20°C. This procedure, developed by Petibon *et al*.,[58] ensured that salts were adequately removed from the organic layer, as these are not suitable for GC-MS analysis. The organic (dichloromethane) layer was then injected into the GC-MS.

2.5.2 GC Analysis of Gases

A thermal conductivity detector (TCD) was used to detect the components of gaseous samples. A TCD measures the thermal conductivity of the gas eluting from the GC and comparing it to that of pure carrier gas flowing through a reference cell. A TCD cell is comprised of a heated chamber containing a filament heated to a higher temperature. Gas flowing through the cell conducts heat from the filament to the chamber walls at a rate proportional to its thermal conductivity. This method is appropriate for characterizing mixtures of H_2, N_2, CO, CO_2 and light hydrocarbons.

A Bruker 436 GC coupled to a Bruker TCD detector was used for the analysis of gases. A custom-made molecular sieve column (Bruker, 10 m, 0.32 mm ID, 30 μm coating) in parallel with a "porous layer open tubular" column (Bruker, 50 m, 0.53 mm ID, 20 μm coating) was used, which allowed for optimal separation of H_2, CO, CO_2, Ar, N_2 and light hydrocarbons. The oven temperature was set to optimize the separation of the compounds while minimizing their retention times. The oven was held at 33°C for 8.5 minutes, then ramped at 15°C/minute to 160°C. The carrier gas was argon, flowing at a rate of 9

mL/min. The TCD temperature was set to 230°C and the filament temperature was set to 370°C.

A "gas extraction device" (GED) was used to remove gas from cells for GC analysis. The GED was designed and built in the Dahn lab.[59] Cells were placed inside GED, which was then evacuated to 60 mbar. A sharp piston was lowered in the GED to puncture the cell casing. The GED was filled with argon gas (>99.99%, Praxair Technology Inc.) to atmospheric pressure. 200.0 μL of the gas mixture was injected into the GC-TCD. The procedure was repeated with a pair sample to ensure reproducibility.

To enable quantitative analysis, the response of the GC-TCD was tested with a calibration gas specially prepared by Praxair, containing 10% by volume of the following gases: H_2, N_2, CO, CO_2, CH_4, C_2H_4, C_2H_6, C_3H_6, C_3H_8, and C_4H_{10}. 1 mL of this calibration gas was injected into the evacuated GED and introduced into the GC in the same way as the gaseous samples described above. The magnitude of the signal resulting from the gases in the calibration mixture was determined by integrating the peaks in the chromatograph and dividing by the volume of the gas that was injected.

2.6 Fourier Transform Infrared Spectroscopy

Fourier transform infrared spectroscopy (FTIR) is a technique for measuring the absorbance of infrared light by a sample. Infrared light can excite motion (twisting, bending, stretching) in molecular bonds. The wavelengths of light that induce motions are absorbed by the molecule and are not transmitted. Different chemicals have varied

molecular geometries, undergo different motions when excited, and thus absorb different wavelengths of infrared light. FTIR is commonly used for identifying the functional groups in an unknown substance. For example, alcohols are easily identified by a strong, broad absorption between 3550-3200 cm^{-1}, corresponding to an O-H stretch.

FTIR spectroscopy is faster than dispersive IR spectroscopy (where data is collected one wavenumber at a time). FTIR applies a Fourier transform to the light emerging from a sample after passing through an interferometer. This allows an absorption spectrum to be collected in a small amount of time. The simplest interferometer is a Michelson interferometer. It consists of a beam splitter that directs light onto perpendicular mirrors, one of which is movable, and is shown in Figure 2.6.1. Infrared light reflected from the mirrors converges at the beam splitter, interacts with a sample and is directed to a detector. When the movable mirror is the same distance from the beam splitter as the stationary mirror, the light emitted to the detector is intense, because the converging light waves are in phase. When the movable mirror is at any other position, some wavelengths of light are out of phase, causing an interference pattern that modifies the intensity of the emitted light. Data collected by the detector (intensity vs. time) as the mirror oscillates is processed into a spectrum (intensity vs. wavenumber) by applying a Fourier transform.

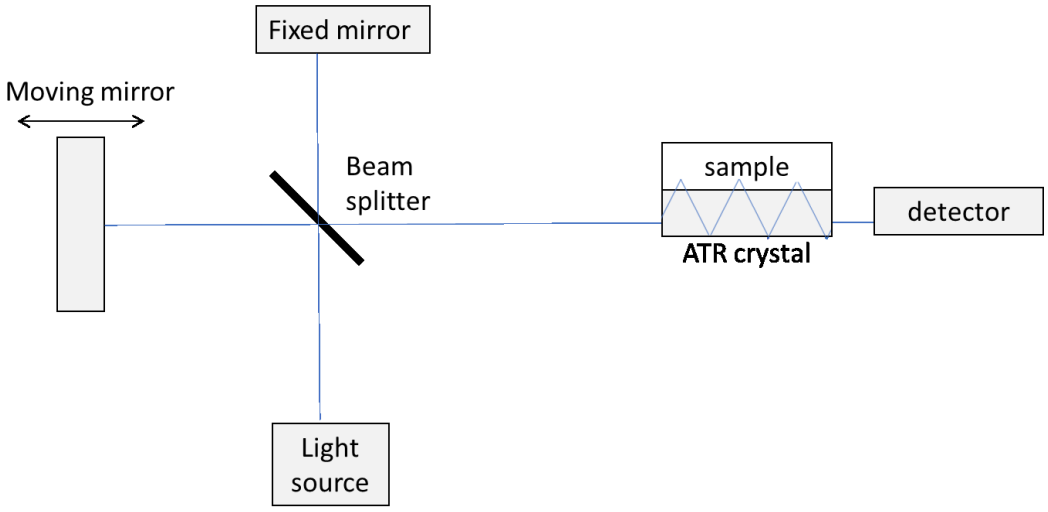

Figure 2.6.1: block diagram of an FTIR with an ATR accessory.

The FTIR instrument used in this work had an attenuated total reflectance (ATR) accessory. ATR-FTIR spectra are obtained by passing light through a crystal that is in direct contact with a sample, causing an evanescent wave to protrude a short way into the sample. This is different from traditional transmission FTIR, in which IR light is transmitted through a sample. The ATR accessory was very convenient for the analysis of liquid electrolyte from lithium-ion cells, since there was no need for transparent cuvettes or large volumes of electrolyte. One drop of electrolyte was sufficient to cover the ATR crystal. Between analyses of different electrolytes, the crystal was cleaned with methanol and a Kimwipe.

FTIR spectra in this thesis were collected using a Cary 630 FTIR (Agilent Technologies) equipped with a germanium crystal ATR accessory. Sixteen scans were collected for each background and sample measurement, at a resolution of 4 cm^{-1}, using MicroLab PC

software. All measurements were performed in a thermostatic room (Coldmatic Refrigeration) maintained at 12 – 14°C to hinder evaporation of electrolyte.

2.7 X-RAY PHOTOELECTRON SPECTROSCOPY

X-ray photoelectron spectroscopy (XPS) is a method for determining the chemical composition of surfaces. In this thesis it is used for studying the SEI of electrodes. XPS uses the photoelectric effect to generate electrons from a sample that have binding energies (BEs) that are characteristic of the element from which they came. A sample is irradiated with photons that have sufficient energy, hv, to eject core electrons from atoms on the surface of a sample. The binding energy of these electrons can be calculated from their measured kinetic energy (KE) through the following relationship

$$\mathrm{BE} = hv - \mathrm{KE} - \Phi_{sp} \qquad (7)$$

where Φ_{sp} is the work function of the spectrometer. The binding energy of a photoelectron is characteristic of the atomic orbital from which it was ejected and is modified by the oxidation state of its parent atom. A photoelectron from an atom with a higher oxidation state will have a higher binding energy, relative to the neutral atom, since the electron is more tightly bound to its electron-deficient environment. An atom with a lower oxidation state will have a lower binding energy, relative to the neutral atom, as electron-electron repulsion makes the electron less tightly bound. Careful analysis of binding energy shifts, with the aid of peak-fitting and reference tables, can be used to elucidate the oxidation state of atoms at the surface of a sample. The following paragraphs describe an XPS experiment in chronological detail.

2.7.1 Sample Preparation and Data Acquisition

The electrodes to be analyzed by XPS were removed from their cells in an argon glovebox. Samples were cut from the middle of the electrodes and rinsed several times with 1 mL aliquots of EMC to remove $LiPF_6$ and EC, which are not ultra-high vacuum (UHV, $<10^{-9}$ mbar) compatible. UHV is required by XPS because photoelectrons must travel a long distance from the sample to the detector without modification to their KE. Rinsing with EMC is not expected to dissolve any SEI components, since EMC is the major component of the electrolyte in which the SEI was formed. The dried samples were mounted onto sample holders with double-sided, UHV-compatible copper tape. The sample holder was transferred into the loading chamber of the XPS system (SPECS) without exposure to air, using an air-tight apparatus designed and built at Dalhousie University.[15] Samples were kept in the loading chamber until its base pressure returned ($\sim 2x10^{-8}$ mbar). They were then transferred to the preparation chamber where they were equilibrated to UHV. The samples were then transferred to the analysis chamber, which had a base pressure of $\sim 2x10^{-10}$ mbar.

During spectral acquisition, the sample was irradiated with unmonochromatized x-radiation from the k_α transitions of a Mg anode. These x-rays cause photoelectrons to be ejected from the surface of the sample, which then travel to the analyzer (Phoibos 150). The analyzer is consists of lenses and a hemispherical capacitor. The voltage applied to the lenses sweep such that only electrons of a certain KE are decelerated to a "pass

energy" (typically 20 eV). The photoelectrons then travel through the hemispherical capacitor, which selects the electrons with the correct pass energy. The electrons emerging from the hemispherical capacitor are counted by a detector. The rate of counts (counts per second, CPS) is plotted vs. the BE of the photoelectrons. A region of interest (for example, the region where C 1s photoelectrons appear, between 284-292 eV) is scanned several times to increase the signal-to-noise ratio.

2.7.2 Data Interpretation

Data analysis was done using CasaXPS software (v. 2.3.18). First a Shirley background was fit around the peak area. A Shirley background is fit iteratively such that it descends with increasing KE in proportion to the integral of counts at higher KE, to account for inelastically scattered photoelectrons. In this thesis the spectra are plotted as CPS vs. BE, sometimes with the Shirley backgrounds subtracted. None of the spectra were normalized in any way. Since the area of a peak is proportional to the amount of material within the probe depth of the surface, weighted by the probability of escape from a given depth, it is assumed that peak areas of similar samples can be compared to give an idea of the relative amounts of a species. This assumption is supported by Figure 2.7.1, which shows the unprocessed XPS spectra of two different samples of the same positive electrode (NMC442, charged in cell to 4.4 V, then stored in a pouch bag for 500 hours at 60°C, with 1M $LiPF_6$ in 3:7 EC:EMC electrolyte, described in further detail in Section 3.2). The two samples were analyzed in the exact same way, but on different days. Figure 2.7.1a

shows that spectra are very similar. Figure 2.7.1b shows that quantification of the elements in the SEI of these samples is the same, within error.

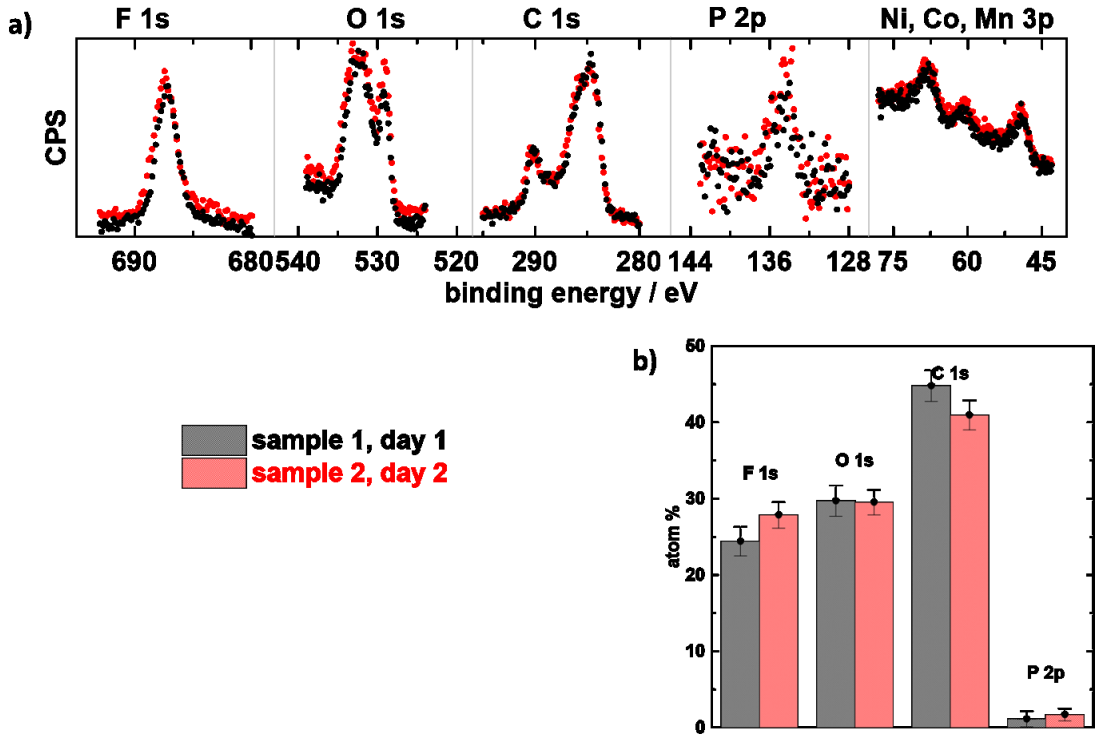

Figure 2.7.1: a) XPS spectra of two identical samples scanned on different days, b) quantification of the elements on the surface of these electrodes.

Quantification of the elements observed with XPS is done using empirically derived relative sensitivity factors (RSF). The RSF used in this work are specific to the SPECS instrument used. The uncertainty in the quantification was calculated with the CasaXPS software (v. 2.3.18).

Peak fitting was also done with CasaXPS software (v. 2.3.18), to distinguish the different chemical species present on the surfaces of the electrodes. Peaks for all the possible SEI

species, shown in Table 2.7.1, were added to a region. [60–62]positions and full widths at half maximum (FWHM) of the peaks were fixed. First, the areas of these peaks were fit. If a certain SEI species was less prevalent in the SEI, the area of its peak would diminish. Peaks were deleted from the fit if their areas were negligible. The position constraints on the remaining peaks were removed, and the peaks were fit to the spectra again. Finally, the FWHM constraints of the SEI peaks were relaxed somewhat to allow for peak broadening caused by the inhomogeneity and insulating properties of the SEI.

Table 2.7.1: XPS chemical shifts of SEI species [60–62]

Photoelectron	*Binding energy / eV*	*Species*
F1s	685.0	LiF
	687.0	fluorophosphate
O1s	529.5	NMC lattice oxygen
	531.0	carbonate, hydroxide
	532.0	ether
	533.0	carbonyl
C1s	284.3	lithiated graphite
	284.8	aliphatic carbon
	285.6	ether
	287.0	carbonyl
	287.8	ester
	289.4	oxalate
	290.1	carbonate
	291.8	polymerized VC
P2p	134	phosphate
	137	fluorophosphate

Good quality peak fitting is rather difficult for lithium-ion SEIs, since there are many overlapping peaks from the multitude of SEI components, some of which are not well-

characterized. This is illustrated by Figure 2.7.2, which shows the F1s, O1s and C1s regions of the XPS spectrum of a fresh (uncycled, unwet) commercial NMC electrode. The carbon region of positive electrodes is hard to fit with certainty (because of overlapping peaks) even for this fresh electrode, which has a well-known composition. The difficulty of fitting XPS spectra of a cycled positive electrode with an SEI is much greater. For this reason, this thesis always compares the relative differences between the SEIs of two or more similar samples, so that the relative difference between the SEIs can be assessed.

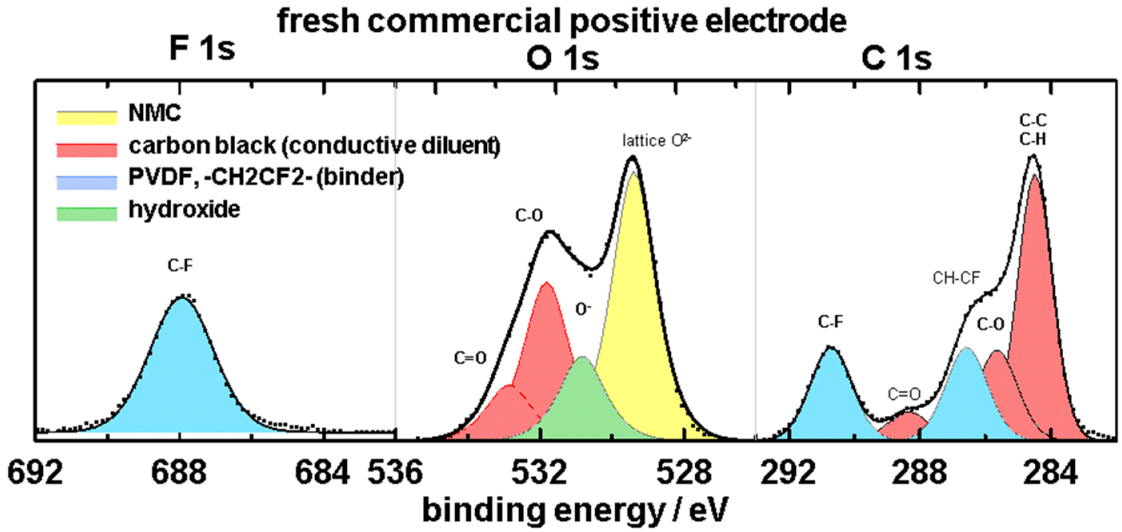

Figure 2.7.2: regions of interest in the XPS spectrum of a fresh commercial positive electrode fit with peaks for the known components.

CHAPTER 3 REVEALING THE HIDDEN CO_2 CHEMICAL DIALOGUE IN LITHIUM-ION CELLS

3.1 DEIJUN'S "POUCH BAG" EXPERIMENTS

Deijun Xiong, a fellow student in the Dahn lab, conducted experiments that set the stage for the work described in this chapter. These experiments are referred to as Deijun's "pouch bag" experiments, and are described in several papers. [42,44,46,47] To expose the chemical dialogue between electrodes, Deijun compared the effects of 60°C storage on charged cells and individual charged electrodes. The individual charged electrodes were stored with electrolyte in the same aluminum laminate material that encased the cells. Storage had no effect on gas evolution and R_{ct} of the charged negative electrode, regardless of whether the electrode was stored in a pouch bag (without the positive electrode) or in the cell (with the positive electrode). The charge-transfer impedances of the negative electrodes were similarly small, and there was little gas evolved in the pouch bags containing the charged negative electrodes. Storage of the charged positive electrode had dramatically different effects when the electrode was stored in a pouch bag (without the negative electrode) or in a cell (with the negative electrode). When stored in a pouch bag, the positive electrode charge-transfer impedance was nearly four times that of one stored in a cell. Also, a tremendous volume of CO_2 (>2 mL) was evolved in the pouch bag containing the charged positive electrode, but not in the charged cell. Tremendous impedance growth and CO_2 evolution were not abated even when the most effective electrolyte additives[42,44] and electrode coatings[47] known in the Dahn group were used.

Deijun's pouch bag experiment gave evidence of cross-talk in lithium-ion cells. The growing volume of CO_2 in the pouch bags containing positive electrodes indicates that electrolyte is continually being oxidized at the charged positive electrode, even when good electrolyte additives and coatings are used. However, this tremendous volume change is not observed when charged positive electrodes are in the presence of a charged negative electrode, in cells. This result suggests that CO_2 is removed from cells by the negative electrodes.

In this chapter, the effects of chemical dialogue on the SEI of the positive and negative electrodes are revealed by XPS. Then the fate of CO_2 inside lithium-ion cells is determined. The mechanism of CO_2 consumption is revealed by XPS, and the possible consequences of CO_2 consumption on cell performance are discussed.

3.2 Effect of Chemical Dialogue on the Positive Electrode SEI

Deijun Xiong prepared the electrode samples discussed in this section.

To try to understand the cause of their large impedance, XPS analysis was done on charged positive electrodes that were stored in pouch bags.At first it was thought that their impedance was caused by the deposition of oxidized electrolyte species that would otherwise would have migrated to the negative electrode. The NMC442 electrodes discussed in this section were from cells containing 1M $LiPF_6$ in 3:7 wt. EC:EMC electrolyte (no additives), were charged to 4.4 V. These electrodes were stored in a cell or

in a pouch bag with electrolyte (again 1M $LiPF_6$ in 3:7 wt. EC:EMC) for 500 hours at 60°C.

Contrary to expectations, the SEI on the positive electrode stored in the pouch bag was thinner than that on the positive electrode from the stored cell. The relative thicknesses of the SEIs is most easily seen by comparing the area of the peak from NMC lattice oxygen, at 529 eV, in the O1s spectra shown in Figure 3.2.1. Since the inelastic mean free path (IMFP) of an O1s photoelectron in the SEI is small (~2.4 nm, assuming the SEI has a density of ~1 g/cm^3) [63,64], the intensity of the underlying NMC peak will diminish as the overlying SEI thickens. Figure 3.2.1 shows that the NMC O1s peak of the electrode that was stored in the cell is smaller than that of the electrode stored in the bag, indicating that the SEI is thicker on the electrode stored in the cell. The PVDF binder peak, at 291 eV, in the C1s region is also less intense for the electrode that was stored in the cell, indicating that the binder, as well as the active particles, are covered in a thicker SEI when stored in a cell.

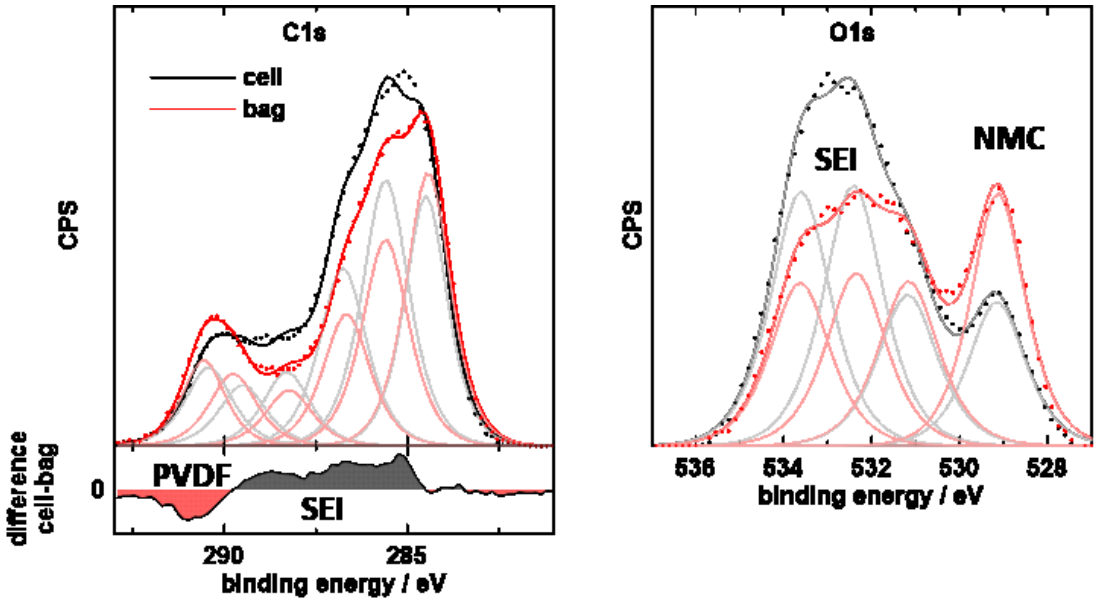

Figure 3.2.1: C1s and O1s spectra of positive electrodes that were charged to 4.4 V in cells, then stored for 500 hours at 60°C in cells or in pouch bags containing 1M $LiPF_6$ in 3:7 wt. EC:EMC. Curve-fitting in these spectra is intended only as a guide for the eye, since the peaks are too closely spaced for good peak fitting.

The species that cause thickening of the SEI in the pouch cell are carbon and oxygen-rich, evidenced by the increased intensity in the region of 285-290 eV (aliphatic, ether, carbonyl and ester-type species), and 532-534 eV (carbonyl and ester-type species). The amount of inorganic SEI species (phosphates and fluorophosphates) was similar for both electrodes. Virtually identical results were obtained when this experiment was repeated with electrodes that were stored in pouch bags or cells with different electrolyte solvents and electrolyte additives (1:1 wt. fluoroethylene carbonate:bis(2,2,2-fluoroethyl) carbonate, 2% VC and 2% PES).[42,44]

These results show that the large impedance of charged positive electrodes stored in pouch bags cannot be attributed to a thickened SEI. This result is consistent with the

work of others who have shown (using an electrochemical quartz microbalance) that electrochemical electrolyte oxidation does not produce solid reaction products that attach to the positive electrode, and therefore does not directly cause film growth.[37] The fact that the SEI is thicker on the positive electrode that was stored in the cell suggests that SEI growth on the positive electrode is caused by the deposition of species generated from the negative electrode.

3.3 Effect of Chemical Dialogue on the Negative Electrode SEI

Deijun Xiong prepared the electrode samples discussed in this section.

XPS analysis was done on charged negative electrodes stored either in pouch bags or pouch cells, to see what effect cross-talk from the positive electrode had on the SEI of the negative electrode. Figure 3.3.1 shows the XPS spectra of negative electrodes stored in pouch bags or pouch cells with electrolyte containing a) 2% VC, or b) electrolyte without additives. Cross-talk from the positive electrode evidently thickens the SEI of the negative electrode in 2% VC electrolyte, as the peak from lithiated graphite (~283 eV) is visible only for the electrode stored in the bag. The lithiated graphite peak is not present in the spectrum of the electrode stored in the cell, indicating that the overlaying SEI has become much thicker than the photoelectron IMFP. The species that thicken the SEI on the electrode from the cell with 2% VC are phosphates (134 eV), fluorophosphates (687 and 137 eV), LiF (685 eV) and oxalates or carbonates (289-290 eV). Mn ions originating from the positive electrode may also form part of the SEI for the electrode stored in the

cell, since there is slightly more intensity around ~47 eV, which corresponds to Mn 3p photoelectrons. It has been observed several times that Mn from the positive electrode migrates and deposits on the negative electrode. [65–67]

The lithiated graphite peak is not visible in the spectra of the electrodes stored in electrolyte without additives, shown in Figure 3.3.1b. This indicates that the SEIs on both of these electrodes are relatively thick. It is not possible to tell with this data whether one SEI is thicker than the other. It is likely that cross-talk thickened the SEI of the electrode in the cell, just as it did with the electrodes that were stored in electrolyte with 2% VC. LiF is slightly more abundant (~5 atom % more F at 685 eV) in the SEI of the electrode stored in the cell, while phosphates are slightly more abundant in the SEI of the electrode stored in the bag (~ 0.7 atom % more P at 134 eV). A great deal of non-cross-talk parasitic reactions are known to occur directly between charged negative electrodes and electrolyte without additives[68] so it may be that SEI species from cross-talk are outnumbered and buried by SEI species that occur from the direct reaction of additive-free electrolyte with the charged negative electrode.

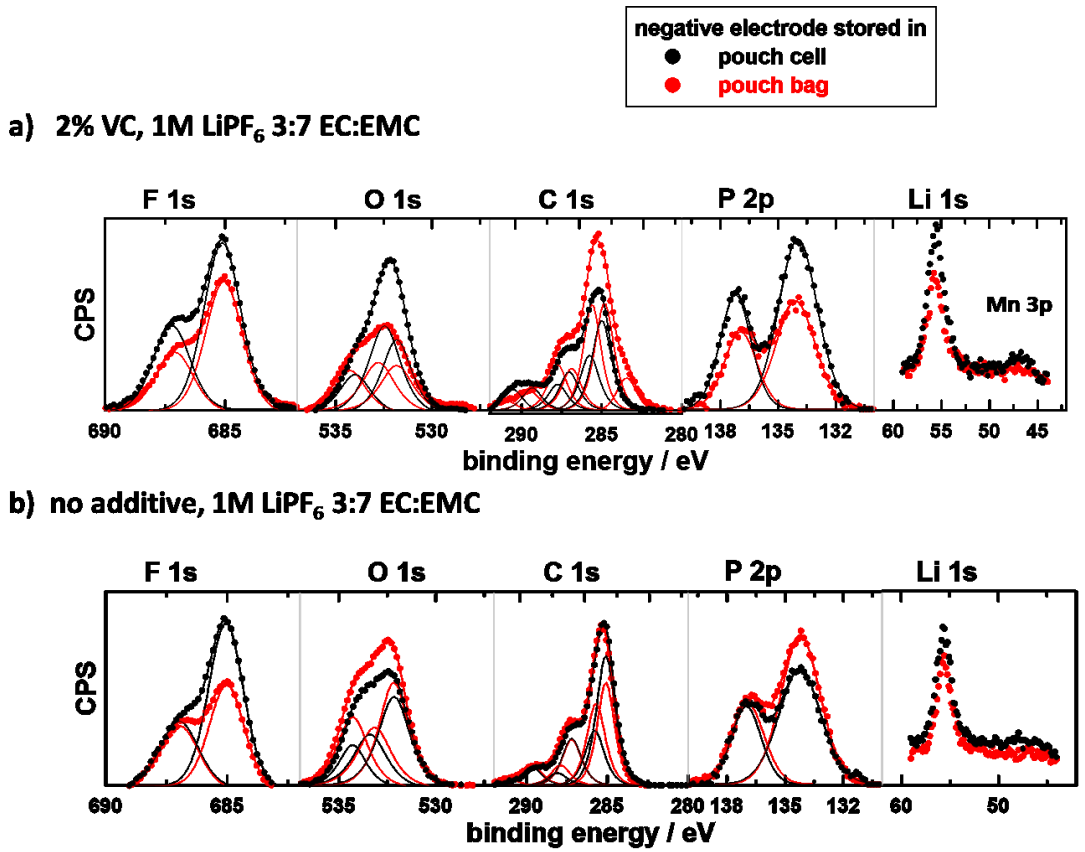

Figure 3.3.1: XPS spectra of charged negative electrodes stored in pouch bags or pouch cells with a) electrolyte containing 2% VC, and b) electrolyte without additives.

3.4 Fate of CO_2 in a Lithium-Ion Cell

To explain why a tremendous amount of gas evolution was observed when charged positive electrodes were stored in pouch bags, but not when charged positive electrodes were stored in pouch cells, it was hypothesized that CO_2 is consumed by the negative electrode in cells. It was also thought that perhaps the evolved CO_2 reacted with the positive electrode to cause impedance growth (for example, if it reacted with oxygen radicals released from the charged positive electrode's lattice, which some believe

contributes to dramatic impedance growth).[25,69] To test these hypotheses, a modification was made to Deijun's pouch bag experiment to probe the reactivity of CO_2 with individual charged electrodes. A rubber septum was glued to the pouch bag, so that the pouch bag could be inflated with gas using a syringe. The method for constructing these "inflated pouch bags" is described fully in Section 2.2. Charged negative electrodes were stored in CO_2-inflated pouch bags with 0.5 mL of electrolyte (1M $LiPF_6$ in EC:EMC), to better simulate the environment of a pouch cell. Positive electrodes wererinsed and dried to remove all electrolyte before being stored in CO_2-inflated pouch bags, so that gas evolution and impedance growth from electrolyte oxidation would not occur.

Figure 3.4.1a shows volume vs. time for pouch bags containing charged electrodes, inflated with CO_2 and stored at 40°C. The volumes of the pouch bags containing lithiated graphite negative electrodes decreased over time, whereas the volumes of the pouch bags containing charged positive electrodes did not change much after equilibration at 40°C. The decrease in volume of the pouch bags containing charged negative electrodes is not due to the dissolution of CO_2 in electrolyte, although the solubility of CO_2 in organic carbonates is very high (2.9 mL CO_2/mL electrolyte, at standard temperature and pressure).[70] CO_2-inflated pouch bags containing only electrolyte (no charged negative electrode) did not decrease in volume during storage (Figure 3.4.1b). Evidently the dissolution of CO_2 in the electrolyte is fast and occurs before the data for Figure 3.4.1 was collected, which was approximately one hour after the injection of CO_2 into the pouch bags. CO_2-inflated pouch bags containing only dry charged negative electrodes decreased in volume decreased at a similar rate to those that contained charged negative

electrodes and electrolyte. The amount of charge required to reduce the volume of CO_2 consumed in Figure 3.4.1B is ~0.5 mAh, assuming a one-electron reduction, much smaller than the 200 mAh capacity of the charged negative electrode.

To see if the reaction of CO_2 increased the impedance of the electrodes, EIS was done on symmetric cells made from electrodes taken from the CO_2-inflated pouch bags after storage. No change in R_{ct} was observed after storage for charged negative electrodes or charged positive electrodes. This result shows that the reaction of CO_2 at the positive electrode does not contribute to impedance growth in this case. This also proves that the SEI formed by CO_2 reduction at the negative electrode does not impede the transfer of lithium ions.

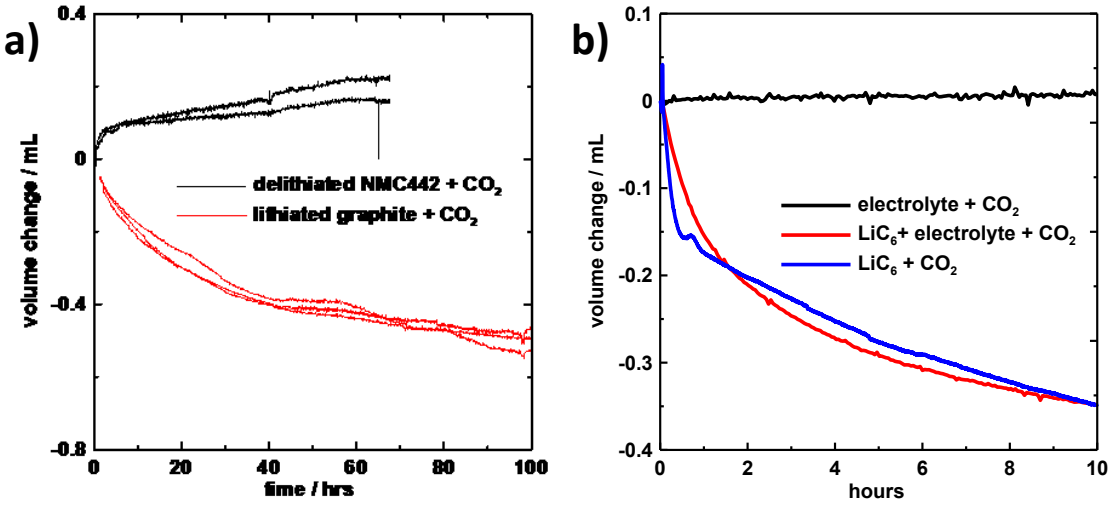

Figure 3.4.1 volume change vs. time for pouch bags containing charged negative or positive electrodes inflated with CO_2 and stored at 40°C. Reproduced with permission from *J. Electrochem Soc.*, **164**, A3518 (2017). Copyright 2017, The Electrochemical Society.

3.5 PRODUCTS FORMED BY CO_2 REDUCTION IN CELLS

After it was determined that large volumes of CO_2 react at the negative electrode, the mechanism and by-products of this reaction were investigated. Electrodes stored with CO_2 were removed from the pouch bags and subjected to XPS analysis. Figure 3.5.1 compares the XPS spectra of charged negative electrodes that were stored in vacuum-sealed pouch bags to those that were stored in CO_2-inflated pouch bags. The XPS spectrum of the negative electrode stored with electrolyte and CO_2 has more intensity in the region corresponding to oxalate-type species, ~289 eV. This suggests that CO_2 is reduced to form lithium oxalate, according to equation (8)

$$2\ CO_2 + 2\ Li \rightarrow Li_2C_2O_4 \qquad (8)$$

The P2p region of the XPS spectrum of the negative electrode stored in CO_2 has more intensity in the region corresponding to phosphate species, ~134 eV. This suggests that CO_2 is reduced to form CO and Li_2CO_3, which subsequently reacts to with $LiPF_6$ to re-evolve CO_2, according to equations (9) and (10)

$$2\ CO_2 + 2\ Li \rightarrow Li_2CO_3 + CO \qquad (9)$$

$$2\ Li_2CO_3 + LiPF_6 \rightarrow 4\ LiF + LiPO_2F_2 + 2\ CO_2. \qquad (10)$$

Recent evidence for equation (10) shows that that it occurs with a 50% yield after two days at 55°C, in organic carbonate solutions.[71] Equation (10) would have a negative impact on cell performance, since it suggests that the reduction of CO_2 to lithium carbonate results in the re-evolution of CO_2, and the consumption of salt in the electrolyte.

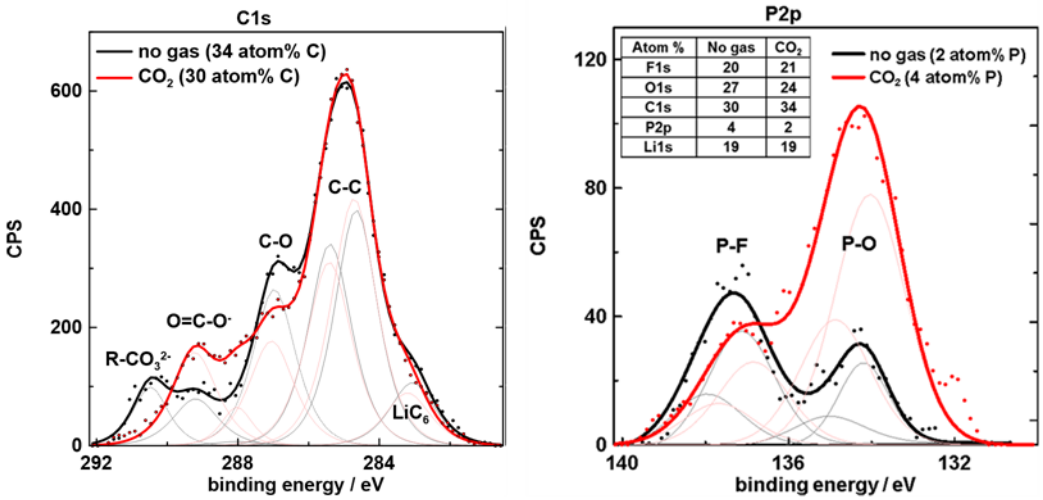

Figure 3.5.1: C1s and P2p regions of XPS spectra of charged negative electrodes that were stored in pouch bags with and without CO_2. Reproduced with permission from *J. Electrochem Soc.*, **164**, A3518 (2017). Copyright 2017, The Electrochemical Society.

3.6 Possible Effects of CO_2 Reduction in Cells

Although the reaction mechanism of CO_2 in lithium-ion cells was never explicitly investigated before, as it has been here, the effect of CO_2 on the performance of lithium-ion cells has been debated for many years. In the early days of lithium-ion batteries, CO_2 was used as an electrolyte additive. Bubbling CO_2 through the electrolyte of a beaker-type half-cells resulted in a lithium-rich SEI that effectively passivated graphite electrodes. [72,73]However, the experimental conditions in these studies may have masked the adverse consequences of CO_2. Beaker-type cells have a large excess of electrolyte, so depletion of $LiPF_6$ (from equation (10)) would not have been observed. Also, lithium/graphite half-cells do not probe the reactions at higher potentials. Later, it was argued that CO_2 was detrimental to cells because lithium oxalate, its reduction product, is slightly soluble in electrolyte and can be oxidized at the positive electrode to reform

CO_2—a shuttle-type parasitic reaction that would result in self-dishcarge.[74] This shuttle reaction may occur to some small extent, but it is not detrimental to cells operated to typical voltages. Unpublished work by Nupur Sinha in the Dahn lab showed that intentionally saturating the electrolyte with lithium oxalate did not increase the rate of self-discharge at high voltage. Very recently, it was shown that CO_2 consumption hinders capacity fade in cells with silicon alloy negative electrodes. [75] The benefit of CO_2 was attributed to its ability to scavenge lithium alkoxides from the electrolyte (alkoxides would otherwise be oxidized at the positive electrode and cause charge endpoint capacity-slippage). [76] Also, very new reports have emerged that $LiPO_2F_2$ (produced from the reduction of CO_2, via equations (9) and (10)) is a powerful electrolyte additive. Even though $LiPO_2F_2$ is slightly soluble, electrolytes containing $LiPO_2F_2$ significantly reduce capacity fade, for reasons yet unknown. [77–79] It could be that the consumption of CO_2 benefits lithium-ion cells by the production of $LiPO_2F_2$.

3.7 Conclusions

Deijun's pouch bag experiments gave clear proof that chemical dialogue occurs in cells. Without the presence of the negative electrode, it is obvious that a tremendous amount of gas (CO_2) is evolved from the oxidation of electrolyte at the charged positive electrode, but in the presence of the charged negative electrode this gas is not observed. Also, isolated storage of charged positive electrodes causes dramatic charge-transfer impedance growth. This is not caused by the formation of thick, resistive films of oxidized electrolyte on the positive electrode. XPS analysis showed that the SEIs on positive

electrodes stored in pouch bags are thinner than those stored in cells, which suggests that chemical dialogue causes thickening of the positive electrode SEI. The reason why large volumes of CO_2 are observed in pouch bags containing electrolyte and charged positive electrodes, but not in full cells, was discovered by the work done in this chapter. Using the inflated pouch bag method, it was shown that CO_2 is readily reduced at the negative electrode. Using XPS, the reduction mechanisms for CO_2 were inferred. The effects of CO_2 consumption at the negative electrode were discussed. There is evidence that CO_2 can be beneficial to cells, as it forms a lithium-rich, passivating SEI on the negative electrode. Reduction of CO_2 may also indirectly cause the formation of $LiPO_2F_2$, a beneficial electrolyte additive. On the other hand, the reduction of CO_2 removes active lithium from the negative electrode, may cause depletion of electrolyte salt (by the reaction of Li_2CO_3 with $LiPF_6$), and may contribute to self discharge at very high voltages (by the CO_2/oxalate shuttle reaction).

CHAPTER 4 FATE OF OTHER GASES IN LITHIUM-ION CELLS

J.P. Allen, an undergraduate student, assisted with the experiments described in this chapter. Figures and text in this chapter are reproduced with permission from *J. Electrochem Soc.*, **164**, A3518 (2017).

After the fate of CO_2 was determined using the inflated pouch bag method, the fates of other gases in lithium-ion cells were investigated in the same way. Gases evolve from lithium-ion cells during their formation cycle, when electrolyte reacts at the surfaces of the charging electrodes to form the initial SEIs. Gases can also form during cycling or storage. Gases are always removed from soft-cased pouch cells in a degassing step after formation, to maintain their shape and to ensure uniform pressure on the electrodes. Hard-cased cells, such as 18650s, are often not degassed since they are sealed with a weld that can withstand large pressures. If cells are not degassed after formation, the gases are partially consumed by the cell over time.[50] The identity of the gases consumed, the mechanisms by which gas consumption occurs, and the effect of gas consumption on cell performance have not been investigated until now. It has been speculated, informally, that the consumption of gas influences cell performance, especially since some pouch cells and 18650 cells with identical cell chemistries perform differently. In this chapter the gases evolved and consumed are identified by GC-TCD. Their reaction mechanisms are inferred using the inflated pouch bag method, and the possible effects of gas consumption on cell performance are discussed.

4.1 Gas Evolution During Cell Formation

Gas evolution during formation occurs in two distinct steps: the first at low voltage, the second at high voltage. These reactions can be seen in Figure 4.1.1, for the formation of a cell with graphite/NMC442 electrodes, with 1 M $LiPF_6$ in EC:EMC 3:7 wt. ratio electrolyte. The first gas-evolving event is caused by reduction of electrolyte and electrolyte impurities at the negative electrode. The major gaseous reduction products of EC are C_2H_4 and CO, by equations (11) [29] and (12) [80]

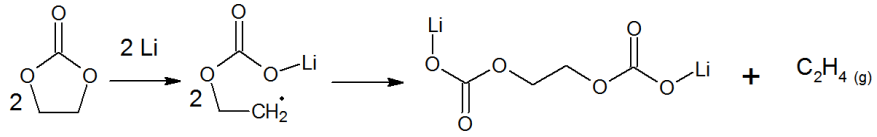

(11)

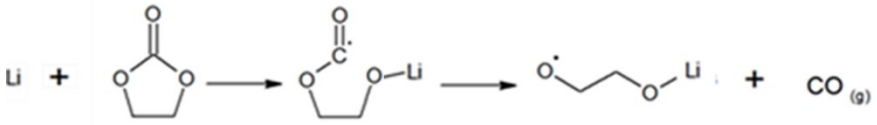

(12)

The reduction of water and other protic impurities cause the evolution of hydrogen by equation (13):

$$2\ H_2O + 2e^- \rightarrow H_2 + 2\ OH^- \qquad (13)$$

The reduction of EMC, and other linear alkyl carbonates, causes the evolution of CH_4 and C_2H_6, but these products form in small quantities since the negative electrode is mostly passivated by the sacrificial reduction of EC by the time EMC reduces. The second gas-evolving event, is the oxidation of electrolyte at the charged positive electrode, occurs above 4.2 V for the cell in Figure 4.1.1. The most likely oxidation pathway of EC gives CO_2 and a radical carbocation by equation (14). [81,82]

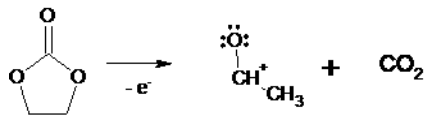

(14)

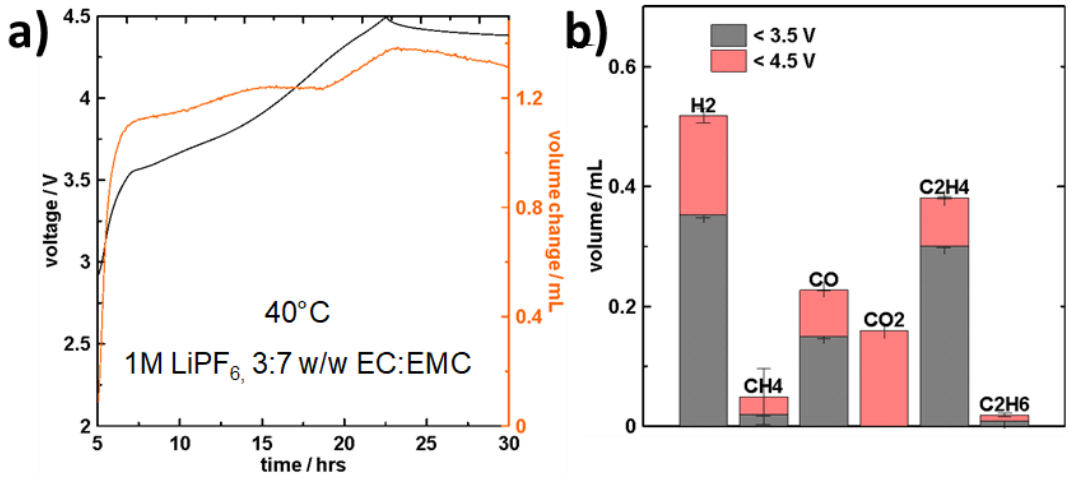

Figure 4.1.1: a) voltage and volume vs. time of a cell (NMC442/graphite) undergoing its formation cycle, and b) volumes of the gases evolved from the cell during formation, determined by GC-TCD.

4.2 Gas Consumption After Cell Formation

Figure 4.2.1a shows the consumption of gas after formation when cells (with NMC442 positive electrodes, and 1 M $LiPF_6$ in 3:7 wt. EC:EMC electrolyte) were stored at 40°C, at voltages ranging from 2.8 V (fully discharged) to 4.5 V (fully charged). The fully charged cell consumed half the formation gas within the first 100 hours of storage. Less gas was consumed at lower states of charge. Figure 4.2.1b shows the volumes of the gases present in the cell before storage, and after 100-hour intervals of storage at 4.5 V. The volume of CO_2 decreases the most rapidly. Nearly all the CO_2 is consumed within the first 100 hours of storage. The volumes of H_2 and C_2H_4 also diminish significantly. A

small volume of CO is consumed in the first 100 hours of storage. The volumes of CH_4 and C_2H_6 do not decrease over time. These saturated hydrocarbons likely owe their inertness to their low bond polarity and the low oxidation state of carbon.

It must be determined whether the decrease in gas volume during storage could be due to other factors, besides consumption at the charged electrodes. Gas dissolution in electrolyte, and gas diffusion through the aluminum laminate pouch bag material would also result in decreased cell volumes. Gas consumption is rapid at high states of charge, and slows with lowered states of charge, which suggests that the observed gas consumption is not due to dissolution or leaking. Also, GC-TCD shows that the gases are consumed at different rates, with some gases, such as CH_4, not being consumed at all.

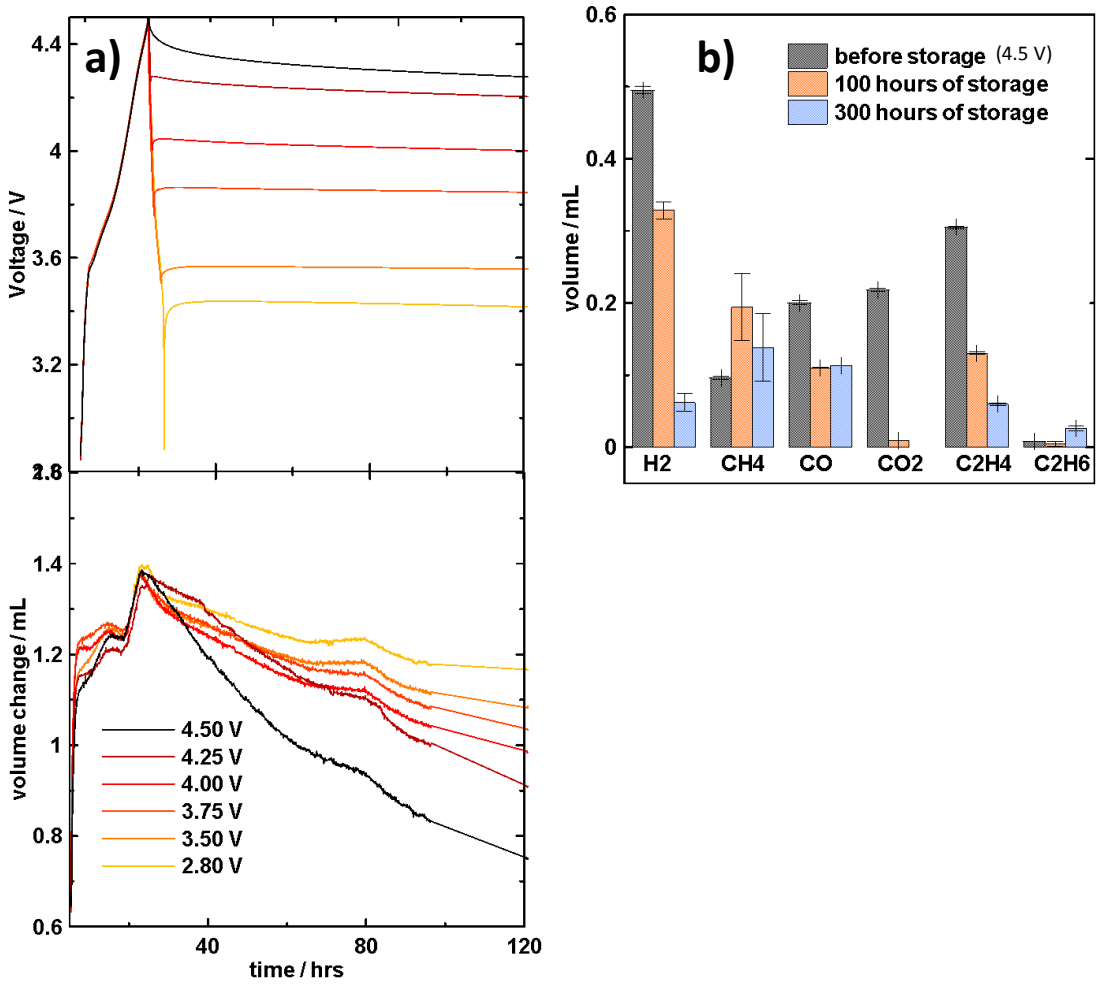

Figure 4.2.1: a) voltage and volume vs. time of cells (NMC442/graphite, 1 M $LiPF_6$ 3:7 EC:EMC) undergoing their first charge, then stored open-circuit at various states of charge at 40°C; b) volumes of the gases present in the cell, measured at various intervals during 4.5 V storage, using GC-TCD.

4.2.1 Fate of H_2 in Lithium-Ion Cells

Using the inflated pouch bag method, the reactivity of hydrogen with charged electrodes was investigated. The electrodes were charged in cells to voltages of 4.4 or 4.6 V before being stored in H_2-inflated pouch bags. Figure 4.2.2 shows their volume change after one week of storage at 40 or 60°C. The length of the error bars in Figure 4.2.2 indicate the

difference between duplicate samples. The volume decreased for the pouch bags containing both negative or positive electrodes, indicating that H_2 can react at both electrodes. The reduction of H_2 likely happens by equation (15), and the electrochemical oxidation of H_2 likely happens by equation (16)

$$2\ Li + H_2 \rightarrow 2\ LiH \qquad (15)$$

$$H_2 \rightarrow 2\ H^+ + 2\ e^- \qquad (16)$$

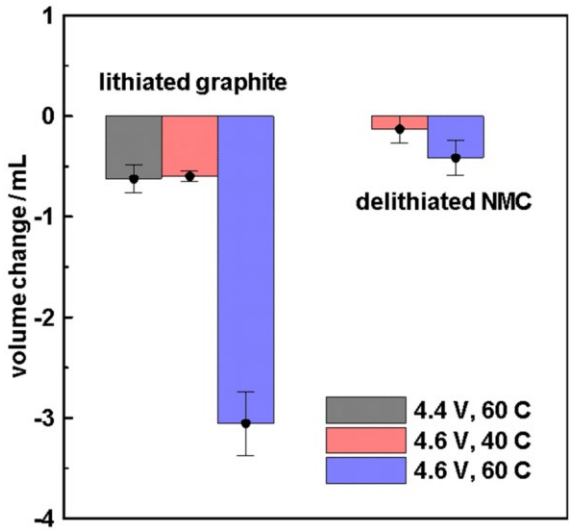

Figure 4.2.2: volume changes of H_2-inflated pouch bags containing positive or negative electrodes at different states of charge, stored for one week at 40 or 60°C.

It has been observed that H_2 ceases to evolve from the negative electrode if it is isolated from the positive electrode.[42,83] The consumption of H_2 and the formation of protons at the positive electrode suggests the possibility of an H_2/H^+ shuttle. Like the oxalate/CO_2 shuttle described before, the H_2/H^+ shuttle could be a cause of continuous self-discharge. Protic species (water impurities, or species generated from electrolyte oxidation) are

reduced at the negative electrode to form H_2, which diffuses to the positive electrode and oxidizes to re-form protons, which migrate back to the negative electrode, to complete the cycle. In terms of cell performance, the H_2/H^+ shuttle would manifest as reversible self-discharge during storage and charge endpoint capacity slippage during cycling. However, if there is no H_2/H^+ shuttle does occur, it would compete with the reduction of H_2 at the negative electrode. Figure 4.2.2 shows that the volume of H_2 consumed at the negative electrode is three times larger than the volume consumed at the positive electrode at a given temperature and SOC. This indicates that H_2 is more likely to reduce than to oxidize in a lithium-ion cell, and thus the H_2/H^+ shuttle, if it does occur, is not the dominant reaction for H_2.

It is not clear why a negative electrode charged to 4.6 V in a cell consumes more gas than the negative electrode charged to 4.4 V in a cell, since the potential of the graphite negative electrode at these two cell voltages is the same (~ 0.075 V vs. Li/Li^+). Because the potential of the graphite is the same, the rate of gas reduction should be the same. It is possible that the increased consumption of gas at the negative electrode at higher state of charge has something to do with the catalytic effect of Mn ions in the negative electrode SEI, which are more prevalent when cells are exposed to higher states of charge.[65] In any case, the results in Figure 4.2.2 agree with the results shown in Figure 4.2.1a, which shows that full cells consume more gas after formation when stored at higher states of charge.

4.2.2 Fate of C_2H_4 in Lithium-Ion Cells

Next, the reactivity of C_2H_4 with charged electrodes was investigated using the inflated pouch bag method. Figure 4.2.3a shows the volume change of the C_2H_4-inflated pouch bags containing charged negative electrodes after one week of storage at 40 or 60°C. The volume decreased only for the pouch bag containing charged negative electrodes. About eight times more C_2H_4 is consumed at 60°C than at 40°C for electrodes at the same SOC, which indicates that the rate of this reaction is slower at lower temperatures. Like with H_2, the amount of gas consumed by the negative electrode charged to 4.6 V in a cell is greater than the amount consumed by the negative electrode charged to 4.4 V in a cell. The reason for this is hard to explain, as discussed in the previous section. The consumption of C_2H_4 is likely due to the reduction of C_2H_4 by lithium, to form $Li(C_2H_4)_n$ (n= 1,2,3) or $Li_2C_2H_4$ type species, which are known to exist.[84] Polyolefins are known to be prominent components of the negative electrode SEI.[85]

Some amount of C_2H_4 evidently reacts with the charged positive electrodes, although the volume of pouch bags containing charged positive electrodes did not decrease. Figure 4.2.3b shows R_{ct}, measured in symmetric cells, of charged positive electrodes after storage in vacuum-sealed pouch bags and C_2H_4-inflated pouch bags. R_{ct} of electrodes stored in C_2H_4 are roughly double those stored in vacuum, for a given temperature and SOC. This result suggests that C_2H_4 can be oxidized at the surface of charged positive electrodes, resulting in a thicker positive electrode SEI, which causes increased R_{ct}. This

reaction may not play a significant role in full cells, however, as C_2H_4 is consumed in larger quantities at the negative electrode.

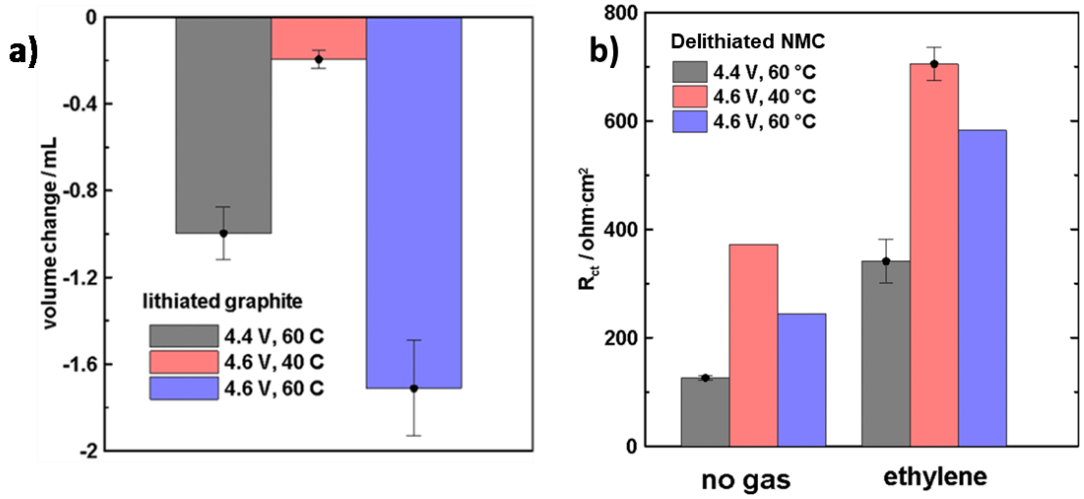

Figure 4.2.3: a) volume change of C_2H_4-inflated pouch bags containing negative electrodes charged in cells to 4.4 or 4.6 V, stored for one week at 40 or 60°C; b) R_{ct} of charged, rinsed and dried positive electrodes charged in cells to 4.4 or 4.6 V, after storage in vacuum or C_2H_4 for one week at 40 or 60°C.

4.2.3 Fate of CO in Lithium-Ion Cells

Lastly, the reactivity of CO with charged electrodes was investigated using the inflated pouch bag method. Table 4.2.1 shows the volume change of the CO-inflated pouch bags containing negative electrodes after one week of storage at 40 or 60°C. The pouch bags containing charged positive electrodes did not decrease in volume. The same amount of CO was consumed in pouch bags with negative electrodes stored at 40 and 60°C—only ~0.15 mL. Figure 4.2.1b (showing the gases in a full cell over time, measured by GC-TCD) also shows that only ~0.1 mL of CO was consumed in full cells over 300 hours. Evidently, only this small and finite amount of CO can be consumed by the negative

electrode. The reduction products of CO and H_2 could include CH_4, C_2H_4 and other small hydrocarbons. These products form in varying degrees from the reduction of CO in aqueous solutions, depending on the pH and catalytic properties of the electrode.[86–89]

Table 4.2.1: volume change of CO-inflated pouch bags containing positive or negative electrodes that were charged in cells to 4.4 or 4.6 V, stored for one week at 40 or 60°C.

SOC, temperature	Volume change
4.6 V, 40°C	-0.14 ± 0.09 mL
4.6 V, 60°C	-0.14 ± 0.05 mL

4.3 CONCLUSIONS

In this chapter, the evolution of gases during formation and their subsequent consumption were studied by GC-TCD, Archimedes' volume measurements, and the inflated pouch bag method. In the absence of electrolyte additives, six gases are evolved from the reaction of organic carbonates with the charging electrodes: H_2, C_2H_4, CO_2, CO, CH_4 and C_2H_6. Of these gases, all except the saturated hydrocarbons are subsequently consumed. H_2 is consumed by both the negative and positive electrode. CO_2, CO and C_2H_4 are consumed at the negative electrode, although C_2H_4 also reacts at the positive electrode, evidenced by an increased R_{ct}.

Table 4.3.1: summary of this chapter, showing the gases evolved in cells (NMC442/graphite cells with 1 M $LiPF_6$ in 3:7 EC:EMC), at which electrode they are thought to be produced, at which electrode they were shown to be consumed, and the possible reaction products they form at these electrodes.

Gas	***Produced by (electrode)***	***Consumed by (electrode)***	***Possible reaction product(s)***
CO_2	Negative Positive	Negative	$Li_2C_2O_4$, Li_2CO_3 [71,74]
H_2	Negative	Negative Positive	LiH, CH_4 H^+ [37,71]
C_2H_4	Negative	Negative Positive	$Li(C_2H_4)_n$ [84] (R_{ct} growth)
CO	Negative	Negative	CH_4, C_2H_4 [74–77]
saturated hydrocarbons	Negative	-	-

CHAPTER 5 EFFECT OF GAS CONSUMPTION ON CELL PERFORMANCE

Now that gas consumption is better understood, the question remains: what effect, if any, does the consumption of gas after formation have on cell performance? The following sections aim to answer these questions by investigating the effect of consumed formation gas on self-discharge, capacity fade, and charge-transfer impedance.

5.1 Effect of Gas Consumption on Self-Discharge

It has been suggested that CO_2 and H_2 may initiate shuttle reactions that cause reversible self-discharge. To see if the presence of formation gas caused self-discharge in undegassed cells (NMC442/graphite electrodes, 1M $LiPF_6$ in 3:7 EC:EMC electrolyte), the open-circuit voltage of a cell that was degassed after formation to 4.5 V was compared to that of an identical cell that was not degassed. Figure 5.1.1 shows that the rate of self-discharge for the non-degassed cell is virtually the same as the cell that was degassed prior to storage. This result indicates that the shuttle reactions initiated by CO_2 or H_2 likely do not contribute to self discharge up to 4.5 V. This may be because these gases are readily reduced at the negative electrode at this state of charge, and the oxidation of H_2 at the positive electrode was shown to be much slower than the reduction of H_2 at the negative electrode.

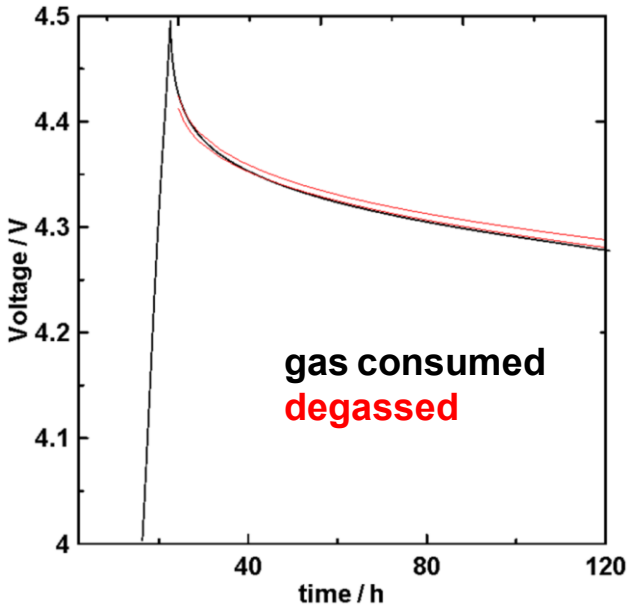

Figure 5.1.1: voltage vs. time for identical cells that were charged for the first time to 4.5 V and stored open-circuit for 100 hours at 40°C. The cells in red were degassed before storage. The cell in black was not degassed.

5.2 Effect of Gas Consumption on Capacity Fade

Most of the gas evolved during formation is reduced at the negative electrode. After 500 hours of storage at 40°C, 1 mL gas is consumed in the cells studied here (NMC442/graphite electrodes, 1M $LiPF_6$ in 3:7 EC:EMC electrolyte, charged to 4.5 V). Since reduction of species other than active lithium ions results in a loss of active lithium, the consumption of gas at the negative electrode results in lost cell capacity. The amount of capacity needed to reduce 1 mL of gas, at standard temperature and pressure, is calculated to be 1.1 mAh (using the ideal gas law and Faraday's constant). Considering that ~3 mL of CO_2 dissolves in the electrolyte within the cell at room temperature and pressure,[70] the total amount of gas consumed in the cells studied here (which contained ~1 mL of electrolyte) may be as high as 4 mL. This means that up to ~4 mAh, ~2% of the

cell capacity may be lost because of gas consumption in the cells studied here. This amount of capacity loss is too small to measure easily, even with an ultra high precision charger, because of cell-to-cell variation in the pouch cells used for this work, shown in Figure 5.2.1.

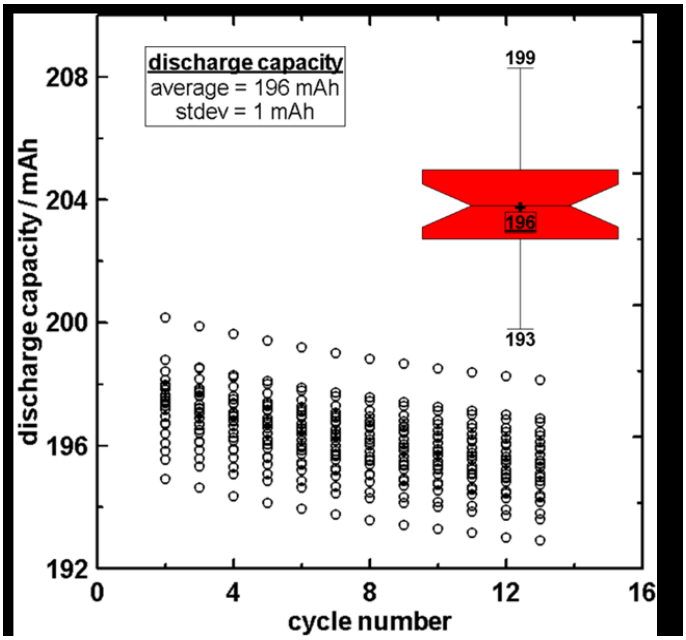

Figure 5.2.1: discharge capacities of 26 indentical cells, measured on ultra high precision charging systems, and a box-and-whisker plot of the discharge capacities at the 12th cycle. W.J. Stone prepared the cells shown in this figure. This figure is reproduced with permission from *J. Electrochem Soc.*, **164**, A3518 (2017). Copyright 2017, The Electrochemical Society.

5.3 Effect of Gas Consumption on R_{CT}

To see if gas consumption affected the charge-transfer impedance of cells, EIS was done on cells that were either degassed or not degassed after formation, then stored at 4.5 V for 500 hours at 40°C. Figure 5.1.1 shows that there is no significant difference between the

charge-transfer resistances of these cells. Evidently consumption of formation gas does not lead to increased charge-transfer resistance, even though storage in C_2H_4 was observed to increase the charge-transfer resistance of dried, charged positive electrodes in section 4.2.2.

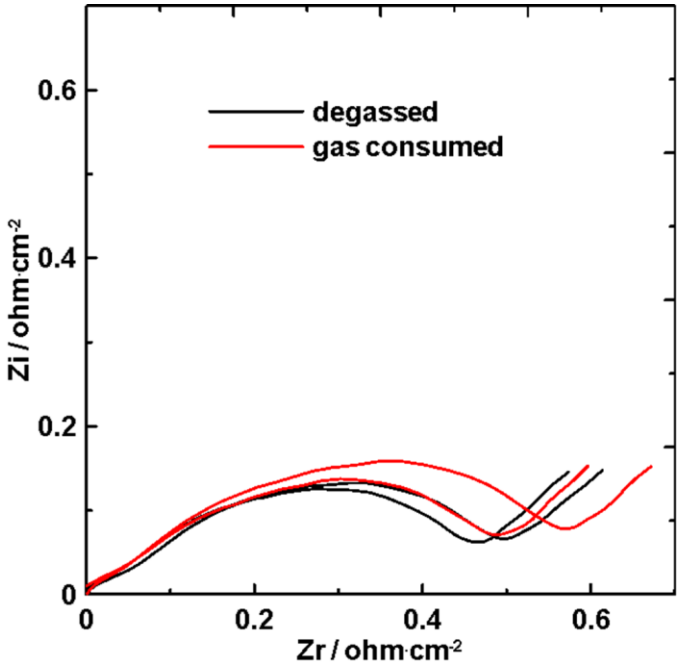

Figure 5.3.1: Nyquist plot of cells that were charged once to 4.5 V, and optionally degassed before 500 hours of open-circuit storage at 40°C. This figure is reproduced with permission from *J. Electrochem Soc.*, **164**, A3518 (2017). Copyright 2017, The Electrochemical Society.

5.4 Concluding Remarks

The consumption of formation gas does not have any measurable effects on the subsequent performance of the cells studied here. These cells did not contain electrolyte additives, which would have reduced the amount of gas evolved during formation, so that

the effects of gas consumption, if any, would be more obvious. A commercial cell would contain electrolyte additives and would evolve (and therefore consume) even less gas after formation. Since there were no significant adverse (or beneficial) effects of the consumption of formation gas on the performance of cells without additives, it is unlikely that there would be any effects on cells in which additives that suppress gas during formation are used. However, Dejun's pouch bag experiments (described in Section 3.1) showed that charged positive electrodes stored alone in electrolyte (with or without additives) produced large volumes of CO_2 that would not be observed in the presence of the negative electrode.[42,44,46,47] This suggests that CO_2 evolution and consumption occurs continuously in charged cells, regardless of whether electrolyte additives are used. After a long time is spent in a fully charged state, the adverse effects of CO_2 consumption (capacity and $LiPF_6$ loss) may be more apparent. The continual consumption of CO_2 at the negative electrode may explain why Li_2CO_3, a possible product of CO_2 reduction, is only observed in the SEI on aged graphite electrodes but is not part of the SEI in young cells.[90] Accumulation of Li_2CO_3 at the negative electrode is thought by some to block the pores of the negative electrode, causing failure of aged cells.[91] These observations suggest that the effects of gas consumption accumulate over time, and may lead to the failure of aged cells, although this work shows that the consumption of small amounts of formation gas does not affect the performance of fresh cells.

CHAPTER 6 EFFECT OF FORMATION CONDITIONS ON THE SEI

J.P. Allen, an undergraduate, prepared some of the cells described in this chapter.

A good SEI hinders parasitic reactions between the underlying electrode and the electrolyte. SEI quality is related to both the SEI thickness[53,92,93]and the SEI [13,94,95] The quality of the SEI evidently improves as a cell matures. Over the years, the Dahn lab has cycled thousands of new lithium-ion cells on ultra high precision chargers, used to evaluate cell chemistries and rank them in order of coulombic efficiency[3,51,96–993] In every case, the CE of a fresh cell increases towards the ideal value of 1.0000… during testing but never actually reaches 1.0000… After about 15-20 cycles at C/20 (600-800 hours) and 40^{o}C, the CEs reach relatively stable values where reliable comparisons between cells can be made[54,55,98,100–1026] The SEI layers formed in the first cycle are not completely passivating but become more and more passivating over time. One must wait a sufficient amount of time in an UHPC experiment to rank cells in order of their CEs. Storing cells for extended periods of time before UHPC measurements can also impact the CEs measured in early charge-discharge cycles, as the SEI layers can mature to varying degrees and lithium can be incorporated within the anode overhang region, which impacts early CE measurements[103]

Ideally in a search for the optimum electrolyte chemistry for a particular cell type, a number of cells differing only in electrolyte composition should undergo formation under the same conditions and be mounted for UHPC testing after the same time interval after

formation. This is the way experiments are carried out in our laboratory where we fill pouch cells with electrolyte and perform the formation steps. Even with this degree of control it is important to consider methods to speed the maturation of the SEI layers to shorten UHPC testing time and improve throughput of UHPC testing systems. Therefore, the purpose of this work was to design a first cycle (formation) protocol that would yield the most passivating SEI and the most stable CE in the shortest amount of time.

Cells from different manufacturers, which may have seen vastly different formation and storage conditions before UHPC testing, should also be considered. Now that UHPC testing systems are relatively common[104–106] device manufacturers need to bring cells from different manufacturers to a common state, if possible, prior to UHPC testing. Finding a way to maximize, or more importantly, standardize the maturity of the SEI layers in purchased cells before UHPC testing may allow for more accurate comparisons between them.

The effects of formation conditions on SEI quality and cell performance have been studied several times over the years. The members of this lab have witnessed many different procedures adopted by many companies ranging from slow formation at or near ambient temperature to rapid formation at elevated temperature. This alone suggests the effect of formation temperature on the quality of the SEI is debateable. Several studies using Li/graphite half-cells with $LiPF_6$ electrolyte have found that the quality of the SEI is best when it is formed at low temperature (20°C)[107–109] but a similar study using $LiClO_4$ electrolyte found that the SEI is best when formed at higher temperatures

(60°C)[110] Studies using full cells with $LiPF_6$ have also shown that higher temperatures (45°C) yield the most passivating SEIs.[111,112] These reports suggest that electrolyte salt, temperature, and the presence of the positive electrode may have an effect on the cell performance and negative electrode SEI quality.

In this work, the effect of cell formation conditions (duration, temperature, and cell voltage) on subsequent CE is investigated, to find preferred conditions for forming a mature SEI that rapidly leads to stable CE. The mechanism by which cells mature is discussed. The effect of cell formation conditions on SEI thickness and chemistry is observed with XPS.

6.1 Finding Preferred Formation Conditions for a Passivating SEI

The standard formation protocol (described fully in the experimental section) was as follows: at 40°C, charge at a rate of C/20 to the upper voltage, hold one hour to equilibrate at this voltage, discharge at C/20 to 3.8 V (~50 % state of charge, SOC) and hold one hour at that voltage to equilibrate. Several modifications to this protocol were made to see what conditions affected the subsequent CE the most. Cells chosen for the initial tests had natural graphite negative electrodes and Al_2O_3-coated NMC622 positive electrodes, were balanced to 4.5 V, and were filled with the most common electrolyte (1.2 M $LiPF_6$ in 3:7 wt. EC:EMC, with 2% wt. VC). Some of these cells were stored for various lengths of time, at different voltages, at 40, 60 or 80°C. Other cells were rapidly

cycled 10 times after formation. The greatest improvement to subsequent CE during the first 10 UHPC cycles was observed when cells were held at 60°C for longer periods of time. To be sure that this trend was not unique to the cell type and electrolyte used, 10 other cell chemistries, listed in Table 6.1.1, were formed either with a) the 40°C standard formation protocol, b) 60°C standard formation, or c) a 60°C modified formation protocol in which the one-hour upper voltage hold was extended to 15 hours. This third formation protocol will henceforth be referred to as the preferred formation protocol.

Table 6.1.1: cell chemistries and upper voltage limits of cells used in this study. In all cases the electrolyte salt was 1.2 M $LiPF_6$ and the solvent was 3:7 wt. EC:EMC except in test #5 where the solvent was just EMC. HV indicates an undisclosed, proprietary "high voltage" coating. The prefix "s" for "s532" signifies that the NMC material consisted of single-crystals, not the usual agglomerated particles.

cell #	***electrolyte additive***	***NMC - coating***	***Graphite***	***Cycling voltages***
1	2% VC	622-Al_2O_3	natural	4.1, 4.2, 4.3 V
2	2% VC	622-HV	natural	4.4 V
3	5% FEC (in EMC)	622-HV	natural	4.2 V
4	PES211	622-Al_2O_3	natural	4.2 V
5	PES211	622-HV	natural	4.2 V
6	PES211	s532	artificial	4.2 V
7	PES222	622-Al_2O_3	natural	4.1, 4.2 V
8	PES222	622-HV	natural	4.2, 4.4 V
9	2% FEC + 1% DTD	s532	artificial	4.2 V
10	VC211	622-Al_2O_3	natural	4.2 V

After formation, the cells were cycled on the UHPC using the same standard protocol: C/20 charge/discharge, between 2.8 V and the upper voltage, at 40°C. Figure 6.1.1a shows CE vs. cycle number for cells with 2% VC and 622A positive electrodes, formed with the three different protocols. When the cells were formed at 40°C, the CE was

initially low, and increased until it plateaued after ~15 cycles. When the cells were formed at 60°C, the initial CE was higher. When the cells were formed at 60°C with the preferred formation protocol, the initial CE was higher still. If the test continued beyond 20 cycles, it is likely that the CE for all three tests would have converged to the same value. The UHPC cycling data for 11 other cell chemistries and voltage limits is shown in Figure 6.1.1b. For ease of viewing (and for the mathematical model described later), coulombic *in*efficiency is plotted vs. the square root of time. The data plotted in this way makes a straight line after the first few cycles. Low CIE in the first three cycles—particularly for the cells that underwent the 15-hour hold at high voltage—is because of capacity gain from the "overhang" region of the negative electrode.[19] The overhang is a narrow region of extra negative electrode that protrudes from the jelly roll, designed to prevent the possibility of having positive electrode with no negative electrode opposite. Over time during a high voltage hold, lithium will fill this overhang region. Lithium slowly leaves the overhang if the cell is subsequently cycled, leading to an apparent increase in capacity.[103] Figure 6.1.1 b shows that, as a general rule, the CIE of cells that underwent formation at 40°C (black) is higher than the CIE of the cells that underwent formation at 60°C (red), which is higher than the CIE of cells that underwent a 15-hour hold at the top of charge during 60°C formation. Near the end of the 20 cycles, the CIEs converge on a representative value for a particular cell chemistry.

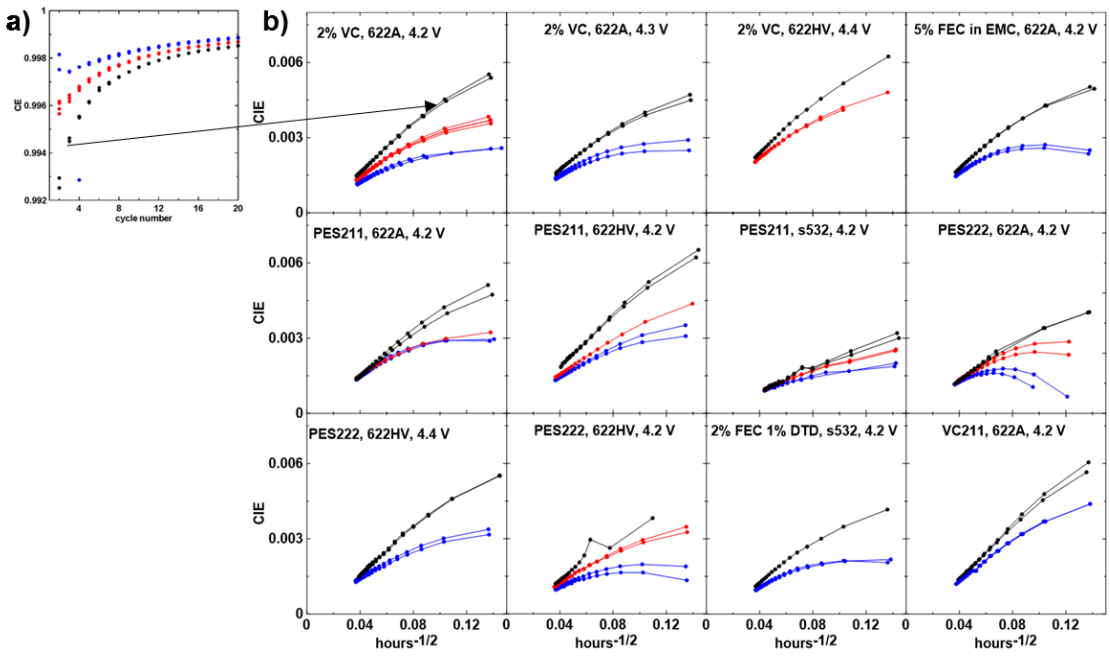

Figure 6.1.1: a) coulombic efficiency vs. cycle number of cells with 2% VC and 622A positive electrodes, b) coulombic inefficiency vs. root time for all the cells listed in Table 6.1.1.

If the preferred formation protocol enabled accelerated UHPC measurements to rank cell chemistries in the same way as slower UHPC measurements, then this project would be deemed a success. Figure 6.1.2 shows the CIE of cells formed with the optimized protocol (60°C, with a 15-hour hold), at cycles 10 and 20, vs. the CIE of the same cells formed with the standard protocol (40°C). The points in indicate the average CIE of duplicate cells, and the lines passing through the dots indicate the difference between pair cells. The points are numbered from left to right, they rank in order of lowest to highest CIE at cycle 20 after standard formation. From bottom to top, the order of the red points is the rank of the cells that underwent the preferred formation, at the 10th cycle. The order of the blue points from bottom to top is the rank of the cells that underwent the optimized formation at the 20th cycle. The ranks obtained after the two formation

protocols (by reading the graph left-right and down-up) are not identical, but they are very similar. The same well-established conclusions can be made 10 cycles after the preferred protocol (rank the red points bottom to top) and 20 cycles after the standard formation (rank the points left to right): i) cells with single crystal NMC532 positive electrodes[102] ii) cells with the ternary additive blend PES211 outperform cells with 2% VC[21]; iii) within cells of the same chemistry, the CIE increases with increasing cycling voltage[21]; iv) in cells with PES211, the Al_2O_3-coated positive electrodes outperform those with the proprietary "high voltage" coating[113] These results suggest that a UHPC experiment, to rank new cells with different chemistries, can be shortened to 10 cycles, if the preferred formation protocol were used.

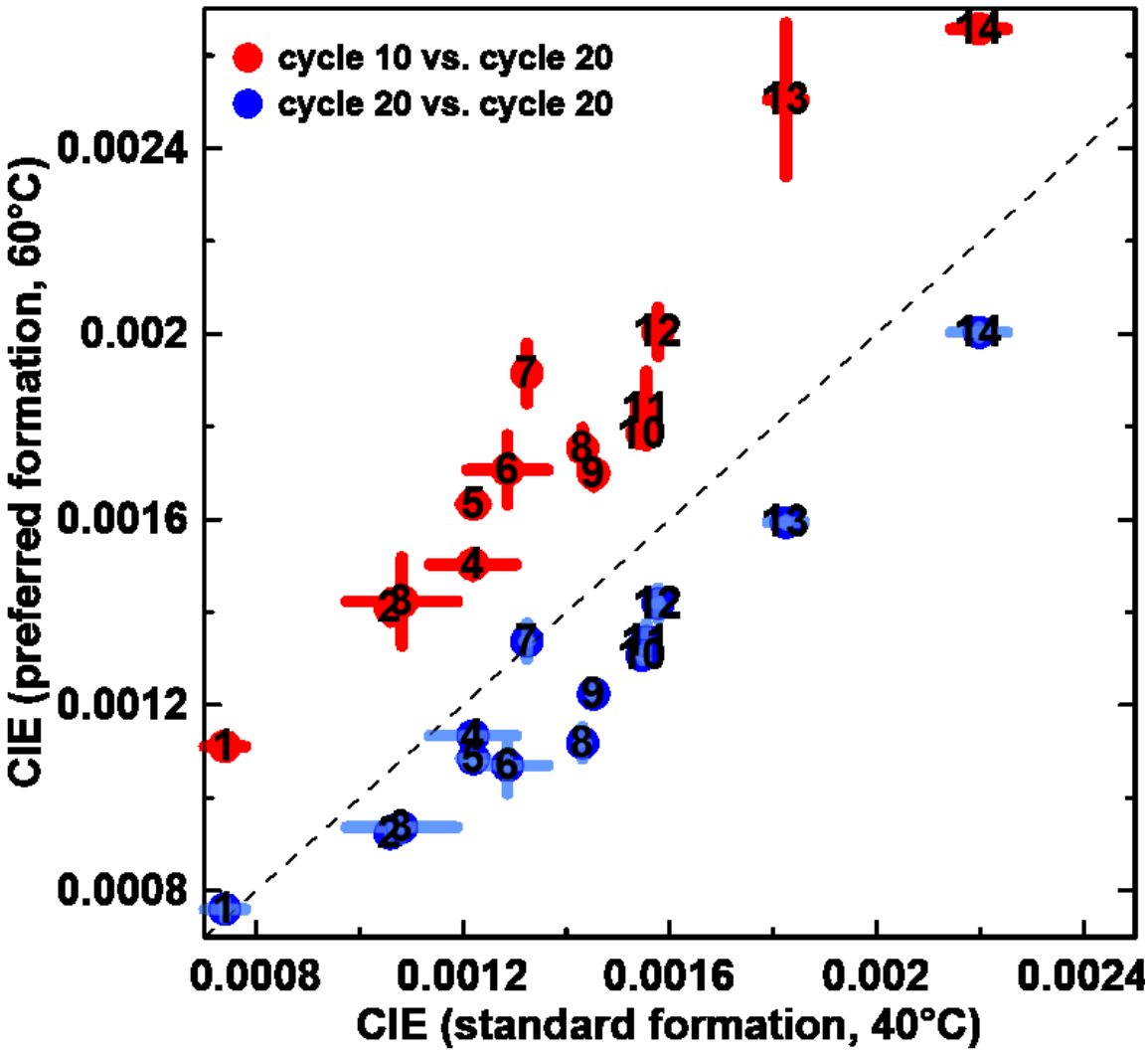

Figure 6.1.2: CIE at cycle 10 (red) or cycle 20 (blue) of cells that underwent the preferred formation (60°C, with 15-hour hold) vs. the CIE at cycle 20 of cells that underwent the standard formation (40°C). The diagonal dashed line has a slope of 1 and shows where the CIEs from the two formation conditions are the same.

Table 6.1.2: cell chemistries from Figure 6.1.3 ranked by order of CIE after standard formation.

Label (40°C Rank)	*Additive*	*Positive electrode*	*Cycling voltage*
1	**PES211**	**SC532**	**4.2 V**
2	**2%FEC 1%DTD**	**SC532**	**4.2 V**
3	**PES211**	**622A**	**4.1 V**
4	**PES222**	**622A**	**4.2 V**
5	**PES222**	**622HV**	**4.2 V**
6	**2% VC**	**622A**	**4.1 V**
7	**PES211**	**622A**	**4.2 V**
8	**2% VC**	**622A**	**4.2 V**
9	**VC211**	**622A**	**4.2 V**
10	**PES211**	**622HV**	**4.2 V**
11	**2% VC**	**622A**	**4.3 V**
12	**5% FEC**	**622A**	**4.2 V**
13	**PES222**	**622HV**	**4.4 V**
14	**2% VC**	**622HV**	**4.4 V**

Figure 6.1.2 shows that after 20 cycles, most cells formed with the preferred protocol have lower CIEs than the cells cycled with the standard protocol (all the blue points are below the dashed line). This begs the question: Did the preferred formation protocol mature the cells (the CIEs will converge at a later point), or did the preferred formation improve the cell chemistry (the CIE of cells that underwent the preferred formation will always be better than the others')? It appears that the former is the case, since [26]Figure 6.1.4 shows that the volume change after formation and UHPC cycling, R_{ct} after formation, and the capacity fade from long-term cycling are all the same, within experimental error, for cells with 2% VC and 622A positive electrodes, cycled to 4.2 V. This shows that the additional 15 hours of storage at 4.2 V and 60°C did not have a detrimental or lasting positive impact on cell performance.

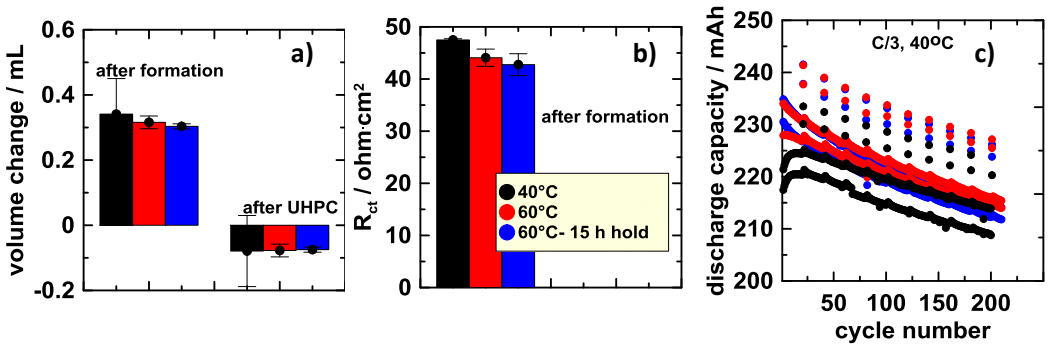

Figure 6.1.4: a) volume change after formation and after 20 UHPC cycles, b) R_{ct} after formation, and c) capacity vs. cycle number after UHPC testing for cells with 2% VC and 622A positive electrodes, cycled at C/3 to 4.2 V.

6.2 Modeling Cell Maturity vs. Time

CIE has sometimes been modeled as inversely proportional to the degree of passivation, x, at a time, t, and proportional to a SEI passivation growth constant, k[97,114]

$$\frac{dx}{dt} = \frac{k}{x} \propto CIE. \quad (17)$$

The degree of passivation, x_1, at a time, t_1, and the CIE can be found by integration and substitution:

$$\left[\frac{x^2}{2}\right]_0^{x_1} = [k\,t]_0^{t1} \quad (18)$$

$$x_1 = \sqrt{2k\,t_1} \quad (19)$$

$$\frac{dx}{dt} = \frac{\sqrt{2\,k}}{2\sqrt{t}} \propto CIE \quad (20)$$

If the temperature of the cell is fixed at 60°C from t = 0 till t = t_1 and is then changed from 60°C to 40°C, at a time, t_1, the expression for the CIE changes for the time period between t_1 and t_2, to reflect the change in passivation constant, k:

$$\left[\frac{x^2}{2}\right]_{x_1}^{x_2} = [k_{40°C}\, t]_{t_1}^{t_2} \quad (21)$$

$$\frac{x_2^2}{2} - \frac{x_1^2}{2} = k_{40°C}\,(t_2 - t_1) \quad (22)$$

Equation (19) is used to substitute for $x_1^2/2$ to get:

$$\frac{x_2^2}{2} - k_{60°C}\, t_1 = k_{40°C}\,(t_2 - t_1) \quad (23)$$

$$x_2 = \sqrt{2(\, k_{40°C}\,(\, t_2 - t_1 + \frac{k_{60°C}}{k_{40°C}}\, t_1\,)} \quad (24)$$

$$\frac{dx_2}{dt} = \frac{\sqrt{k_{40°C}}}{\sqrt{2\,(\, t_2 - t_1 + \frac{k_{60°C}}{k_{40°C}}\, t_1)}} \propto CIE \quad (25)$$

Equations (20) and (25) are shown graphically in Figure 6.2.1 a. Equation (20) is used to model the SEI maturity of cells that were formed and cycled at 40°C. Equation (25) is used to model the SEI of cells that were formed at 60°C (for a duration of t_1) and subsequently cycled at 40°C. Equations (20) and (25) were fit to the data in Figure 6.1.1, using a least squares fitting routine, to determine the k values at 40 and 60°C. For the cells with 2% VC and 622A positive electrodes, cycled to 4.2 V, k_{60} was found to be about nine times k_{40}. This suggests that the SEIs matures nine times faster at 60°C than it does at 40°C for this cell chemistry. CE vs. cycle number for these cells, calculated using

the k values from the fit, is shown in Figure 6.2.1b. The calculated CE bears a good resemblance to the measured CE, which suggests that this model is a decent approximation for cell maturity.

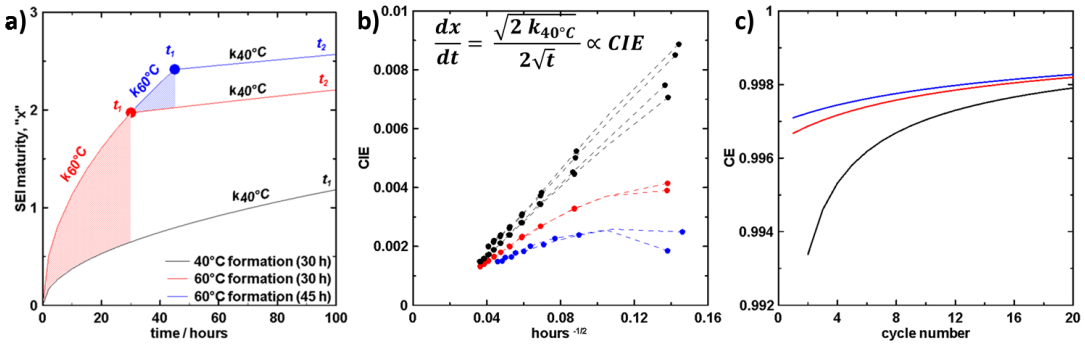

Figure 6.2.1: a) SEI maturity vs. time, calculated from Equations (20) and (25), for cells that underwent different formaton protocols, b) CIE vs. square root time, from Figure 6.1.1a, fit to Equations (20) and (25) by varying k, c) CE vs. cycle number, calculated using k values obtained from the fit shown in b.

6.3 Probing the Mechanism of Cell Maturity

The model described above was previously used to model negative electrode SEI maturity as a function of time at different temperatures [97] However, the improvement in CIE from the preferred protocol is not strongly related to reduced discharge capacity, Q_d, fade (a hallmark of good negative electrode passivation). Figure 6.3.1shows that the capacity fade is not very different when the cells are formed with the different formation protocols. To easily compare the contribution of fade to the CIE, the fade in Figure 6.3.1b is plotted as fractional fade per cycle. CIE is the sum of the fractional fade (Q_d lost in a cycle) and the fractional charge-endpoint capacity slippage (slipC, due to oxidation of species at the positive electrode):

$$CIE = \frac{fade}{Qd} + \frac{slipC}{Qd} \quad (26)$$

The improvement in CIE is more strongly related to reduced charge endpoint capacity slippage, as shown by Figure 6.3.2. This is observed again in Figure 6.3.3, which shows that increasing the temperature and the time spent at high voltage during formation reduces the amount of self-discharge during open-circuit voltage storage at 60°C. Evidently the preferred formation protocol reduces parasitic redox reactions at the positive electrode, more than at the negative electrode. This may explain why early studies on Li/graphite half-cells found that found that low temperature resulted in better passivation[107–109] while later studies on graphite/positive electrode full-cells found the opposite, that high temperature formation resulted in better passivation[111,112]

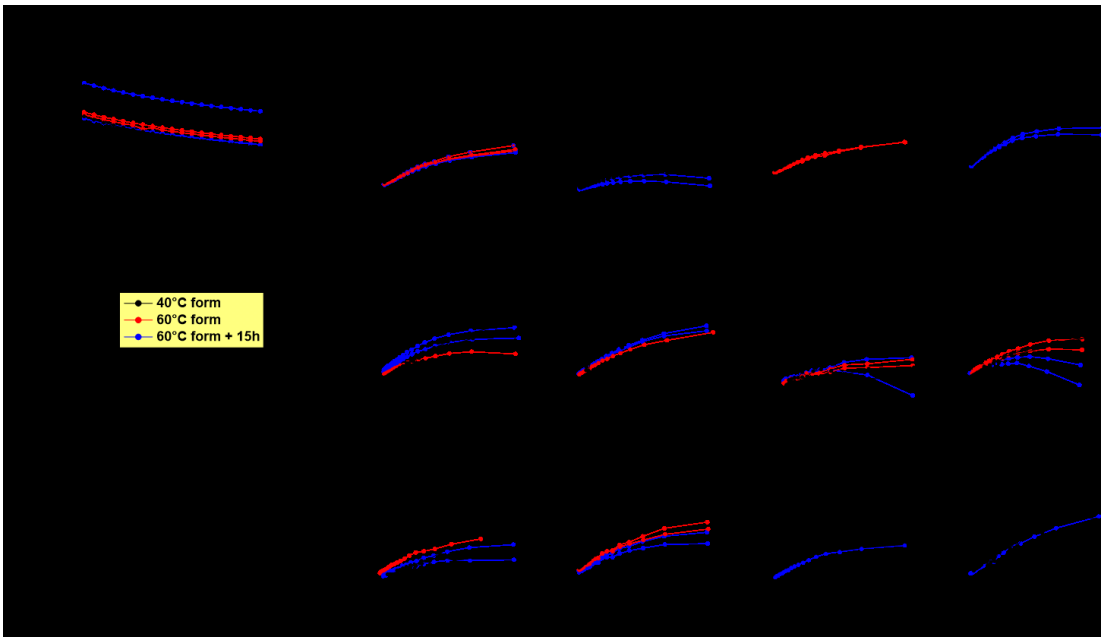

Figure 6.3.1: a) discharge capacity vs. cycle number for cells with 2% VC and 622A positive electrodes, b) fractional capacity fade vs. square root of time for all the cell types listed in Table 6.1.1.

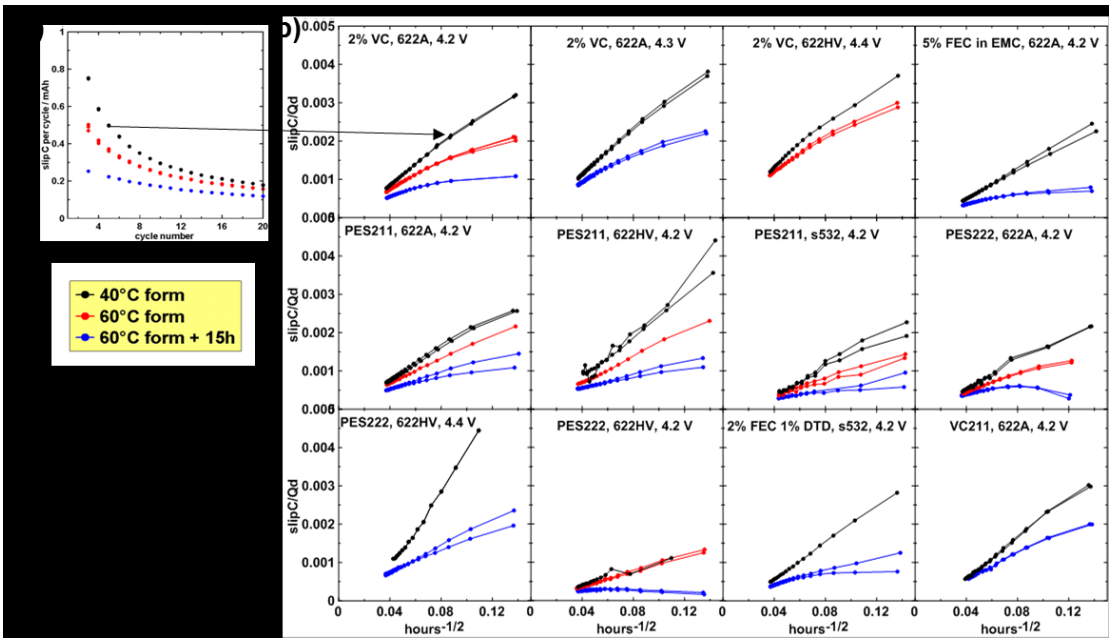

Figure 6.3.2: a) charge endpoint capacity slippage per cycle vs. cycle number for cells with 2% VC and 622A positive electrodes, b) fractional charge endpoint capacity slippage vs. square root of time for all the cell types listed in Table 6.1.1.

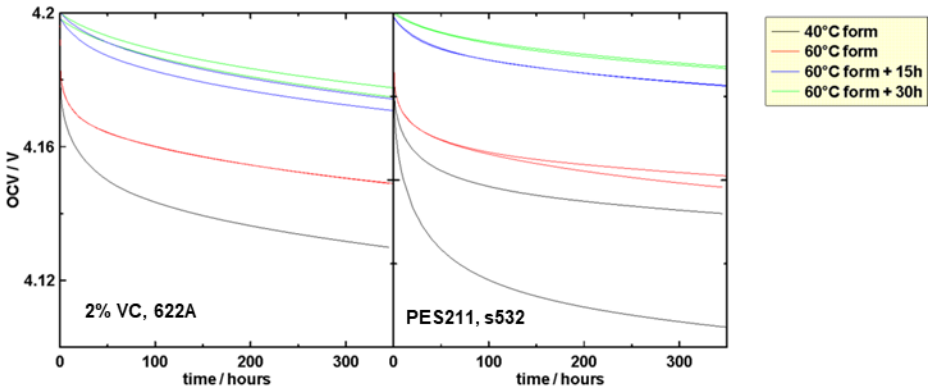

Figure 6.3.3: OCV vs. storage time for cells that were formed at 40°C or 60°C with a 1, 15 or 30 hour hold at 4.2 V.

The cause of reduced charge endpoint capacity slippage and voltage drop after the preferred formation could be due either to a) the increased time spent at 60°C (in accordance with the model suggested in the previous section), or b) the increased time spent at high voltage, during which the positive electrode oxidizes and removes some soluble species that are generated from the reduction of electrolyte and negative electrode SEI formation. In either case, the effect is possibly due to the presence of lithium alkoxides, formed from the reduction of linear alkyl carbonates at insufficiently passivated negative electrodes. Lithium alkoxides are known to oxidize at the positive electrode, causing voltage drop and charge endpoint capacity slippage. [115]

To see whether temperature or voltage had the greatest impact on the initial CIE and charge endpoint capacity slippage, cells with 2% VC and 622A positive electrodes were formed at either 40°C or 60°C, with the 15-hour voltage hold done at a variety of voltages in the first charge. The CIE and fractional charge endpoint capacity slippages of

these cells during subsequent UHPC cycling are shown in Figure 6.3.4. The cells with the lowest initial CIE and charge endpoint capacity slippage are those that that underwent formation at 60°C, among which there is little difference between those that were held at different voltages. This suggests that the benefit of the preferred formation protocol is due to the increased length of time spent at 60°C, not the increased exposure to high voltage. This result agrees with the mathematical model for SEI maturity described above.

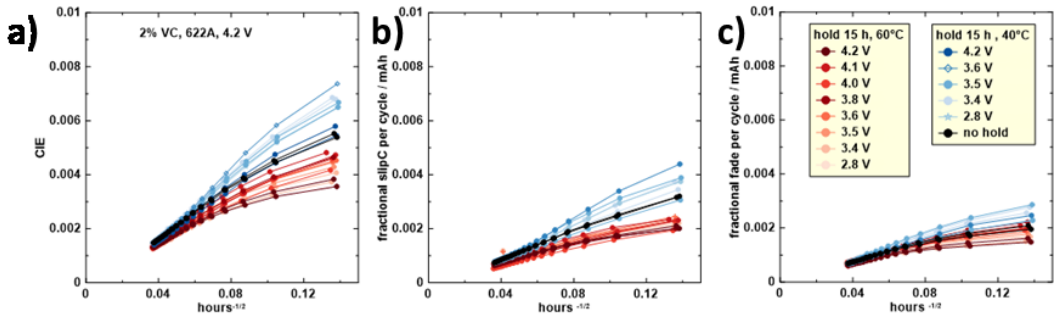

Figure 6.3.4: a) CIE, b) fractional charge endpoint capacity slippage per cycle, and c) fractional fade per cycle plotted versus square root of time for cells (622A with 2% VC) that underwent formation at 40°C (blue) or 60°C (red), with 15-hour voltage holds done at various points during the first charge.

To see what effects the preferred formation had on the positive and negative SEIs, and to better understand what "a mature SEI" means in a physical sense—be it a thickened SEI layer, or a SEI of a certain chemistry—XPS was done on electrodes from cells after standard formation at 40°C, 60°C, or after the optimized formation. The XPS spectra of these electrodes (from cells with 2% VC and 622A positive electrodes) are shown in Figure 6.3.5. The XPS spectra of the positive electrodes were virtually identical,

indicating that the SEI composition of the positive electrodes were very similar, regardless of the protocol used during formation. The thickness of the positive electrode SEI, inferred from the area of the NMC lattice oxygen peak, at 529 eV, is virtually the same for all three positive electrodes. This result agrees with previous work, done with cyclic voltammetry and electrochemical quartz microbalance, which showed that oxidation of electrolyte does not cause the precipitation of oxidized species on the positive electrode. [37]

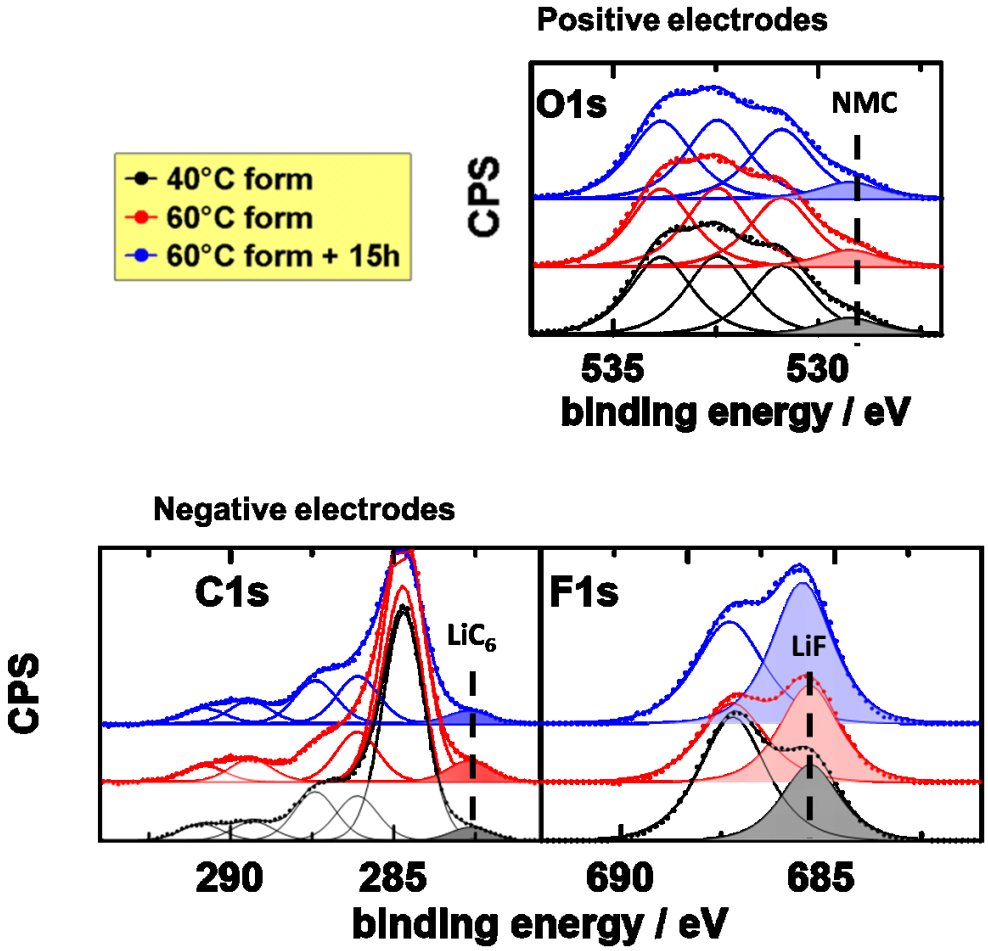

Figure 6.3.5: XPS spectra of positive and negative electrodes taken from 622A cells with 2% VC after standard formation at 40°C or 60°C, or after the preferred formation at 60°C , which included a 15-hour hold at 4.2 V.

The XPS spectra of the negative electrodes also show no compelling evidence for a thickened SEI on more mature electrodes, judging from the area of the lithiated graphite, LiC_6, peak at 283 eV. The area of this peak is approximately the same in all cases, indicating that the overlying SEI is approximately the same thickness. The most significant difference between the three negative electrodes is the relative amount of LiF. This suggests that the SEI ages not by growing thicker, but by becoming more inorganic over time, as others have observed[94,116–118] It is proposed that $LiPF_6$ from the electrolyte reacts with carbonates (or hemi-carbonates, RCO_3Li) in the SEI, to form LiF by Equations (27) or (28):

$$2\ RCO_3Li + LiPF_6 \rightarrow 2\ LiF + 2\ RF + LiPO_2F_2 + 2\ CO_2 \qquad (27)$$

$$RCO_3Li + LiPF_6 \rightarrow 2\ LiF + RF + POF_3 + CO_2. \qquad (28)$$

The evolution of $LiPO_2F_2$ may be a contributing factor to the maturity of cells, since many recent reports have shown that $LiPO_2F_2$ is a beneficial electrolyte additive. [77–79]Although $LiPO_2F_2$ is soluble only up to 1.6 wt.%, very small amounts of $LiPO_2F_2$ have been shown to significantly improve charge endpoint capacity slippage and voltage drop during storage in lithium-ion cells[79] It has been suggested by Leroy *et al.*[116] that evolution of LiF could occur from the reaction of acidic species with carbonates in the SEI, according to Equation (29):

$$RCO_3Li + 2HF \rightarrow LiF + RF + H_2O + CO_2. \qquad (29)$$

Acidic species can be formed by the reaction of $LiPF_6$ with moisture impurities. Acidic species can also be evolved from the oxidation of electrolyte species or H_2 at the positive electrode,[42,43,83] which may explain why some have observed increased amounts of LiF on graphite electrodes when cells are cycled to higher voltages[119] In any case, the

appearance of LiF on the negative electrode in this work is correlated with SEI maturity and decreased parasitic reactions.

6.4 Conclusions

The initial purpose of this work was to create a formation protocol that would allow for shorter UHPC experiments, by accelerating the maturity of new cells. This was achieved by forming cells at 60°C, instead of 40°C, and by prolonging the duration of the formation cycle by 15 hours. The preferred formation protocol gave neither short-term damage, nor permanent advantage to the cells formed with the standard formation protocol. It was found that the preferred protocol benefitted the cells by reducing the initial rate of charge endpoint capacity slippage. This is likely because incomplete passivation causes lithium alkoxides to be evolved, which are subsequently oxidized at the positive electrode, causing reversible self-discharge. The preferred formation protocol did not lead to thickening of the SEI on either electrode, but more inorganic species were observed in the SEI of the negative electrodes that spent longer at 60°C. This suggests that $LiPF_6$ reacts with carbonates in the SEI to create a more inorganic SEI over time (perhaps with the evolution of $LiPO_2F_2$, a beneficial electrolyte additive). It is possible that this change in SEI chemistry is correlated with the improved CE of cells that underwent the preferred formation protocol.

CHAPTER 7 A NEW WAY TO MEASURE CHANGES IN ELECTROLYTE COMPOSITION

Leah Ellis devised the concept for this work (using FTIR as an analytical tool for determining the concentration of species in electrolyte). Sam Buteau, a graduate student, devised the machine learning (ML) algorithm to facilitate data analysis. Sam Hames, an undergraduate student under the supervision of Leah Ellis, prepared the electrolytes and measured their FTIR spectra. Lauren Thompson, a graduate student, obtained the GC-MS and ICP-OES measurements. Text and figures in this chapter are reproduced with permission from *J. Electrochem. Soc*, **165**:A256 (2018). Copyright 2018, The Electrochemical Society.

A dominant cause of lithium-ion cell failure, especially in high voltage cells, is degradation of the electrolyte, particularly at the surface of the charged electrodes.[2] Most studies on the topic of cell degradation and electrolyte decomposition have focused on the formation of films of electrolyte decomposition products which build up on the surfaces of the electrodes.[2,4,62] These films contain chemical moieties derived from both the electrolyte solvents and the electrolyte salt, $LiPF_6$. Although mechanisms for the consumption of solvents[29,58,80] and $LiPF_6$[31,33,74] in lithium-ion cells have been determined, there have been few systematic studies which quantify the changes in the bulk electrolyte as a function of cell aging.

Quantitative analyses of electrolyte solutions typically employ nuclear magnetic resonance (NMR) spectroscopy, gas chromatography (GC), high performance liquid chromatography (HPLC), and inductively coupled plasma optical emission spectrometry (ICP-OES).[58,120–132] These instruments are costly, and these methods require the preparation and measurement of many calibration solutions. Often the columns or detectors used in chromatography experiments cannot be exposed to the high temperature decomposition products of $LiPF_6$, so these experiments often focus on the organic portions of the electrolyte, after the water-soluble portions of the electrolyte have been removed.[58]

A method of determining the concentration of $LiPF_6$ and weight fractions of solvents in unknown electrolyte solutions, using Fourier transform infrared (FTIR) spectroscopy is presented here. Until now, FTIR has only been used for qualitative electrolyte analysis, and for the determination of solvation structures. [133–135] Quantitative analysis was achieved using a ML algorithm to match features in the FTIR spectra of unknown electrolyte solutions to those interpolated from a spectral database of known electrolyte solutions. This method is very fast. Once the spectral database and ML algorithm have been set up, there is no need for sample preparation, instrument calibration, or for data manipulation. The accuracy and precision of this method was first validated by determining the concentration of $LiPF_6$ and weight fractions of solvents in known "unknown" solutions. Then the method was used to determine the $LiPF_6$ concentration and weight fractions of solvents in the electrolyte extracted from aged lithium-ion cells. The results were found to be in good agreement with results from GC/mass spectrometry

(MS) and ICP-OES measured on the same electrolytes. This method is easy, fast and allows for systematic studies of liquid electrolytes in lithium-ion cells as they age.

7.1 How FTIR Signals Change with Changing Electrolyte Composition

Figure 7.1.1 shows FTIR spectra of electrolyte solutions with various concentrations of $LiPF_6$, EC, and DMC. The bottom-right corner shows the spectrum of pure DMC. As the amount of $LiPF_6$ in DMC increases, certain features in the FTIR spectra evolve, in proportion to the amount of $LiPF_6$. The most prominent and well-known of these changes is to the carbonyl, C=O, stretching peak, at ~1750 cm^{-1}.[133,135–139] The carbonyl peak splits upon the introduction of $LiPF_6$. This is a result of the coordination of the carbonyl group of the solvent molecules to the Li^+ of the dissociated $LiPF_6$. The absorbance of this split peak grows with increasing $LiPF_6$ concentration (highlighted in green in Figure 7.1.1). This carbonyl peak is one of the spectral features used by the ML algorithm, discussed later, to determine the concentration of $LiPF_6$ in a solution of organic carbonates. In a similar way, the ML algorithm determines the concentration of EC and DMC from the presence of spectral features that vary with the solvent ratio. For EC, these include the peaks between 1050 – 1200 cm^{-1} that grow with increasing EC content, which are caused by the twisting of the adjacent CH_2 groups in EC.[140] The presence of DMC can be determined from the strong absorption at 1290 cm^{-1}, corresponding to the carbonyl symmetric stretching. This can be clearly distinguished from carbonyl asymmetric stretching of EC, which occurs at a much lower wavenumber, 1170 cm^{-1}.

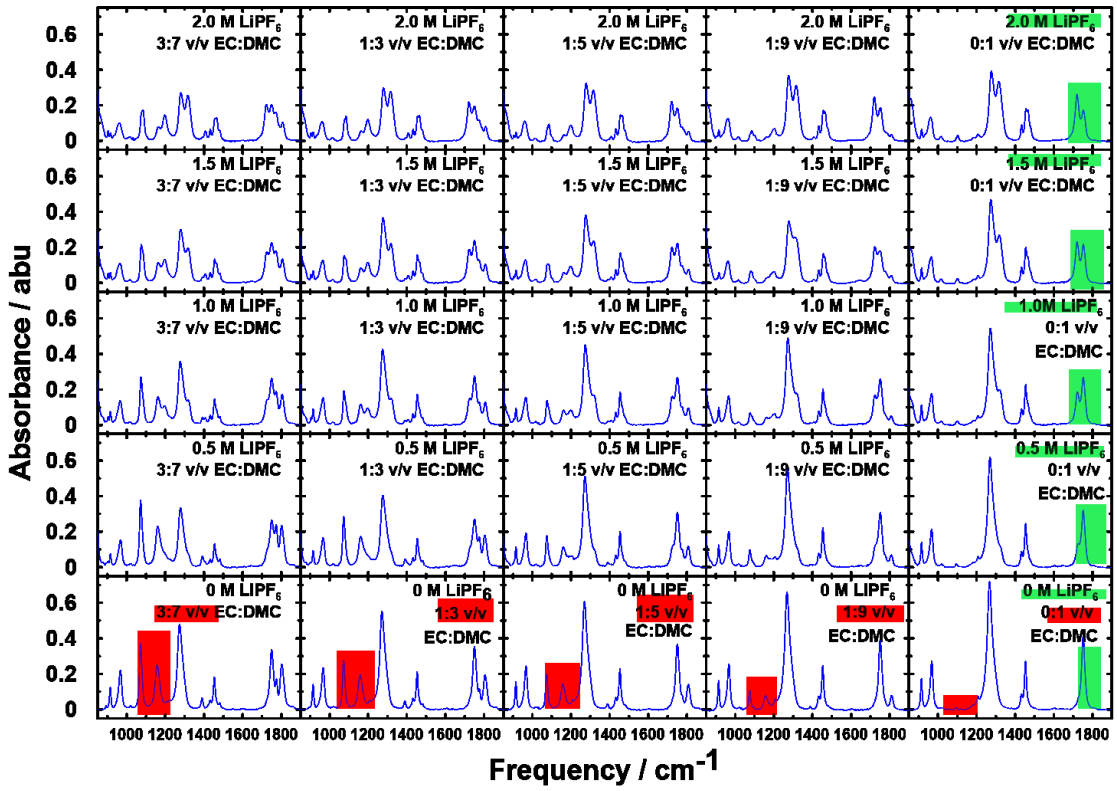

Figure 7.1.1: a) FTIR spectra of electrolyte solutions with a range of $LiPF_6$, EC, and DMC concentrations. Green highlights the evolution of a spectral feature that is strongly correlated with [$LiPF_6$] in DMC solutions. Red highlights the evolution of a spectral feature that is correlated with [EC] in DMC solutions.

7.2 Machine Learning

The FTIR/ML software was written in Mathematica 11.1. [21] First, the raw FTIR spectra were normalized such that the total integrated area over the range 650 – 2000 cm^{-1} equalled one. Then, *n* selected features in the absorbance spectra (see Table 1) of each of the 81 database samples were measured. For example, one such feature consists of the area of the normalized signal in a region centred around 839 cm^{-1} and with a half width of

25 cm^{-1}. This procedure produces an *n*-component array of values, where each *n*-component array is associated with a database sample of known composition.

The value (either the integrated area or the weighted central wavenumber within a pre-defined region) produced by each of the *n* features in the spectra vary smoothly with composition in the 9 x 9 array of database samples. The variation of each feature with composition can be well fitted to a surface of the form of Equation (30):

$$F_n(x,y) = a_n + b_n x + c_n y + d_n x y + e_n x^2 + f_n y^2, \quad (30)$$

where F_n is the value (area or weighted central wavenumber) of the n^{th} spectral feature, *x* is the $LiPF_6$ concentration, and *y* is the volume % ratio of EC in the EC/DMC solution. The parameters a_n, b_n, c_n, d_n, e_n and f_n are adjustable parameters and the index, *n*, runs over all the spectra features considered. These parameters are adjusted by least squares fitting to the areas or weighted central wavenumbers of the 81 database samples. A larger or smaller number of spectral features can be considered as desired.

The features selected from the spectra were determined by trial and visualization. The feature values for the database samples together with the fitted surface were plotted to determine which spectral features yielded a large slope with composition and good agreement between the measurements and the fit. Many suitable features were found, and the best $n = 12$ were selected. Then, these features were rescaled to weigh their contribution according to their signal-to-noise ratio.

To determine the $LiPF_6$ concentration and EC/DMC ratio of an unknown sample, the FTIR spectrum of the unknown was first measured. Then the intensities or central wavenumbers of the n =12 selected spectral features were determined. Least squares fitting to the n =12 surfaces described by equation (30) was performed to determine which values of x and y gave the best fit. Thus, the composition of an unknown sample could be determined.

Figure 7.2.1 illustrates the operation of the machine learning algorithm, constructed by Sam Buteau. Figure 7.2.1a shows a representative FTIR spectrum of an electrolyte blend. The spectrum has been normalized such that the total integrated area over the range 650 – 2000 cm^{-1} is equal to one. To characterize this solution, the features of this spectrum are analyzed by the ML algorithm. In this work, twelve regions and features were used to determine the concentration of $LiPF_6$ and the weight fraction of the solvents. These twelve regions and features are described in Table 7.2.1**.** [138,140,141]Features 7 and 10 from Table 7.2.1 are highlighted on the sample FTIR spectrum in Figure 7.2.1a, in green and red, respectively. Figure 7.2.1b and Figure 7.2.1c, show the integrated area of Features 10 and 7 over a range of solution compositions, respectively. Feature 10 is labeled as an [$LiPF_6$]-determining feature in Table 7.2.1, because the slope of the surface with $LiPF_6$ concentration is large in that surface. In contrast, Feature 7 can be used to determine both EC and $LiPF_6$ content since the surface in Figure 7.2.1c slopes strongly in both EC and $LiPF_6$ content. In reality, however, all 12 features are used by the ML algorithm for the determination of both the solvent ratio and the $LiPF_6$ concentration. The black dots in Figure 7.2.1b and Figure 7.2.1c mark measurements of the prepared database solutions

used to create the model (the FTIR spectra of some these solutions were shown in Figure 7.1.1). The arrows in Figure 7.2.1 show the position of the FTIR features from Figure 7.2.1a. Surfaces, as in Figure 7.2.1b and Figure 7.2.1c, were fitted to the intensity of the 12 spectral features in Table 7.2.1 as a function of $LiPF_6$ concentration and solvent ratio. The equations for these 12 surfaces then "trained" the model. The FTIR spectrum of an unknown is then measured and the intensities of the 12 spectral features in the spectrum of the unknown are calculated. Least-squares fitting was used to determine the best choice of the $LiPF_6$ concentration and solvent ratio that match the 12 measured and database spectral feature intensities.

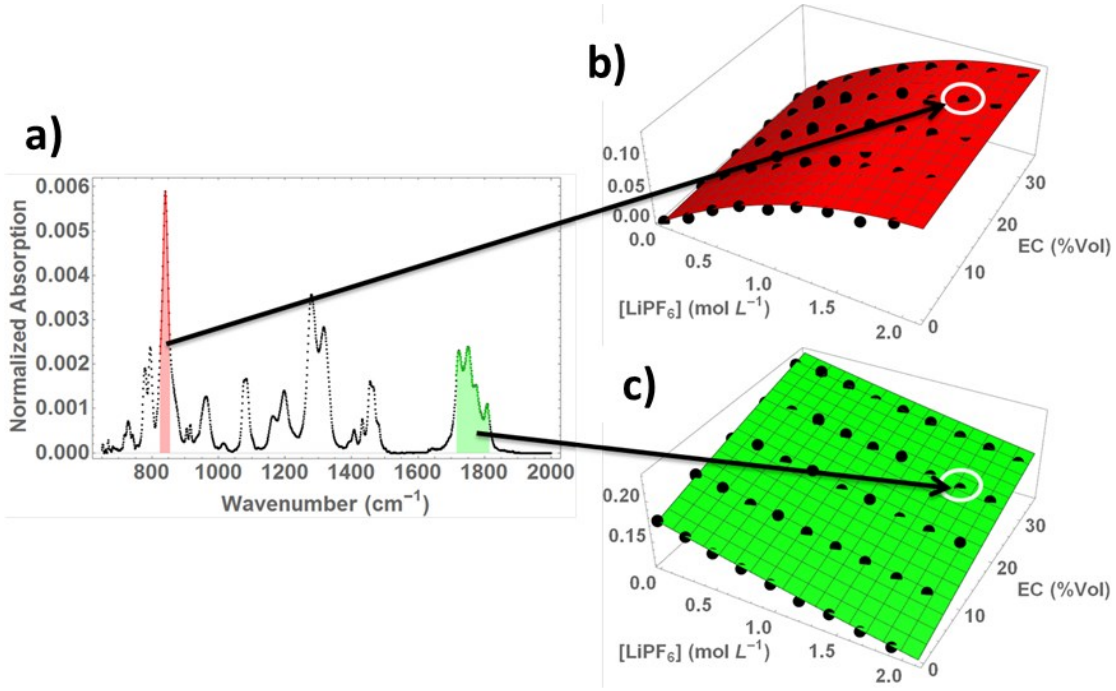

Figure 7.2.1: a) FTIR spectrum of an electrolyte solution composed of 1.75 M $LiPF_6$, 25% (vol) EC in DMC. Red highlights a prominent spectral feature that is strongly correlated with [$LiPF_6$] (feature 10 in Table 7.2.1). Green highlights a prominent spectral feature that is correlated with [EC] (feature 7 in Table 7.2.). B) and c) show the variation of these spectral features over a range of electrolyte compositions.

Table 7.2.1: FTIR regions, features and vibrational modes used for the determination of [EC] and [$LiPF_6$]

	Region / cm^{-1}	*Feature*	*Assignment*
[EC]:			
1)	780 ± 25	Center	CO_3 non-planar rock
2)	1170 ± 40	Area	CO_2 symmetric stretch (EC)
3)	1270 ± 30	Center	CO_2 symmetric stretch (DMC)
4)	1290 ± 75	Center	CO_2 symmetric stretch (DMC)
5)	1443 ± 60	Center	C-O asymmetric stretch
6)	1710 ± 20	Area	C=O, stretch
7)	1775 ± 80	Area	C=O, stretch
8)	1775 ± 60	Center	C=O, stretch
[$LiPF_6$]:			
9)	780 ± 25	Area	CO_3 non-planar rock
10)	839 ± 25	Area	$LiPF_6$ t_{1u}
11)	1290 ± 75	Center	CO_2 symmetric stretch (DMC)
12)	1320 ± 30	Center	CO_2 symmetric stretch

7.3 Proof of Concept

Figure 7.3.1 shows the results of a "proof of concept" experiment, in which the composition of five known "unknown" solutions were characterized by the method described above. These solutions were prepared and characterized by different people, so that their compositions remained unknown at the time of analysis. The first solution was pure DMC. The other four solutions contained DMC, $LiPF_6$, EC and sometimes small amounts of common electrolyte additives. The proportions of the electrolyte additives and electrolyte components were chosen to be representative of typical electrolytes that could be used in lithium-ion cells. Figure 7.3.1 shows that the ML algorithm determined the relative ratios of $LiPF_6$, EC and DMC in the electrolyte solutions with accuracy and precision, despite the presence of small amounts of electrolyte additives which were not included in the algorithm's training matrix. This result served as a proof of concept for

the FTIR/ML method for determining the approximate composition of electrolytes based on $LiPF_6$, EC and DMC.

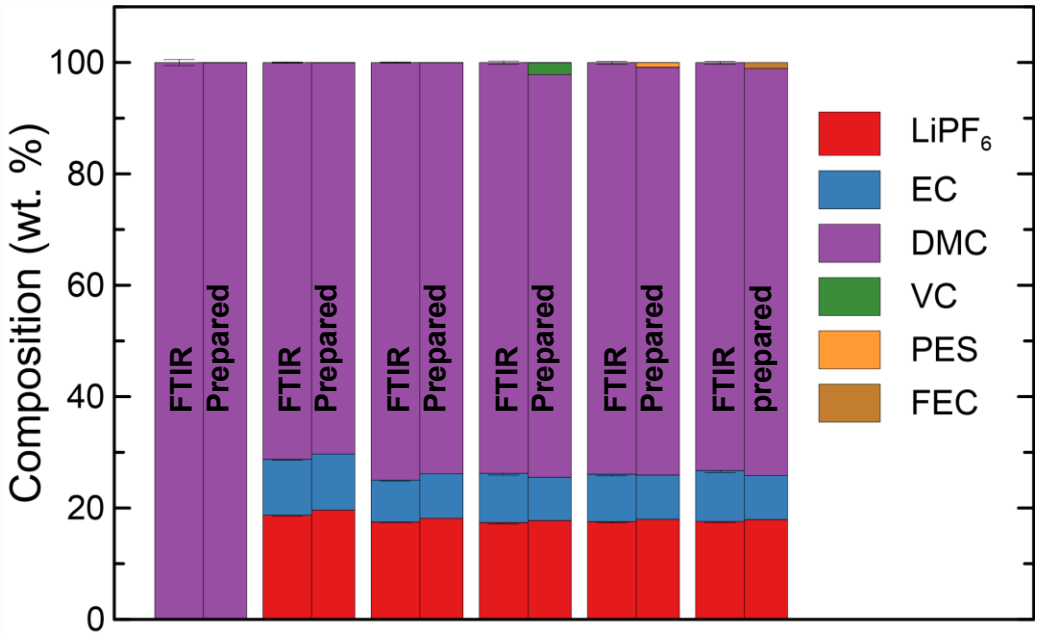

Figure 7.3.1: the composition of six solutions that were characterized in a "blind" FTIR/ML analysis compared to their known compositions.

Table 7.3.1 compares the sensitivity, speed and cost of the FTIR/ML method against other analytical tools that are commonly used for characterizing electrolyte in lithium-ion cells. This method has competitive accuracy but is not sensitive to electrolyte additives and other trace components. However, it has several substantial advantages over other methods. The first advantage of the FTIR/ML method is speed of analysis. Only several seconds were needed to measure each FTIR spectrum. Only several milliseconds of computer time were needed to analyze each FTIR spectrum with the existing spectral

database and ML algorithm. Considerably more time and effort would be needed to characterize these solutions with other methods. GC-MS requires over one hour per sample, for sample preparation, data collection and analysis. NMR and ICP-OES also require several minutes for sample preparation, preparation of calibration solutions, and data analysis. The second advantage of FTIR method is that it does not require sample preparation. Electrolyte can be analyzed neat, as opposed to other methods, where electrolyte must be diluted in harsh or expensive solutions. The third advantage of the FTIR/ML method is that it can quantify both the solvent and the salt concentrations simultaneously, albeit with somewhat less accuracy than GC-MS and ICP-OES methods. It is expected, however, that the accuracy and sensitivity of the FTIR method will suffice for the analysis of principle electrolyte components (> 5% wt.) in aged lithium-ion cells, where large amounts of capacity fade are expected to cause changes in the electrolyte. The final advantage of the FTIR/ML method is cost. The FTIR instrument used in this work was purchased for ~ $18,000 USD, which is about an order of magnitude less than the cost of the other instruments in Table 7.3.1.

Table 7.3.1: comparison of common methods for the characterization of electrolyte solutions.

method	**Analytes**	**Approximate Accuracy**	**Preparation**	**Speed***	**Instrument cost**
FTIR-ML	Solvents $LiPF_6$	3-5 wt. % 5 % in molarity	none	~ 1m	~$18,000 USD
GC-MS	Solvents Additives Trace components	1-2 wt. %	Extraction, CH_2Cl_2	~ 1h	~$100,000 USD
ICP-OES	$LiPF_6$	3-5 wt. %	Dilution, HNO_3	~ 1h	~$100,000 USD
NMR	Solvents $LiPF_6$ Additives Trace components	hard to make fully quantitative	Dilution, deuterated solvent	~30 m	> $100,000 USD

* the approximate sum of time spent on preparing one electrolyte sample, acquiring data and analyzing the data to determine the concentration of components.

Figure 7.3.2a compares the results of the FTIR and GC-MS/ICP-OES analysis on electrolyte extracted from aged lithium-ion cells. Figure 7.3.2b shows capacity vs. cycle number for the cells, which were cycled at 55°C, at a rate of C/3, between 3.1 V and 4.1, 4.3, or 4.5 V. These cells only exhibited a small amount of capacity fade and hence the expected changes to the electrolyte are small. The cells were filled with electrolyte which was prepared to contain $LiPF_6$, EC and DMC in a 14.3/25.7/60.0 wt. ratio. This electrolyte was measured by GC-MS, ICP-OES and FTIR/ML shortly after it was prepared. The ratios of $LiPF_6$, EC and DMC were found to be 13.1/26.5/60.4 by GC-MS and ICP-OES, and 13.3/27.5/59.3 by FTIR/ML. By GC-MS and ICP-OES the wt. ratios of $LiPF_6$, EC and DMC in electrolytes from cycled cells were found to be 9.8/29.5/60.7 for the cells cycled to 4.1 V, 12.5/29.8/57.8 for the cells cycled to 4.3 V, and 11.8/30/2/58.0 for the cells cycled to 4.5 V. By FTIR the wt. ratio of $LiPF_6$, EC and DMC in electrolytes from cycled cells were found to be 10.1/25.3/64.6 for the cells

cycled to 4.1 V, 11.4/25.4/63.2 for the cells cycled to 4.3 V, and 10.5/26.3/63.3 for the cells cycled to 4.5 V. Table 7.3.2 summarizes the results for the fresh electrolyte and for the electrolyte found in the cycled cells. Both ICP-OES and FTIR/ML methods show that 10-20 % of the $LiPF_6$ in these cells was lost during cycling. This could be caused by the thermal decomposition of $LiPF_6$ at elevated temperature, and by the inclusion of $LiPF_6$ decomposition products in the thickening negative electrode SEI. [38–42] The GC-MS and FTIR/ML methods do not come to the same result for the EC/DMC ratio. It is unclear whether this discrepancy occurred from preferential evaporation of the DMC during the preparation of the GC-MS sample, or from the uncertainties within the ML algorithm.

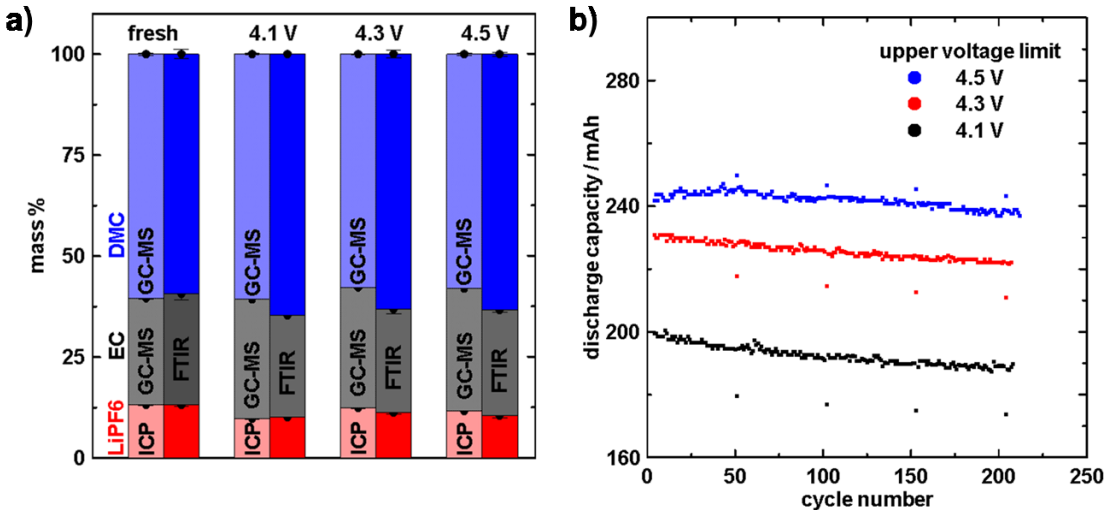

Figure 7.3.2: a) the composition of electrolyte extracted from cycled cells, determined by GC-MS and ICP-OES, or by FTIR, b) capacity vs. cycle number for these cells.

Table 7.3.2: major components of the fresh electrolyte and the electrolyte from the cells cycled at 55°C also shown in Figure 7.3.2. The values obtained by GC/MS, ICP-OES and by FTIR/MLare indicated.

electrolyte	method	$LiPF_6$ / wt. %	EC / wt. %	DMC / wt. %
Fresh	As prepared	14.5	25.6	59.8
	GC-MS/ICP-OES	13.1 ± 0.1	26.5 ± 0.2	60.4 ± 0.3
	FTIR-ML	13.3 ± 0.4	27.5 ± 1.5	59.3 ± 1.2
4.1 V	GC-MS/ICP-OES	9.8 ± 0.2	29.51 ± 0.03	60.7 ± 0.2
	FTIR-ML	10.08 ± 0.02	25.35 ± 0.04	64.57 ± 0.03
4.3 V	GC-MS/ICP-OES	12.5 ± 0.2	29.8 ± 0.1	57.8 ± 0.1
	FTIR-ML	11.4 ± 0.4	25.4 ± 1.1	63.2 ± 0.9
4.5 V	GC-MS/ICP-OES	11.8 ± 0.1	30.22 ± 0.03	58 ± 0.3
	FTIR-ML	10.5 ± 0.6	26.3 ± 0.6	63.3 ± 0.5

7.4 Conclusions

A new method for the characterization of liquid electrolyte solutions, using FTIR and a machine learning algorithm, was presented. A satisfactory proof of concept for this method was shown from the characterization of known "unknown" solutions, and from the relatively good agreement between FTIR and GC-MS/ICP-OES on electrolytes taken from cycled Li-ion cells. It was found that the concentration of $LiPF_6$ was depleted by 10-20% in cells which had undergone 200 cycles at 55°C. This amount of salt loss is large and is likely a significant contributor to eventual cell failure. The speed, ease and cost advantages of the FTIR method will allow for analyses of the depletion of salt in aged lithium-ion cells and dramatic changes in solvent ratio. What is most important is that it is now possible to easily and quickly analyse the electrolytes from all cells in this laboratory at end of life or at specified points during life. Given that about 1300 Li-ion cells are tested each month in the Dahn lab, it is likely that this tool will yield many

interesting and important results and will allow deeper insight into the failure mechanisms of lithium-ion cells.

CHAPTER 8 CONCLUSION

8.1 SUMMARY

The work in this thesis aimed to improve the understanding of the parasitic reactions in lithium-ion cells. Parasitic reactions consume solvent, salt and active lithium in cells, and do not contribute to the desired charge/discharge reactions. They cause capacity loss and cell failure over time. Parasitic reactions are hard to observe since they sometimes involve complicated reactions between the positive and negative electrodes, carried out by unknown electrolyte decomposition products. The first part of this thesis aimed to uncover some of these hidden parasitic reactions.

In Chapter 3, the "pouch bag" method was used to uncover "chemical dialogue"-type parasitic reactions that occur in lithium-ion cells. It was found that CO_2 is continuously evolved from charged positive electrodes, from the oxidation of electrolyte. This is not evident from observing charged full cells since CO_2 is readily consumed by the negative electrode. XPS analysis was used to determine the effects of cross-talk on the surface chemistry of the electrodes, and to find the reaction products of CO_2 at the negative electrode.

Chapter 4 investigated the consumption of gases (other than CO_2) that are formed from the decomposition of electrolyte in the first cycle, namely H_2, C_2H_4 and CO. It was found that H_2 is consumed at both electrodes, although more so at the negative than at the positive electrode. C_2H_4 was consumed at the negative electrode, and more so at 60°C

than at 40°C. Storage of the positive electrode in C_2H_4 caused charge-transfer impedance growth, although the volumes of pouch bags containing positive electrodes and C_2H_4 did not shrink. CO was consumed at small amounts at the negative electrode.

Chapter 5 investigated whether the consumption of formation gas had an effect on the performance of the cell. There was no significant difference in self-discharge, charge-transfer resistance, or capacity between cells that were degassed and those that consumed their formation gas. However, there is evidence that suggests that an accumulation of Li_2CO_3, from the reduction of CO_2 evolved from the positive electrode, can contribute to cell failure. Future work, discussed in the next chapter, is required to investigate this hypothesis further.

Chapter 6 investigated the effect of formation cycle duration and temperature on the CE of new lithium-ion cells. The purpose of this work was to accelerate the maturity of SEIs during the first cycle, to allow for stabilized CE measurements to be taken after less time. It was found that formation at 60°C resulted in cells that had better initial CE than those formed at 40°C. Increasing the duration of the exposure to 60°C further improved the CE. XPS analysis suggested that organic SEI species in the negative electrode were replaced by inorganic SEI species as the cell matured. These results give insight into the mechanisms of cell maturity. Application of the formation protocol described in this work may decrease the time needed for HPC experiments in the Dahn lab.

In Chapter 7 a new method was introduced for determining the ratios of major components ($LiPF_6$, EC and linear carbonates) in typical lithium-ion battery electrolytes. Machine learning techniques were used to match features of the FTIR spectrum of an unknown electrolyte to a database of FTIR spectra with known compositions. With this method, $LiPF_6$ concentrations could be determined with similar accuracy and precision as an inductively coupled plasma optical emission spectrometry (ICP-OES) method. The ratios of organic carbonate solvent species were determined with more rapidity than gas chromatography (GC). This FTIR method is faster and less expensive than GC and ICP-OES and has the added benefit of being able to determine $LiPF_6$ concentration and solvent fractions simultaneously. Application of this tool can facilitate electrolyte analysis of aged lithium-ion cells and help elucidate mechanisms for cell degradation. In addition, this method could be applied to analyse any mixed solution across a wide range of application areas including beverages, redox flow and aqueous-ion batteries.

8.2 Future Work

The following section describes experiments that are motivated by the work in this thesis. These experiments would use the tools and techniques developed in this thesis. They would further improve the understanding of parasitic reactions that occur in lithium-ion cells.

8.2.1 Fully Characterize Products of Electrolyte Oxidation and Find Causes of Positive Electrode Impedance Growth

Deijun's "pouch bag" experiments, described in Section 3.1, showed that storage of individual charged positive electrodes in electrolyte at elevated temperatures caused CO_2-evolution and dramatic charge-transfer impedance growth.[42,44,46,47] Computational studies give Equation (14), reproduced below, as the most probable pathway for electrolyte oxidation and CO_2 evolution at the positive electrode.[81,82]

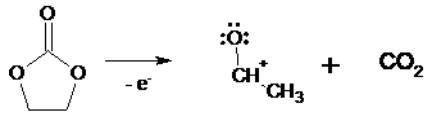

(14)

The carbocation produced by this reaction likely undergoes further reaction in the cell. It may react with other electrolyte species in solution, or it may diffuse towards the negative electrode and reduce, like CO_2, to form part of the negative electrode SEI. It is worthwhile to characterize and investigate the fate of this product, since the cause for dramatic positive electrode impedance growth in Deijun's pouch bags has not yet been discovered. It is possible that the non-gaseous by-products formed by electrolyte oxidation react with the positive electrode to cause dramatic impedance growth, if they are not removed in a cross-talk reaction with the negative electrode. Cells cycled to high voltages are often found to fail from large positive electrode impedance,[20–23] therefore investigating the mechanism for positive electrode impedance growth is very important.

8.2.2 Further Investigate the Correlation Between Cross-Talk and Capacity Fade Using XPS

This thesis focused mostly on the parasitic reactions in relatively young cells. Chapters 4-6 were heavily focused on the formation cycle, and the ~500 hours that followed. The XPS analysis in this thesis was done on relatively young cells. However, the effects of parasitic reactions are probably more obvious in aged cells that are on the verge of failure.

Experiments involving aged cells require careful panning, since cycling an academically relevant cell chemistry to failure requires several months, at least. Perhaps a great deal could be learned about failure mechanisms by doing systematic XPS studies on aged cells. For example, this thesis suggests that it is important to see what effect CO_2 cross-talk has on the cycle life of aged cells, especially those cycled to high voltage, where cells produce a lot of CO_2 and have increased rates of capacity fade. Section 5.4 discussed evidence in the literature that suggests that accumulation of Li_2CO_3 on the surface of aged negative electrodes may contribute to cell failure.[90,91]

The hypothesis that Li_2CO_3, from CO_2 cross-talk, accumulates on aged negative electrodes could be confirmed by doing XPS analysis on the negative electrodes aged to increasing degrees. For example, 10 identical cells could be made and cycled in the same way. At regular intervals, perhaps every 100 cycles, one cell could be removed from the charger and dissected for XPS analysis, to see whether the presence of Li_2CO_3 in the negative electrode SEI is correlated with increased capacity fade.

The degree of cross-talk can also be revealed by comparing the XPS spectrum of the front of an aged negative electrode (the side facing the positive electrode) to the back of the electrode (the side facing the copper foil), as shown in Figure 8.2.1. Preliminary results of this type of analysis consistently show that the SEI on the back of an aged negative electrodes is thinner than the front (because the SEI on the front is more likely to include additional species that migrate from the positive electrode), and that the thickness of the SEI on the front of the negative electrode increases as a cell approaches failure (suggesting that negative electrode pore-plugging contributes to cell failure). This work has the potential to prove the hypothesis that the accumulation of SEI species from cross-talk correlates with cell failure. If it is found that CO_2 cross-talk contributes to failure of high voltage cells, then efforts should be put into developing electrolyte solvents that do not oxidize to produce CO_2, or ones that do not dissolve CO_2. Such a solvent may improve the lifetime and energy density of lithium-ion cells.

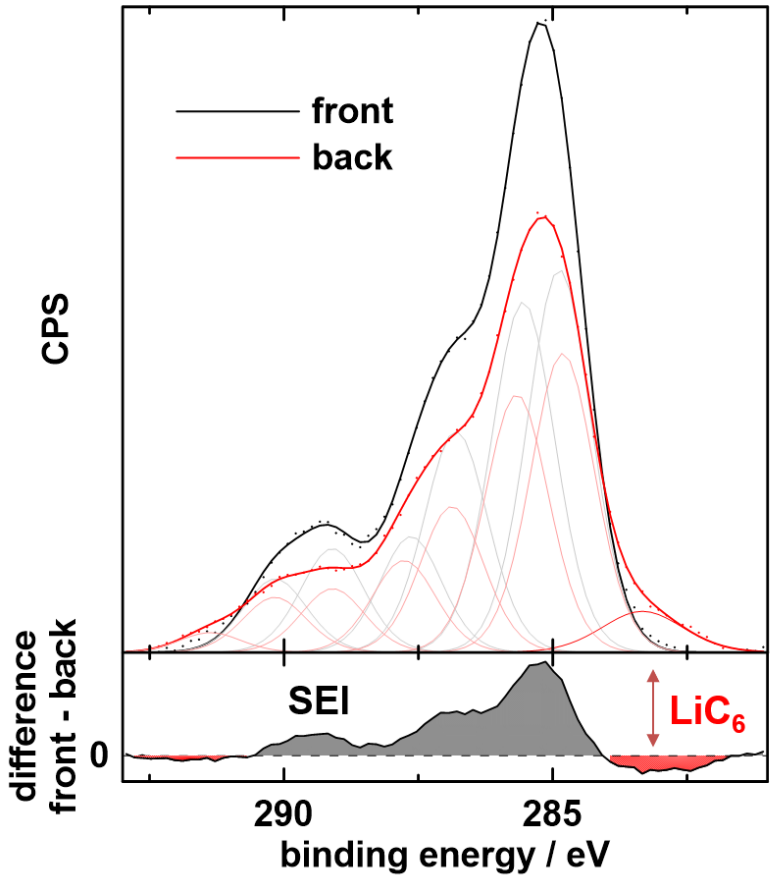

Figure 8.2.1: C1s spectra of the front (positive electrode-facing) and back (copper foil-facing) of an aged graphite negative electrode.

8.2.3 Use the FTIR Method to Investigate Changes in Electrolyte Composition in Aged Lithium-Ion Cells

Chapter 7 demonstrated proof of concept for a new method, using FTIR and machine learning, to easily find the ratios of $LiPF_6$, EC and linear carbonates in electrolyte. This method will be useful for determining the concentration of $LiPF_6$ in lithium-ion cells, since ICP-OES and other methods for determining the concentration of $LiPF_6$ in

electrolyte are time-consuming, expensive or complicated. Determining the fate of $LiPF_6$ in lithium-ion cells could be very interesting, since a preliminary study (using differential thermal analysis) demonstrated that a significant amount of $LiPF_6$ was consumed when cells were cycled aggressively (to 4.5 V at 40°C).[142] To probe this phenomenon, several experiments are currently underway that will use the FTIR method to determine the effect of temperature and upper voltage limit on the composition of electrolyte in cycled and stored lithium-ion cells.

REFERENCES

1. M. M. Thackeray, C. Wolverton, and E. D. Isaacs, *Energy Environ. Sci.*, **5**, 7854 (2012).

2. K. Xu, *Chem. Rev.*, **114**, 11503–11618 (2014).

3. A. J. Smith, J. C. Burns, D. Xiong, and J. R. Dahn, *J. Electrochem. Soc.*, **158**, A1136–A1142 (2011).

4. E. Peled and S. Menkin, *J. Electrochem. Soc.*, **164**, A1703–A1719 (2017).

5. R. Fong, U. von Sacken, and J. R. Dahn, *J. Electrochem. Soc.*, **137**, 2009–2013 (1990).

6. M. N. Obrovac and V. L. Chevrier, *Chem. Rev.*, **114**, 11444–11502 (2014).

7. P. Patel and P. Patel, *Sci. Am.* https://www.scientificamerican.com/article/could-cobalt-choke-our-electric-vehicle-future/.

8. Z. Lu, D. D. MacNeil, and J. R. Dahn, *Electrochem. Solid-State Lett.*, **4**, A200–A203 (2001).

9. T. Ohzuku and Y. Makimura, *Chem. Lett.*, **30**, 744–745 (2001).

10. H.-J. Noh, S. Youn, C. S. Yoon, and Y.-K. Sun, *J. Power Sources*, **233**, 121–130 (2013).

11. Y. Wang, X. Guo, S. Greenbaum, J. Liu, and K. Amine, *Electrochem. Solid-State Lett.*, **4**, A68–A70 (2001).

12. A. M. Andersson, D. P. Abraham, R. Haasch, S. MacLaren, J. Liu, and K. Amine, *J. Electrochem. Soc.*, **149**, A1358–A1369 (2002).

13. M. Balasubramanian, H. S. Lee, X. Sun, X. Q. Yang, A. R. Moodenbaugh, J. McBreen, D. A. Fischer, and Z. Fu, *Electrochem. Solid-State Lett.*, **5**, A22–A25 (2002).

14. L. E. Ouatani, R. Dedryvère, C. Siret, P. Biensan, S. Reynaud, P. Iratçabal, and D. Gonbeau, *J. Electrochem. Soc.*, **156**, A103–A113 (2009).

15. L. Madec, J. Xia, R. Petibon, K. J. Nelson, J.-P. Sun, I. G. Hill, and J. R. Dahn, *J. Phys. Chem. C*, **118**, 29608–29622 (2014).

16. J. Vetter, P. Novák, M. R. Wagner, C. Veit, K.-C. Möller, J. O. Besenhard, M. Winter, M. Wohlfahrt-Mehrens, C. Vogler, and A. Hammouche, *J. Power Sources*, **147**, 269–281 (2005).

17. M. Broussely, S. Herreyre, P. Biensan, P. Kasztejna, K. Nechev, and R. J. Staniewicz, *J. Power Sources*, **97–98**, 13–21 (2001).

18. J. Li, L. E. Downie, L. Ma, W. Qiu, and J. R. Dahn, *J. Electrochem. Soc.*, **162**, A1401–A1408 (2015).

19. R. Fathi, J. C. Burns, D. A. Stevens, H. Ye, C. Hu, G. Jain, E. Scott, C. Schmidt, and J. R. Dahn, *J. Electrochem. Soc.*, **161**, A1572–A1579 (2014).

20. R. Petibon, C. P. Aiken, N. N. Sinha, J. C. Burns, H. Ye, C. M. VanElzen, G. Jain, S. Trussler, and J. R. Dahn, *J. Electrochem. Soc.*, **160**, A117–A124 (2013).

21. L. Ma, J. Xia, and J. R. Dahn, *J. Electrochem. Soc.*, **161**, A2250–A2254 (2014).

22. C. . Chen, J. Liu, and K. Amine, *J. Power Sources*, **96**, 321–328 (2001).

23. K. Amine, C. H. Chen, J. Liu, M. Hammond, A. Jansen, D. Dees, I. Bloom, D. Vissers, and G. Henriksen, *Journal of Power Sources*, **97–98**, 684–687 (2001).

24. D. . Abraham, R. . Twesten, M. Balasubramanian, I. Petrov, J. McBreen, and K. Amine, *Electrochem. Commun.*, **4**, 620–625 (2002).

25. F. Lin, I. M. Markus, D. Nordlund, T.-C. Weng, M. D. Asta, H. L. Xin, and M. M. Doeff, *Nat. Commun.*, **5**, 3529 (2014).

26. K. J. Nelson, G. L. d'Eon, A. T. B. Wright, L. Ma, J. Xia, and J. R. Dahn, *J. Electrochem. Soc.*, **162**, A1046–A1054 (2015).

27. K. J. Nelson, D. W. Abarbanel, J. Xia, Z. Lu, and J. R. Dahn, *J. Electrochem. Soc.*, **163**, A272–A280 (2016).

28. L. O. Valøen and J. N. Reimers, *J. Electrochem. Soc.*, **152**, A882 (2005).

29. M. Nie, D. Chalasani, D. P. Abraham, Y. Chen, A. Bose, and B. L. Lucht, *J. Phys. Chem. C*, **117**, 1257–1267 (2013).

30. G. G. Botte, R. E. White, and Z. Zhang, *J. Power Sources*, **97-98**, 570–575 (2001).

31. S. E. Sloop, J. K. Pugh, S. Wang, J. B. Kerr, and K. Kinoshita, *Electrochem. Solid-State Lett.*, **4**, A42–A44 (2001).

32. K. Gavritchev, G. Sharpataya, A. Smagin, E. Malyi, and V. Matyukha, *J. Therm. Anal. Calorim.*, **73**, 71–83 (2003).

33. C. L. Campion, W. Li, and B. L. Lucht, *J. Electrochem. Soc.*, **152**, A2327–A2334 (2005).

34. H. Yang, G. V. Zhuang, and P. N. Ross, *J. Power Sources*, **161**, 573–579 (2006).

35. B. Ravdel, K. . Abraham, R. Gitzendanner, J. DiCarlo, B. Lucht, and C. Campion, *Journal of Power Sources*, **119–121**, 805–810 (2003).

36. L. D. Ellis, J. Xia, A. J. Louli, and J. R. Dahn, *J. Electrochem. Soc.*, **163**, A1686–A1692 (2016).

37. M. Moshkovich, M. Cojocaru, H. E. Gottlieb, and D. Aurbach, *J. Electroanal. Chem.*, **497**, 84–96 (2001).

38. J. Xu, R. D. Deshpande, J. Pan, Y.-T. Cheng, and V. S. Battaglia, *J. Electrochem. Soc.*, **162**, A2026–A2035 (2015).

39. D. P. Abraham, J. A. Gilbert, I. A. Shkrob, and K. Kalaga, *Meet. Abstr.*, **MA2017-02**, 151–151 (2017).

40. B. Michalak, B. B. Berkes, H. Sommer, T. Brezesinski, and J. Janek, *J. Phys. Chem. C*, **121**, 211–216 (2017).

41. Z. Chen, Y. Qin, and K. Amine, *Electrochimica Acta*, **54**, 5605–5613 (2009).

42. D. J. Xiong, L. D. Ellis, R. Petibon, T. Hynes, Q. Q. Liu, and J. R. Dahn, *J. Electrochem. Soc.*, **164**, A340–A347 (2017).

43. L. D. Ellis, J. P. Allen, L. M. Thompson, J. E. Harlow, W. J. Stone, I. G. Hill, and J. R. Dahn, *J. Electrochem. Soc.*, **164**, A3518–A3528 (2017).

44. D. J. Xiong, L. D. Ellis, K. J. Nelson, T. Hynes, R. Petibon, and J. R. Dahn, *J. Electrochem. Soc.*, **163**, A3069–A3077 (2016).

45. L. D. Ellis, S. Buteau, S. G. Hames, L. M. Thompson, D. S. Hall, and J. R. Dahn, *J. Electrochem. Soc.*, **165**, A256–A262 (2018).

46. D. J. Xiong, R. Petibon, M. Nie, L. Ma, J. Xia, and J. R. Dahn, *J. Electrochem. Soc.*, **163**, A546–A551 (2016).

47. D. J. Xiong, T. Hynes, L. D. Ellis, and J. R. Dahn, *J. Electrochem. Soc.*, **164**, A3174–A3181 (2017).

48. C. P. Aiken, J. Xia, D. Y. Wang, D. A. Stevens, S. Trussler, and J. R. Dahn, *J. Electrochem. Soc.*, **161**, A1548–A1554 (2014).

49. C. P. Aiken, J. Self, R. Petibon, X. Xia, J. M. Paulsen, and J. R. Dahn, *J. Electrochem. Soc.*, **162**, A760–A767 (2015).

50. J. Self, C. P. Aiken, R. Petibon, and J. R. Dahn, *J. Electrochem. Soc.*, **162**, A796–A802 (2015).

51. A. J. Smith, J. C. Burns, S. Trussler, and J. R. Dahn, *J. Electrochem. Soc.*, **157**, A196 (2010).

52. J. C. Burns, A. Kassam, N. N. Sinha, L. E. Downie, L. Solnickova, B. M. Way, and J. R. Dahn, *J. Electrochem. Soc.*, **160**, A1451–A1456 (2013).

53. J. Xia, L. Madec, L. Ma, L. D. Ellis, W. Qiu, K. J. Nelson, Z. Lu, and J. R. Dahn, *J. Power Sources*, **295**, 203–211 (2015).

54. J. Xia, L. Ma, C. P. Aiken, K. J. Nelson, L. P. Chen, and J. R. Dahn, *J. Electrochem. Soc.*, **161**, A1634–A1641 (2014).

55. J. Xia, M. Nie, J. C. Burns, A. Xiao, W. M. Lamanna, and J. R. Dahn, *J. Power Sources*, **307**, 340–350 (2016).

56. N. N. Sinha, A. J. Smith, J. C. Burns, G. Jain, K. W. Eberman, E. Scott, J. P. Gardner, and J. R. Dahn, *J. Electrochem. Soc.*, **158**, A1194 (2011).

57. J.-M. Atebamba, J. Moskon, S. Pejovnik, and M. Gaberscek, *J. Electrochem. Soc.*, **157**, A1218 (2010).

58. R. Petibon, L. Rotermund, K. J. Nelson, A. S. Gozdz, J. Xia, and J. R. Dahn, *J. Electrochem. Soc.*, **161**, A1167–A1172 (2014).

59. R. Petibon, V. L. Chevrier, C. P. Aiken, D. S. Hall, S. R. Hyatt, R. Shunmugasundaram, and J. R. Dahn, *J. Electrochem. Soc.*, **163**, A1146–A1156 (2016).

60. R. Dedryvère, L. Gireaud, S. Grugeon, S. Laruelle, J.-M. Tarascon, and D. Gonbeau, *J. Phys. Chem. B*, **109**, 15868–15875 (2005).

61. R. Dedryvère, S. Laruelle, S. Grugeon, L. Gireaud, J.-M. Tarascon, and D. Gonbeau, *J. Electrochem. Soc.*, **152**, A689–A696 (2005).

62. P. Verma, P. Maire, and P. Novák, *Electrochimica Acta*, **55**, 6332–6341 (2010).

63. S. Tanuma, C. J. Powell, and D. R. Penn, *Surf. Interface Anal.*, **17**, 927–939 (1991).

64. C. J. Powell and A. Jablonski, *NIST Electron Inelastic-Mean-Free-Path Database-Version 1.2*, National Institute of Standards and Technology, Gaithersburg, MD, USA, (2010).

65. I. A. Shkrob, A. J. Kropf, T. W. Marin, Y. Li, O. G. Poluektov, J. Niklas, and D. P. Abraham, *J. Phys. Chem. C*, **118**, 24335–24348 (2014).

66. C. Zhan, J. Lu, A. Jeremy Kropf, T. Wu, A. N. Jansen, Y.-K. Sun, X. Qiu, and K. Amine, *Nat. Commun.*, **4**, 2437 (2013).

67. A. Jarry, S. Gottis, Y.-S. Yu, J. Roque-Rosell, C. Kim, J. Cabana, J. Kerr, and R. Kostecki, *J. Am. Chem. Soc.*, **137**, 3533–3539 (2015).

68. D. Xiong, J. C. Burns, A. J. Smith, N. Sinha, and J. R. Dahn, *J. Electrochem. Soc.*, **158**, A1431–A1435 (2011).

69. R. Jung, M. Metzger, F. Maglia, C. Stinner, and H. A. Gasteiger, *J. Electrochem. Soc.*, **164**, A1361–A1377 (2017).

70. Y. R. Dougassa, C. Tessier, L. El Ouatani, M. Anouti, and J. Jacquemin, *J. Chem. Thermodyn.*, **61**, 32–44 (2013).

71. B. S. Parimalam, A. D. MacIntosh, R. Kadam, and B. L. Lucht, *J. Phys. Chem. C*, **121**, 22733–22738 (2017).

72. J. O. Besenhard, P. Castella, and M. W. Wagner, *Mater. Sci. Forum*, **91-93**, 647–652 (1992).

73. J. O. Besenhard, M. W. Wagner, M. Winter, A. D. Jannakoudakis, P. D. Jannakoudakis, and E. Theodoridou, *J. Power Sources*, **44**, 413–420 (1993).

74. S. E. Sloop, J. B. Kerr, and K. Kinoshita, *J. Power Sources*, **119–121**, 330–337 (2003).

75. L. J. Krause, V. L. Chevrier, L. D. Jensen, and T. Brandt, *J. Electrochem. Soc.*, **164**, A2527–A2533 (2017).

76. B. Strehle, S. Solchenbach, M. Metzger, K. U. Schwenke, and H. A. Gasteiger, *J. Electrochem. Soc.*, **164**, A2513–A2526 (2017).

77. B. Yang, H. Zhang, L. Yu, W. Fan, and D. Huang, *Electrochimica Acta*, **221**, 107–114 (2016).

78. G. Yang, J. Shi, C. Shen, S. Wang, L. Xia, H. Hu, H. Luo, Y. Xia, and Z. Liu, *RSC Adv.*, **7**, 26052–26059 (2017).

79. L. Ma, L. D. Ellis, S. L. Glazier, X. MA, Q. Liu, J. Li, and J. R. Dahn, *J. Electrochem. Soc.* (2018).

80. M. Onuki, S. Kinoshita, Y. Sakata, M. Yanagidate, Y. Otake, M. Ue, and M. Deguchi, *J. Electrochem. Soc.*, **155**, A794–A797 (2008).

81. L. Xing, W. Li, C. Wang, F. Gu, M. Xu, C. Tan, and J. Yi, *J. Phys. Chem. B*, **113**, 16596–16602 (2009).

82. L. Xing and O. Borodin, *Phys. Chem. Chem. Phys.*, **14**, 12838–12843 (2012).

83. M. Metzger, B. Strehle, S. Solchenbach, and H. A. Gasteiger, *J. Electrochem. Soc.*, **163**, A798–A809 (2016).

84. L. Manceron and L. Andrews, *J. Phys. Chem.*, **90**, 4514–4528 (1986).

85. E. Peled, *J. Electrochem. Soc.*, **126**, 2047–2051 (1979).

86. D. P. Summers and K. W. Frese, *J. Electrochem. Soc.*, **135**, 264–265 (1988).

87. Y. Hori, R. Takahashi, Y. Yoshinami, and A. Murata, *J. Phys. Chem. B*, **101**, 7075–7081 (1997).

88. K. J. P. Schouten, Z. Qin, E. Pérez Gallent, and M. T. M. Koper, *J. Am. Chem. Soc.*, **134**, 9864–9867 (2012).

89. F. Calle-Vallejo and M. T. M. Koper, *Angew. Chem.*, **125**, 7423–7426 (2013).

90. L. Zhao, I. Watanabe, T. Doi, S. Okada, and J. Yamaki, *J. Power Sources*, **161**, 1275–1280 (2006).

91. P. Bernard, H. Martinez, C. Tessier, E. Garitte, S. Franger, and R. Dedryvere, *J. Electrochem. Soc.*, **162**, A7096–A7103 (2015).

92. L. Chen, K. Wang, X. Xie, and J. Xie, *J. Power Sources*, **174**, 538–543 (2007).

93. M. A. McArthur, S. Trussler, and J. R. Dahn, *J. Electrochem. Soc.*, **159**, A198–A207 (2012).

94. A. M. Andersson and K. Edström, *J. Electrochem. Soc.*, **148**, A1100–A1109 (2001).

95. P. Lu, C. Li, E. W. Schneider, and S. J. Harris, *J. Phys. Chem. C*, **118**, 896–903 (2014).

96. A. J. Smith, J. C. Burns, and J. R. Dahn, *Electrochem. Solid-State Lett.*, **13**, A177 (2010).

97. A. J. Smith, J. C. Burns, X. Zhao, D. Xiong, and J. R. Dahn, *J. Electrochem. Soc.*, **158**, A447–A452 (2011).

98. D. Y. Wang, J. Xia, L. Ma, K. J. Nelson, J. E. Harlow, D. Xiong, L. E. Downie, R. Petibon, J. C. Burns, A. Xiao, W. M. Lamanna, and J. R. Dahn, *J. Electrochem. Soc.*, **161**, A1818–A1827 (2014).

99. M. Nie, L. Ma, J. Xia, A. Xiao, W. M. Lamanna, K. Smith, and J. R. Dahn, *J. Electrochem. Soc.*, **163**, A2124–A2130 (2016).

100. L. Ma, J. Self, M. Nie, S. Glazier, D. Y. Wang, Y.-S. Lin, and J. R. Dahn, *J. Power Sources*, **299**, 130–138 (2015).

101. D. Y. Wang, N. N. Sinha, R. Petibon, J. C. Burns, and J. R. Dahn, *J. Power Sources*, **251**, 311–318 (2014).

102. J. Li, A. R. Cameron, H. Li, S. Glazier, D. Xiong, M. Chatzidakis, J. Allen, G. A. Botton, and J. R. Dahn, *J. Electrochem. Soc.*, **164**, A1534–A1544 (2017).

103. B. Gyenes, D. A. Stevens, V. L. Chevrier, and J. R. Dahn, *J. Electrochem. Soc.*, **162**, A278–A283 (2015).

104. J. R. Dahn, J. C. Burns, and D. A. Stevens, *Electrochem. Soc. Interface*, **25**, 75–78 (2016).

105. http://www.novonix.ca/.

106. Bio-Logic Science Instruments https://www.bio-logic.net/en/divisions/bt-lab/.

107. S.-B. Lee and S.-I. Pyun, *Carbon*, **40**, 2333–2339 (2002).

108. S. S. Zhang, K. Xu, and T. R. Jow, *J. Power Sources*, **130**, 281–285 (2004).

109. M. Steinhauer, S. Risse, N. Wagner, and K. A. Friedrich, *Electrochimica Acta*, **228**, 652–658 (2017).

110. S. Bhattacharya, A. R. Riahi, and A. T. Alpas, *Carbon*, **67**, 592–606 (2014).

111. C. Huang, K. Huang, H. Wang, S. Liu, and Y. Zeng, *J. Solid State Electrochem.*, **15**, 1987–1995 (2011).

112. A. Friesen, X. Mönnighoff, M. Börner, J. Haetge, F. M. Schappacher, and M. Winter, *J. Power Sources*, **342**, 88–97 (2017).

113. S. L. Glazier, K. J. Nelson, J. P. Allen, J. Li, and J. R. Dahn, *J. Electrochem. Soc.*, **164**, A1203–A1212 (2017).

114. K. R. Lawless, *Rep. Prog. Phys.*, **37**, 231 (1974).

115. L. Ma, S. L. Glazier, R. Petibon, J. Xia, J. M. Peters, Q. Liu, J. Allen, R. N. C. Doig, and J. R. Dahn, *J. Electrochem. Soc.*, **164**, A5008–A5018 (2017).

116. S. Leroy, F. Blanchard, R. Dedryvere, H. Martinez, B. Carre, D. Lemordant, and D. Gonbeau, *Surf. Interface Anal.*, **37**, 773–781 (2005).

117. N. Leifer, M. C. Smart, G. K. S. Prakash, L. Gonzalez, L. Sanchez, K. A. Smith, P. Bhalla, C. P. Grey, and S. G. Greenbaum, *J. Electrochem. Soc.*, **158**, A471–A480 (2011).

118. S.-H. Lee, I.-S. Jo, and J. Kim, *Surf. Interface Anal.*, **46**, 570–576 (2014).

119. L. Madec and L. D. Ellis, *J. Electrochem. Soc.*, **164**, A3718–A3726 (2017).

120. G. Gachot, P. Ribière, D. Mathiron, S. Grugeon, M. Armand, J.-B. Leriche, S. Pilard, and S. Laruelle, *Anal. Chem.*, **83**, 478–485 (2011).

121. S. Wilken, M. Treskow, J. Scheers, P. Johansson, and P. Jacobsson, *RSC Adv.*, **3**, 16359 (2013).

122. P. Handel, G. Fauler, K. Kapper, M. Schmuck, C. Stangl, R. Fischer, F. Uhlig, and S. Koller, *J. Power Sources*, **267**, 255–259 (2014).

123. V. Kraft, M. Grützke, W. Weber, M. Winter, and S. Nowak, *J. Chromatogr. A*, **1354**, 92–100 (2014).

124. S. Nowak and M. Winter, *J. Electrochem. Soc.*, **162**, A2500–A2508 (2015).

125. C. Schultz, V. Kraft, M. Pyschik, S. Weber, F. Schappacher, M. Winter, and S. Nowak, *J. Electrochem. Soc.*, **162**, A629–A634 (2015).

126. W. Weber, V. Kraft, M. Grützke, R. Wagner, M. Winter, and S. Nowak, *J. Chromatogr. A*, **1394**, 128–136 (2015).

127. A. Guéguen, D. Streich, M. He, M. Mendez, F. F. Chesneau, P. Novák, and E. J. Berg, *J. Electrochem. Soc.*, **163**, A1095–A1100 (2016).

128. V. Kraft, W. Weber, B. Streipert, R. Wagner, C. Schultz, M. Winter, and S. Nowak, *RSC Adv.*, **6**, 8–17 (2016).

129. W. Weber, R. Wagner, B. Streipert, V. Kraft, M. Winter, and S. Nowak, *J. Power Sources*, **306**, 193–199 (2016).

130. S. Wiemers-Meyer, M. Winter, and S. Nowak, *Phys. Chem. Chem. Phys.*, **18**, 26595–26601 (2016).

131. X. Mönnighoff, A. Friesen, B. Konersmann, F. Horsthemke, M. Grützke, M. Winter, and S. Nowak, *J. Power Sources*, **352**, 56–63 (2017).

132. C. Schultz, S. Vedder, B. Streipert, M. Winter, and S. Nowak, *RSC Adv.*, **7**, 27853–27862 (2017).

133. J. Barthel and R. Deser, *J. Solut. Chem.*, **23**, 1133–1146 (1994).

134. J. Barthel, R. Buchner, and E. Wismeth, *J. Solut. Chem.*, **29**, 937–954 (2000).

135. N. Chapman, O. Borodin, T. Yoon, C. C. Nguyen, and B. L. Lucht, *J. Phys. Chem. C*, **121**, 2135–2148 (2017).

136. D. M. Seo, S. Reininger, M. Kutcher, K. Redmond, W. B. Euler, and B. L. Lucht, *J. Phys. Chem. C*, **119**, 14038–14046 (2015).

137. C. M. Burba and R. Frech, *J. Phys. Chem. B*, **109**, 15161–15164 (2005).

138. R. Aroca, M. Nazri, G. A. Nazri, A. J. Camargo, and M. Trsic, *J. Solut. Chem.*, **29**, 1047–1060 (2000).

139. S. Wilken, P. Johansson, and P. Jacobsson, *Solid State Ion.*, **225**, 608–610 (2012).

140. C. L. Angell, *Trans. Faraday Soc.*, **52**, 1178–1183 (1956).

141. B. M. Gatehouse, S. E. Livingstone, and R. S. Nyholm, *J. Chem. Soc.*, **0**, 3137–3142 (1958).

142. R. P. Day, J. Xia, R. Petibon, J. Rucska, H. Wang, A. T. B. Wright, and J. R. Dahn, *J. Electrochem. Soc.*, **162**, A2577–A2581 (2015).

APPENDIX A: COPYRIGHT STATEMENT

Chapters 3-7 in this thesis have content from the following published works that have been reproduced and/or adapted in accordance with the rights retained by authors for reuse of published materials. Figures and text from these works have been appropriately cited within the document.

1. D. J. Xiong, **L.D. Ellis**, K.J. Nelson, Toren Hynes, R. Petibon, and J. R. Dahn (2016) Rapid Impedance Growth and Gas Production at the Li-Ion Cell Positive Electrode in the Absence of a Negative Electrode, Journal of the Electrochemical Society, 163:A3069.
2. **L.D. Ellis**, J.P. Allen, J.E. Harlow, W.J. Stone, I.G. Hill and J.R. Dahn, (2017) Quantifying, Understanding and Evaluating the Effects of Gas Consumption in Lithium-Ion Cells. Journal of the Electrochemical Society, A164:A3518
3. **L.D. Ellis**, S. Buteau, Samuel G. Hames, Lauren E. Thompson, D.S. Hall, and J.R. Dahn, (2018) A New Method for Determining the Concentration of Electrolyte Components in Lithium-Ion Cells, using Fourier Transform Infrared Spectroscopy and Machine Learning, Journal of the Electrochemical Society, 165:A256

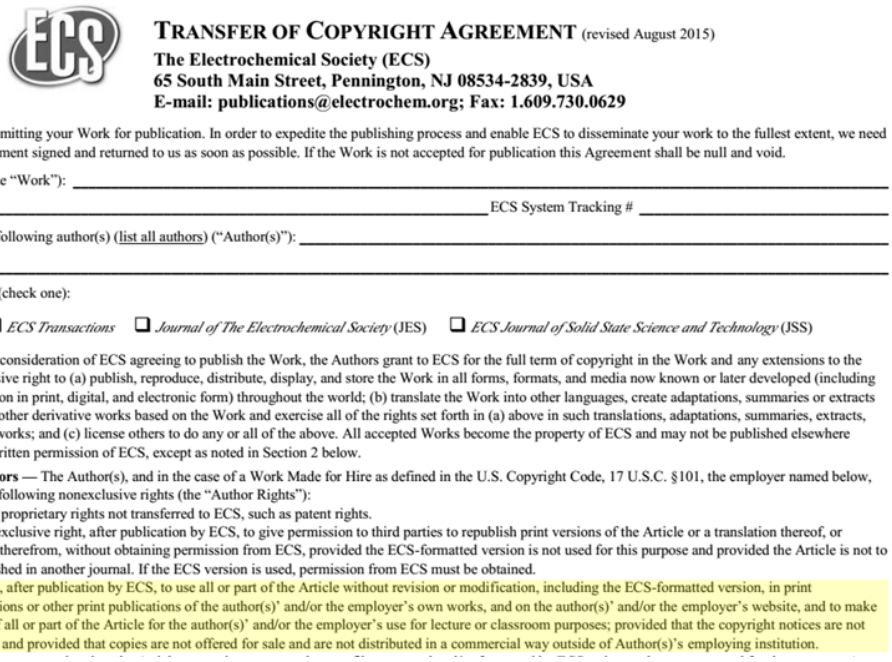

TRANSFER OF COPYRIGHT AGREEMENT (revised August 2015)

The Electrochemical Society (ECS)
65 South Main Street, Pennington, NJ 08534-2839, USA
E-mail: publications@electrochem.org; Fax: 1.609.730.0629

Thank you for submitting your Work for publication. In order to expedite the publishing process and enable ECS to disseminate your work to the fullest extent, we need to have this Agreement signed and returned to us as soon as possible. If the Work is not accepted for publication this Agreement shall be null and void.

Article entitled (the "Work"): _____

_____ ECS System Tracking # _____

Submitted by the following author(s) (list all authors) ("Author(s)"): _____

_____

for publication in (check one):

❑ *Interface* ❑ *ECS Transactions* ❑ *Journal of The Electrochemical Society* (JES) ❑ *ECS Journal of Solid State Science and Technology* (JSS)

1. **Transfer** — In consideration of ECS agreeing to publish the Work, the Authors grant to ECS for the full term of copyright in the Work and any extensions to the term, the exclusive right to (a) publish, reproduce, distribute, display, and store the Work in all forms, formats, and media now known or later developed (including without limitation in print, digital, and electronic form) throughout the world; (b) translate the Work into other languages, create adaptations, summaries or extracts of the Work or other derivative works based on the Work and exercise all of the rights set forth in (a) above in such translations, adaptations, summaries, extracts, and derivative works; and (c) license others to do any or all of the above. All accepted Works become the property of ECS and may not be published elsewhere without prior written permission of ECS, except as noted in Section 2 below.
2. **Rights of Authors** — The Author(s), and in the case of a Work Made for Hire as defined in the U.S. Copyright Code, 17 U.S.C. §101, the employer named below, shall retain the following nonexclusive rights (the "Author Rights"):
   a. All other proprietary rights not transferred to ECS, such as patent rights.
   b. The nonexclusive right, after publication by ECS, to give permission to third parties to republish print versions of the Article or a translation thereof, or excerpts therefrom, without obtaining permission from ECS, provided the ECS-formatted version is not used for this purpose and provided the Article is not to be published in another journal. If the ECS version is used, permission from ECS must be obtained.
   c. The right, after publication by ECS, to use all or part of the Article without revision or modification, including the ECS-formatted version, in print compilations or other print publications of the author(s)' and/or the employer's own works, and on the author(s)' and/or the employer's website, and to make copies of all or part of the Article for the author(s)' and/or the employer's use for lecture or classroom purposes; provided that the copyright notices are not removed and provided that copies are not offered for sale and are not distributed in a commercial way outside of Author(s)'s employing institution.

Figure 1.2.1, Figure 1.2.2 and Figure 1.2.3 were adapted with permission from the Journal of the Electrochemical Society and are cited appropriately in the figure captions.

Copyright Clearance Center

Confirmation Number: 11696684
Order Date: 02/01/2018

Customer Information

Customer: leah ellis
Account Number: 3001244602
Organization: leah ellis
Email: leahellis@dal.ca
Phone: +1 (902) 210-6472
Payment Method: Invoice

This is not an invoice

Order Details

Journal of the Electrochemical Society

Billing Status: **N/A**

Order detail ID:	70992291
ISSN:	0013-4651
Publication Type:	Journal
Volume:	
Issue:	
Start page:	
Publisher:	ELECTROCHEMICAL SOCIETY,
Author/Editor:	ELECTROCHEMICAL SOCIETY

Permission Status: Granted
Permission type: Republish or display content
Type of use: Republish in a thesis/dissertation
Order License Id: 4280360323499

Requestor type	Academic institution
Format	Electronic
Portion	chart/graph/table/figure
Number of charts/graphs/tables /figures	3
The requesting person/organization	Leah Ellis
Title or numeric reference of the portion(s)	Figures 1-3
Title of the article or chapter the portion is from	Interpreting High Precision Coulometry Results on Li-ion Cells
Editor of portion(s)	NA
Author of portion(s)	A. J. Smith, * J. C. Burns, * D. Xiong, and J. R. Dah
Volume of serial or monograph	158
Issue, if republishing an article from a serial	10
Page range of portion	A1136-A1142
Publication date of portion	2011
Rights for	Main product
Duration of use	Life of current edition
Creation of copies for the disabled	no

Note: This item was invoiced separately through our **RightsLink service.** More info **$ 0.00**

APPENDIX B: LIST OF CONTRIBUTIONS

1. S.L. Glazier, J, Li, X. Ma., J.P. Allen, **L.D. Ellis** and J.R. Dahn (2018) The Effect of Methyl Acetate, Ethylene Sulfate, and Carbonate Blends on the Parasitic Heat Flow of NMC532/graphite Lithium Ion Pouch Cells.

Contribution: performed calculations of solvent-salt binding energy using Gering's Advanced Electrolyte Model.

2. L.Ma, **L.D. Ellis**, S.L. Glazier, X. Ma, Q. Liu, J.Li and J. R. Dahn (2018) Lithium Difluorophosphate as an Electrolyte Additive in Li[Ni0.5Mn0.3Co0.2]O2/graphite Pouch Cells. *Submitted to the Journal of the Electrochemical Society.*

Contribution: performed XPS analysis on electrodes cycled in cells with lithium difluorophosphate. This work improved the understanding of how this additive imparted benefit.

3. **L.D. Ellis**, S. Buteau, Samuel G. Hames, Lauren E. Thompson, D.S. Hall, and J.R. Dahn (2018) A New Method for Determining the Concentration of Electrolyte Components in Lithium-Ion Cells, using Fourier Transform Infrared Spectroscopy and Machine Learning, #JESP-17-4472

Contribution: devised the method described in this paper and wrote the manuscript.

4. D. J. Xiong, M. Bauer, **L.D. Ellis**, T. Hynes, S. Hyatt, D.S. Hall and J. R. Dahn (2018) Some Physical Properties of Ethylene Carbonate-Free Electrolytes, Journal of the Electrochemical Society, 165:A126

Contribution: assisted in the discovery of the phenomenon discussed in the paper and assisted with data interpretation.

5. L. Madec, **L.D. Ellis,** (2017) Exploring Interactions between Electrodes in $Li[Ni_xMn_yCo_{1-x-y}]O_2$ graphite cells through Electrode/Electrolyte Interfaces Analysis, Journal of the Electrochemical Society, 164:A3718

Contribution: provided comments to the lead author that improved the logic and depth of the analysis.

6. E.C. Power, A.L. Paterson, U. Werner-Zwanziger, **L.D. Ellis,** J.W. Zwanziger (2018) Zero Stress-Optic Bismuth Oxide-Based Glass. Journal of Non-Crystalline Solids. 479:82

Contribution: analyzed the glasses discussed in this work using spectroscopic ellipsometry.

7. D.S. Hall, J.P. Allen, S.L. Glazier, **L.D. Ellis**, L. Ma, J.M. Peters, I.G. Hill, J.R. Dahn (2017) The Solid-Electrolyte Interphase Formation Reactions of Ethylene Sulfate and Its Synergistic Chemistry with Prop-1-ene-1, 3-Sultone in Lithium-Ion Cells, Journal of the Electrochemical Society, 164:A3445

Contribution: performed XPS analysis on electrodes cycled in cells ethylene sulfate. This analysis was used to confirm the decomposition mechanism of this additive.

8. C. Shen, D.J. Xiong, **L.D. Ellis**, Kevin L. Gering, L. Huang and J.R. Dahn, Using Positive Electrode Symmetric Cells to Find Electrolyte/Electrode Combinations with Minimum Reactivity. 164:13:A3349

Contribution: identified the cause of the corrosion problem discussed in this work and proposed its remedy; suggested the experiments involving $LiBF_4$-based electrolytes discussed in this work.

9. D. J. Xiong, T. Hynes and **L.D. Ellis** and J. R. Dahn, (2017) Effects of Surface Coating on Gas Evolution and Impedance Growth at $Li[Ni_xMn_yCo_{1-x-y}]O_2$ Positive Electrodes in Li-ion Cells, Journal of the Electrochemical Society, 164:A2174

Contribution: performed XPS analysis on electrodes cycled in pouch bags and pouch cells and developed the method for quantifying gas consumption at one electrode. This work improved the understanding of cross-talk reactions in cells.

10. **L.D. Ellis**, J.P. Allen, J.E. Harlow, W.J. Stone, I.G. Hill and J.R. Dahn, (2017) Quantifying, Understanding and Evaluating the Effects of Gas Consumption in Lithium-Ion Cells. Journal of the Electrochemical Society, A164:A3518

Contribution: conducted most of the experiments, analyzed the data and wrote the manuscript.

11. D. J. Xiong, **L.D. Ellis**, J. Li, H.Y. Li, T. Hynes, J.P. Allen, J. Xia, D. S. Hall, I.G. Hill and J. R. Dahn, (2017) Measuring Oxygen Release from Charged $LiNi_xMn_yCo_{1-x-y}O_2$ and its Effects on the Performance of High Voltage Li-ion Cells, Journal of the Electrochemical Society, 163:A3025

Contribution: performed XPS analysis on electrodes before and after O_2 release. This work contributed to the understanding of the phenomenon discussed in this work.

12. **L.D. Ellis**, I.G. Hill, Kevin L. Gering and J.R. Dahn (2017) Synergistic Effect of $LiPF_6$ and $LiBF_4$ as Electrolyte Salts in Lithium-Ion Cells, Journal of the Electrochemical Society, 164:A2426

Contribution: conducted most of the experiments, analyzed the data and wrote the manuscript.

13. D. J. Xiong, **L.D. Ellis** R. Petibon, Toren Hynes, Q.Q. Liu and J. R. Dahn (2017) Studies of Gas Generation, Gas Consumption and Impedance Growth in Li-ion Cells with Carbonate or Fluorinated Electrolytes Using the Pouch Bag Method, Journal of the Electrochemical Society, 164: A340.

Contribution: performed XPS analysis on electrodes cycled in pouch bags and pouch cells and developed the method for quantifying gas consumption at one electrode. This work improved the understanding of cross-talk reactions in cells.

14. **L.D. Ellis**, J. Xia, A.J. Louli and J.R. Dahn (2016) Effect of Substituting $LiBF_4$ for $LiPF_6$ in High Voltage Lithium-ion Cells Containing Electrolyte Additives, Journal of the Electrochemical Society, 163:A1686.

Contribution: conducted most of the experiments, analyzed the data and wrote the manuscript.

15. D. J. Xiong, **L.D. Ellis**, K.J. Nelson, Toren Hynes, R. Petibon, and J. R. Dahn (2016) Rapid Impedance Growth and Gas Production at the Li-Ion Cell Positive Electrode in the Absence of a Negative Electrode, Journal of the Electrochemical Society, 163:A3069.

Contribution: performed XPS analysis on electrodes cycled in pouch bags and pouch cells. This work improved the understanding of cross-talk reactions in cells.

16. D.S. Hall, M. Nie, **L.D. Ellis**, S. Glazier, S. Hyatt, R. Petibon, A. Xiao, B. Lamanna, K. Smith, I. Hill and J.R. Dahn (2016) Surface-Electrolyte Interphase Formation in Lithium-Ion Cells Containing Pyridine Adduct Additives. Journal of the Electrochemical Society. 163:A780.

Contribution: performed XPS analysis on electrodes cycled in cells pyridine adduct additives. This work improved the understanding of how these additives imparted benefit.

17. J. Xia, L. Madec, L. Ma, **L.D. Ellis**, W. Qiu, K.J. Nelson, Z, Lu and J.R. Dahn(2015) Study of Triallyl Phosphate as an Electrolyte Additive for High Voltage Lithium-Ion Cells. Journal of Power Sources. 295:203.

Contribution: performed XPS analysis on electrodes cycled in cells triallyl phosphate. This work improved the understanding of how this additive imparted benefit.